

**BACKGROUND REJECTION
IN
GAS DETECTORS**

by

Paul Ronald Ratcliff

**A thesis submitted to the University of Leiceester
for the degree of Doctor of Philosophy**

1988

UMI Number: U013865

All rights reserved

INFORMATION TO ALL USERS

The quality of this reproduction is dependent upon the quality of the copy submitted.

In the unlikely event that the author did not send a complete manuscript and there are missing pages, these will be noted. Also, if material had to be removed, a note will indicate the deletion.



UMI U013865

Published by ProQuest LLC 2015. Copyright in the Dissertation held by the Author.
Microform Edition © ProQuest LLC.

All rights reserved. This work is protected against
unauthorized copying under Title 17, United States Code.



ProQuest LLC
789 East Eisenhower Parkway
P.O. Box 1346
Ann Arbor, MI 48106-1346

X751537844

This work is dedicated to my parents, without whose support
I would have had to have got a "real job" ages ago !

Acknowledgments

I would like to take the opportunity to thank the people and institutions who have made this work possible, and pleasurable.

Financial support was provided by the Science and Engineering Research Council and AERE Harwell through a CASE award, and the facilities of the Physics Department of Leicester University were used with the permission of Professors E.A.Davies and K.A.Pounds.

Dr. Trevor Harris and his colleagues in the Electronics Workshop could always be relied upon for prompt and efficient technical assistance. Dr. Martin Turner provided numerous useful discussions and suggestions, and Mr. James Brier assisted in taking some of the experimental data and in the writing of two computer programs.

My supervisor at Harwell, Dr. John Leake, kept a close eye on the progress of the project and provided a necessary guiding hand on several occasions. Mr. David Lloyd provided important technical advice at Harwell. Dr. Don Newton provided numerous useful suggestions and information on the medical aspects of the subject, as well as allowing use of the facilities of the Body Radioactivity Measurement Section, and Ms Pauline Johnson was most helpful in organising the work of that section around my intrusions.

Finally it is a pleasure to acknowledge the expert over-all supervision of Dr. Ernest Mathieson who was never to be found short of ideas and who provided the theoretical basis of this work and most of the programs used in the computer simulations.

PUBLICATION

Some of the work reported here has been described in the following publication:

J.W.Leake, E.Mathieson, P.Ratcliff and M.J.L.Turner,
"Background Reduction by Pulse Shape Discrimination in a
Multiwire Plutonium Lung Monitor", Nucl. Instr. and Meth.
A269 No 1, 505-511 (1988)

CONTENTS

Page

Abstract

Acknowledgments

Publications

1	Contents	
6	Chapter 1	: Introduction
10	Chapter 2	: Proportional counters
10	2.1	: Counter operation
10	2.1.1	: Detector geometry
13	2.1.2	: Absorption of radiation
18	2.1.3	: Charge migration
19	2.1.4	: Townsend avalanche
22	2.1.5	: Gas mix

Page

23	2.1.6 : Positive ion motion
25	2.1.7 : Signal formation
27	2.2 : Background rejection
29	Chapter 3 : Pulse shape discrimination
29	3.1 : Detector pulses
33	3.2 : Experimental procedure
35	3.3 : Experimental results
35	3.3.1 : Pulse shape measurements
40	3.3.2 : Discrimination
42	Chapter 4 : Ion mobility measurements
42	4.1 : Theory
43	4.2 : Results
46	Chapter 5 : Radiation protection monitoring
46	5.1 : The radiation hazard

Page

50 5.2 : Plutonium metabolism

55 5.3 : Means of detection

61 5.4 : Detector criteria

63 5.5 : Detector technology

71 5.6 : Calibration

77 Chapter 6 : The prototype proportional chamber lung
 monitor

77 6.1 : Chamber design

81 6.2 : Background rejection

82 6.3 : Processing electronics

83 6.4 : Performance figures

88 Chapter 7 : Evaluation of the prototype lung
 monitor

88 7.1.1 : Proportionality

Page

88	7.1.2 : Gain
92	7.1.3 : Resolution
95	7.1.4 : Window transmission
96	7.2 : Background rejection
96	7.2.1 : Layer anticoincidence
99	7.2.2 : Guard anodes
100	7.2.3 : Guard cathodes
106	7.2.4 : Front guard
107	7.2.5 : Pulse shape discrimination
114	7.3 : Overall performance
117	7.4 : Comparison with other monitors
120	Chapter 8 : Charge width distribution
120	8.1 : Theory
124	8.2 : Apparatus
124	8.2.1 : The chamber
127	8.2.2 : The electrodes
127	8.3 : Preliminary results
131	8.4 : Results

Page

139 Chapter 9 : Discussion

145 Glossary

151 Abbreviations

154 Symbols

162 References

Chapter 1

Introduction

1.1 Historical perspective

The absorption of ionizing radiation by a gas produces free electric charge which may be used as the basis of the detection of that radiation. The movement of this charge in an electric field constitutes a current, though the magnitude of this current will generally be too small to be of practical use for the detection of individual photons or particles unless some form of physical amplification is employed.

In 1908 Rutherford and Geiger [1] reported the development of a counter in which the avalanche multiplication process described by Townsend [2], occurring in the high electric field near a fine wire, was used to obtain the required increase in charge. The real potential of this device was only fulfilled, however, in the 1930s, when pulse processing electronics became available.

By the end of the Second World War, Rossi and Staub [3] were able to describe a wide variety of proportional counters that had been developed under the impetus of the atomic weapons programme. One of these counters

incorporated a multiwire anode plane, though the full potential usefulness of this arrangement had apparently not been realised, and it was left to Charpak et al [4,5] to develop the idea and apply it to position-sensitive detection. The possibility of two-dimensional imaging using the charge induced on the cathode planes was also realised [6].

The great flexibility in choice of gas filling and detector geometry, coupled with good rate capability and real time imaging has opened up many fields of application for proportional counters, including x-ray diffraction [7-9], biophysics and medicine [10-13], x-ray astronomy [14,15], and materials studies, particularly in view of the vast improvement in data handling made possible by the rapid development of computer technology.

They also offer considerable possibilities for high sensitivity counting, in which a small signal, or a signal small compared to the inherent background level, must be measured. This is because of the possibility of discrimination between events on the grounds of energy deposited, event location within the detector, and the time and charge distribution profiles.

Gas detectors are only efficient for detecting radiation for which the gas has a significant stopping power. However, the effective range of detection can be extended to high energy γ -rays by incorporation of high

density converter materials, such as lead, in the detector design [16-18]. Alternatively, the radiation may be absorbed by a scintillator, such as barium fluoride (BaF_2), and the resulting ultraviolet radiation detected in a gas detector by absorption by a low photoionization potential molecule [19]. Thermal neutrons may also be detected [20,21].

Much recent work has been done on parallel plate structures, in which amplifying regions extend between conducting plates, instead of being confined to the vicinity of fine wires, and in multistep chambers, in which the overall gas gain is obtained in more than one amplification region [22].

Despite the advent and rapid development of scintillation and solid state detectors, the study and development of proportional counters remains of considerable importance due to the degree of flexibility in both design and usage. The combination of the inherent simplicity of the basic detector with the capacity to tailor performance for specific requirements should ensure a useful future for these detectors.

1.2 Scope of this thesis

This work is concerned almost exclusively with the application of the multiwire proportional counter to the

field of high sensitivity x-ray detection, with specific reference to the problems encountered in applications in radiological protection. Particular emphasis is placed on pulse shape discrimination, and position sensing is only dealt with where it pertains to background rejection.

Chapter 2 provides a basic description of the operation of a proportional counter. Chapter 3 covers the principles of pulse shape discrimination and the development of such a discrimination system. This system also allowed investigation of ion mobility in the high field region of a coaxial proportional counter, the results of which are presented in Chapter 4. Chapter 5 provides a review of the current status of radiation protection monitoring, with particular reference to plutonium-in-lung detection, and Chapters 6 and 7 describe the development and performance of a multilayer multiwire proportional chamber for this purpose. Chapter 8 introduces a further method of background rejection, namely charge shape discrimination, based on the lateral extent of the charge distribution induced on the cathode of a multiwire counter. A concluding chapter summarises the results obtained and their implications, and outlines some areas in which further development is possible.

Chapter 2

Proportional Counters

2.1 Counter operation

The following section provides a brief description of the operation of a proportional counter and of the physics of the processes involved. The present work concerns the detection of x-rays of < 25 keV, and only this particular case is considered in any degree of detail.

2.1.1 Detector geometry

In the most basic sense, a gas detector consists of a conducting envelope, or casing, enclosing a volume of gas, in which radiation will be absorbed, and the electrodes necessary for collection of the resulting free charge. The casing will contain feedthroughs to allow voltage supplies and amplifiers to be coupled to the electrodes, and may be sealed in order to preserve the purity of the counter gas or else contain a flow mechanism allowing the gas to be flushed.

Most non-imaging proportional counters are constructed with a cylindrical geometry (coaxial counters), as shown in

Fig. 2.1. The anode consists of a fine wire positioned along the axis of a hollow tube which serves as the cathode. This tube must obviously be made of, or contain a window of, a material transparent to the radiation to be detected.

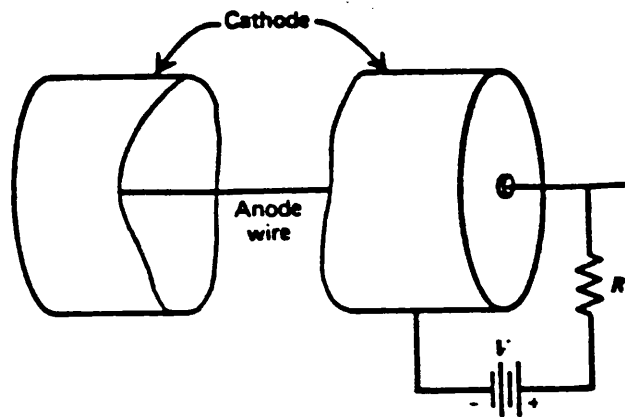


Fig. 2.1 Basic elements of a coaxial proportional counter. The output pulse is developed across resistor R.

For this geometry the electric field at radius r from the anode is given by

$$E(r) = \frac{V_a}{r \ln(r_c / r_a)} \quad \text{Eqn. 2.1}$$

where V_a is the potential difference between the anode and the cathode, r_a is the radius of the anode wire, and r_c is the internal radius of the cathode. The cathode is usually operated at earth potential.

Other designs of counter are possible, the most common being the multiwire proportional counter (MWPC) in which the

anode, and possibly the cathodes, consists of planes of wires (Fig. 2.2). This allows detectors with a large surface area to be constructed, and provides the possibility of two-dimensional position-sensitive detection, as well as providing a faster response.

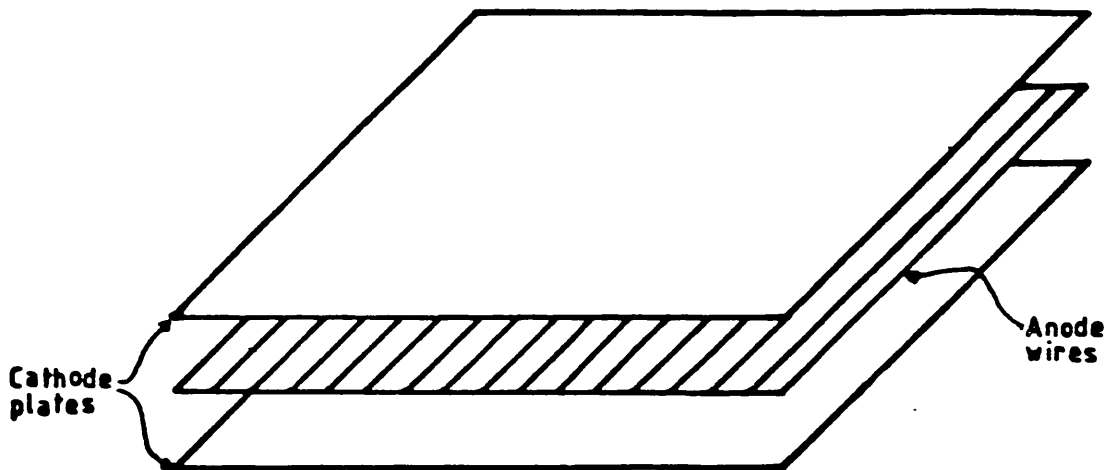


Fig. 2.2. Electrode configuration of a multiwire proportional counter. The cathodes may be an integral part of the chamber casing or else enclosed within the detector.

It has been shown [23] that for planar cathodes in an MWPC the electric field close to the anode wires (where gas multiplication occurs) has the same form as in the simple coaxial counter (Fig. 2.3). More complex geometries, such as with wire cathode arrays, can be treated by the superposition of the potentials due to individual wires.

Proportional counters have also been used in parallel plate, blade, needle and toroidal geometries.

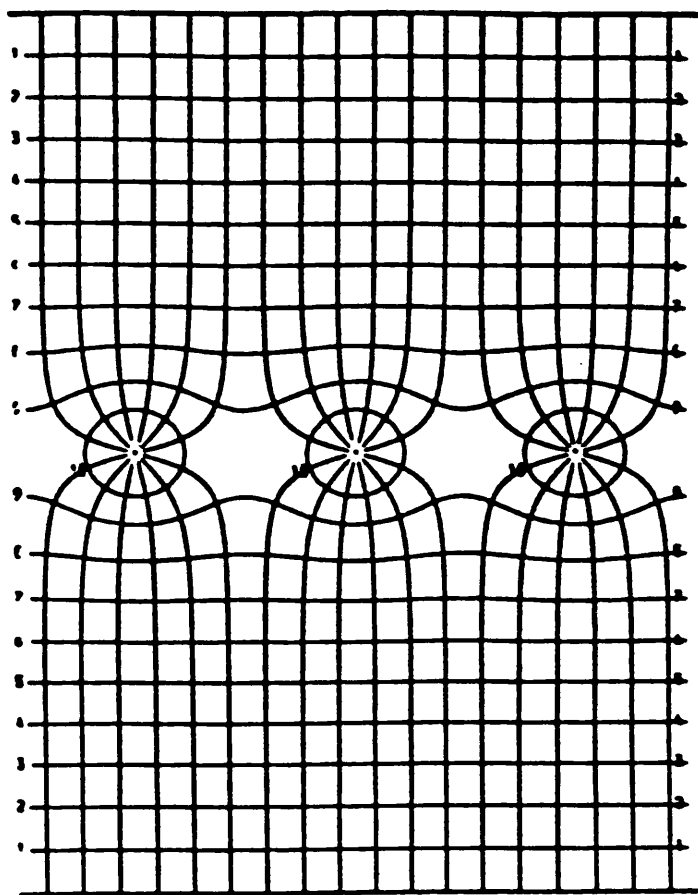


Fig. 2.3 Example of calculated field lines and equipotentials in an MWPC with continuous cathodes. The rapid transition from the almost radial field, comparable to that of a coaxial geometry, to the almost parallel field is notable [25].

2.1.2 Absorption of radiation

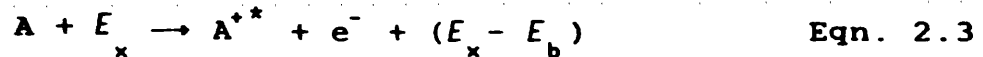
X-rays in the energy range of interest are absorbed in chamber gases almost exclusively by the photoelectric effect, the interaction cross-section for the competing process, Compton or incoherent scattering, generally being over 10^3 times smaller [24]. In the photoelectric process the entire energy of the absorbed photon is transferred to an electron in the absorbing atom, which is then ejected

with kinetic energy, E_e .

$$E_e = E_x - E_b \quad \text{Eqn. 2.2}$$

where E_x is the energy of the incident x-ray photon and E_b is the binding energy of the electron. In principle the photoelectron can come from any shell whose binding energy is less than that imparted by the photon, but the most probable origin is the shell with binding energy most closely approaching that of the x-ray. Under most circumstances this will be the K or L shell.

The absorbing atom is thus left in an ionized and excited state, generally with an inner shell vacancy:



The atom rapidly de-excites by a series of internal transitions, resulting in the emission of one or more characteristic fluorescent x-rays, or the excitation energy may be transferred directly to one of the outer electrons of the atom. This so-called Auger electron will be emitted with kinetic energy equal to the difference between the original excitation energy of the atom and the binding energy of the electron. Auger electrons thus produce a discrete energy spectrum corresponding to different initial and final states of the atom. The average probability of the former process is known as the fluorescent yield, and is related to the atomic number of the gas (see Fig. 2.4).

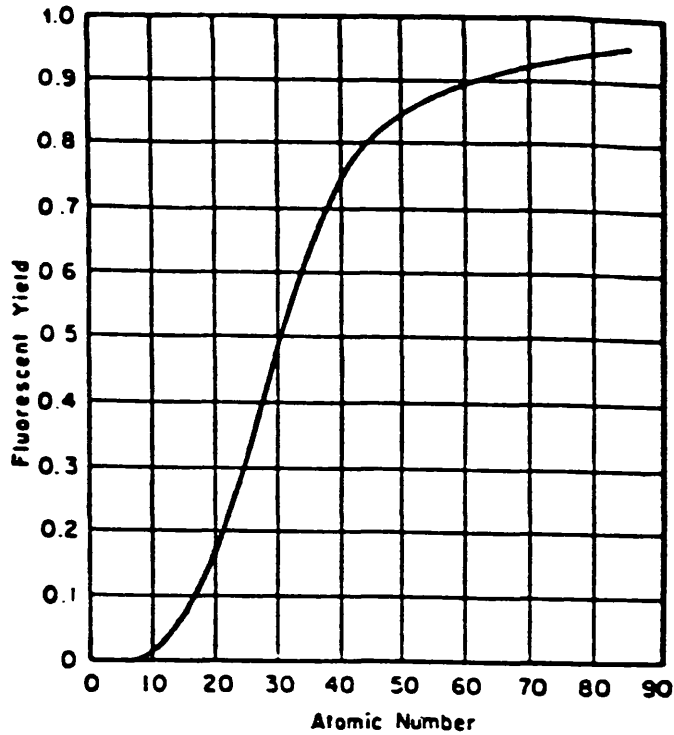


Fig. 2.4 Fluorescent yield in the K shell plotted as a function of atomic number [27].

Thus emission of fluorescent x-rays is more likely for xenon ($Z=54$) than it is for argon ($Z=18$). Gases generally have a relatively low absorption cross-section for their own characteristic radiation, so fluorescent x-rays can escape from the active volume of a detector. The energy deposited in the active volume will then be $(E_x - \Sigma E_f)$ where E_f is the energy of the escaping photon or photons.

The remaining available energy of the ion appears in further low energy Auger emission [26]. These secondary and tertiary Auger electrons have little kinetic energy, are confined to the location of the x-ray interaction and are subject to pronounced reabsorption by the atomic ions [28]. In contrast, the initial photoelectron and Auger electron

(if produced) can penetrate some distance through the gas, losing kinetic energy by successive collisions, and producing excitation or ionization of the target atoms. In most gases of interest for radiation detectors the ionization energy of the least tightly bound electron shells is 10-20 eV, but because of the possibility of energy deposition by excitation of a more tightly bound electron, the average energy lost by the incident electron per ion pair formed (the work function, W) is always greater than this, normally around 30 eV.

The total number of ion pairs produced, N , is thus given by

$$N = \frac{E_x - E_b}{W} \quad \text{Eqn. 2.4}$$

Empirical observations show that the work function is a remarkably constant parameter for many gases and different types of radiation, so for a given gas the number of ion pairs produced is a function of the photon energy only, E_b and W being essentially constant assuming absorption in a particular electron shell to be dominant. This provides the basis of useful proportional operation.

The relative variance on the number of ion pairs produced sets a fundamental limit on the energy resolution that can be achieved. If Poisson statistics were obeyed the standard deviation of the number formed would be equal

to the square root of the average number, but it is found [29] that

$$\left[\frac{\sigma_N}{\bar{N}} \right]^2 = \frac{\overline{(N-\bar{N})^2}}{\bar{N}^2} = \frac{F}{\bar{N}} \quad \text{Eqn. 2.5}$$

where \bar{N} is the mean number of ionizations for the particular x-ray energy. The Fano factor, F , is the factor by which the Poissonian variance has to be multiplied to give the observed variance, and would be equal to unity if Poisson statistics were obeyed. F is generally much smaller than this, for example $F=0.17$ for argon [30], because the processes that give rise to each individual charge carrier are not independent, and so the total number of charge carriers produced can not be described by simple Poisson statistics. The Fano factor is related to the fraction of all the incident photon energy that is used in forming ion pairs. If all the energy were always used, there would always be the same number of ion pairs produced, and the statistical fluctuation would be zero.

An increase in \bar{N} and a decrease in F can be achieved if a second gas is present which can be ionized by the excited atoms of the first, thereby reducing the variance. This is the principle behind the behaviour of Penning gas mixtures [28].

2.1.3 Charge migration

The result of an x-ray absorption is a relatively compact charge cloud, consisting of around 500 ion pairs (if $E_x \sim 15$ keV) in a volume $< 1\text{mm}^3$, at close to thermal energies. This cloud will spread by diffusion, and will drift due to the influence of any applied electric field, the free electrons drifting toward the anode and the positive ions toward the cathode.

Electron drift in gases under the influence of electric fields has been considered by a number of workers [31-35]. The mean drift velocity of the centre of the cloud, v_e , is given by

$$v_e = \mu_e E/p \quad \text{Eqn. 2.6}$$

where E/p is the reduced field (p being the gas pressure) and μ_e is the electron mobility, which is a function of the gas composition, temperature, pressure, and of the electric field (see Fig. 2.5). The electrons, being of low mass, undergo considerable acceleration between collisions and for typical chamber dimensions reach the anode in a few microseconds. Furthermore, there is usually a saturation effect of the drift velocity (of 10^4 - 10^5 m/s) above E/p values of about 10^4 - 10^5 V/m-atm.

The lateral extent the electron cloud attains is governed by diffusion. The standard deviation of the

distribution of the electrons in the cloud is given by

$$\sigma_{dif} = (2\epsilon_k d / eE)^{1/2} \quad \text{Eqn. 2.7}$$

where $\epsilon_k = eD/\mu_e$ is the characteristic energy of the electrons, e being the electron charge, D the electron diffusion coefficient, and d the distance moved by the cloud.

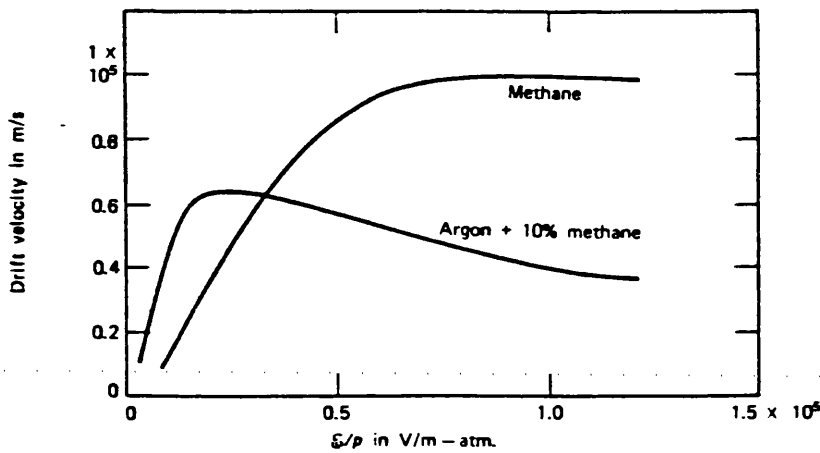


Fig. 2.5 Electron drift velocity plotted as a function of the reduced field [28].

2.1.4 Townsend avalanche

The behaviour of the electrons near the anode wire depends on the strength of the electric field. In a relatively weak field the electrons will be collected at the wire (as in an ionization chamber), but if the field exceeds a certain threshold (typically $\sim 10^6$ V/m for atmospheric pressure) they will gain sufficient energy between

collisions to cause ionization. An exponential avalanche then builds up, which is, in practice, confined to a radial extent of only a few wire radii. The process ends when all free electrons have been collected at the anode, and though the total number of secondary ionization events may be several orders of magnitude greater than the number of primary electrons, the total number will still be proportional to the number of primary electrons, and hence dependent on the energy of the initial ionizing photon. This physical charge amplification reduces the demands on external amplifiers and can result in significantly improved signal to noise characteristics compared to ionization chambers.

In normal operation the field is essentially unaffected by the avalanche process, though at very high counting rates or high chamber gains sufficient space charge of positive ions can be produced to cause significant local modification of the field [36-40]. Such field modifications may result in operating modes dramatically different from the normal proportional mode, as for example in the limited proportional region or in self-quenching streamer operation [41]. If the applied voltage is sufficiently high, the space charge created by the positive ions can become completely dominant. Under these conditions the avalanche continues until a sufficient number of positive ions have been created to reduce the field below the point at which gas multiplication can take place. The process is thus self-limiting and terminates when a certain number of ion

pairs have been formed, regardless of the number created by the incident radiation, thus losing energy proportionality. If the avalanche also propagates laterally along the anode wires due to ultraviolet ionisation of the gas, the Geiger-Muller region of operation occurs (Fig. 2.6).

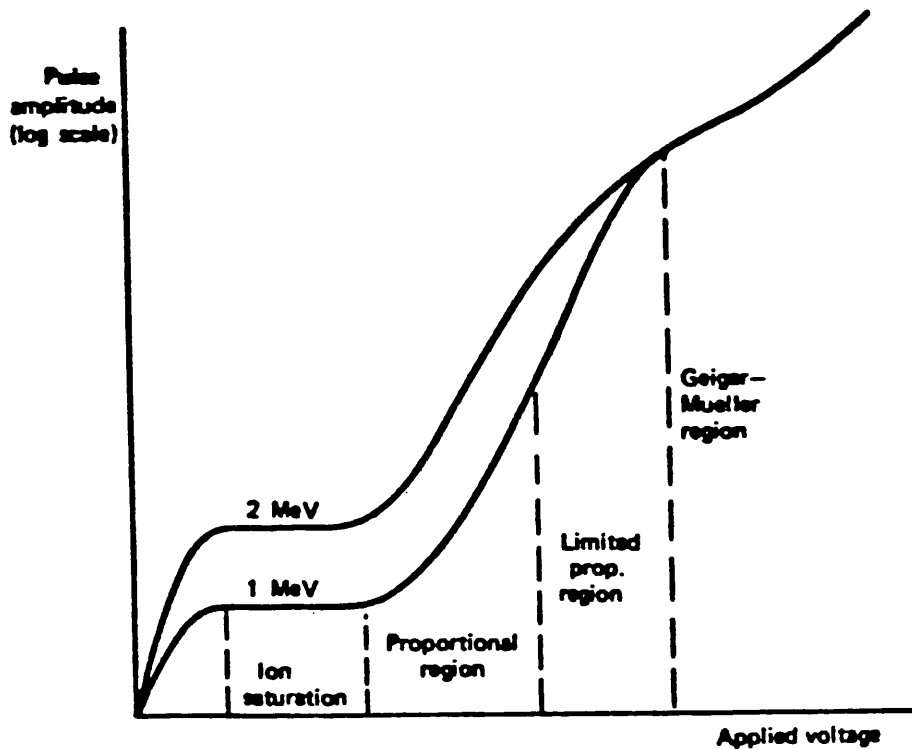


Fig. 2.6 Different regions of operation of gas-filled detectors. The curves represent events depositing two different amounts of energy within the counter gas.

The relative variance in the size of the avalanche produced by each individual primary electron is

$$\left[\frac{\sigma_A}{\bar{A}} \right]^2 = \frac{\overline{(A - \bar{A})^2}}{\bar{A}^2} = f \quad \text{Eqn. 2.8}$$

where \bar{A} is the mean gain. f is quite large, ~0.6 to 0.7 for argon [40], and is very sensitive to the details of the first few ionizations. However, the overall variance for \bar{N} independently developing avalanches is reduced to f/\bar{N} , and so, from Eqn. 2.5, the variance on the total number of electrons generated, P , is [42-44]

$$\left[\frac{\sigma_P}{\bar{P}} \right]^2 = \frac{(F+f)W}{E_x} \quad \text{Eqn. 2.9}$$

with $\bar{P} = \bar{N}\bar{A}$. This value represents the ideal energy resolution of the counter (about 15% for 5.9 keV x-rays in argon), but in practice mechanical imperfections (such as varying wire radius), marginal misplacement of wires in MWPCs and loss of electrons to species with significant electron affinity can worsen the resolution. Further degradation can be caused if the uv photons emitted by collisionally excited noble gas atoms eject electrons from the metal surfaces of the detector [45] which then produce secondary avalanches [46,47].

2.1.5 Gas mix

Gas multiplication is critically dependent on the migration of the free electrons, so it is essential that the gas in the counter has negligible concentrations of molecules with significant electron affinities. For this

reason the noble gases are ideal, argon being commonly used for detection of soft x-rays (<10 keV) and xenon at slightly higher energies (10-30keV). Air, of course, does have significant electron affinity, so it is essential to maintain the purity of the counter gas.

Normally a small amount (5-10%) of a polyatomic quench gas is added to de-excite the noble gas atoms by collision and to absorb the uv radiation they produce. These photons will cause instabilities in operation and loss of proportionality in a pure noble gas if the gas gain exceeds about 100, but the quench gas absorbs them in a manner that does not lead to further ionization. Methane is commonly used with argon, and allows stable operation at avalanche charges in excess of 1 pC. In many gas mixes the quench gas also undergoes charge transfer with the positive noble gas ions since they have lower ionization potentials, so it is the ions of the quench gas that drift to the cathode. This occurs for argon/methane mixes, but not for xenon/carbon dioxide which was the counter gas used for most of the work included in this thesis.

2.1.6 Positive ion motion

A similar equation to that governing electron drift applies to the positive ions, though their greater mass means that mobilities are typically a factor of around 10^3 lower than that of electrons, and they are not greatly

dependent on field and pressure over a wide range of values (see Fig. 2.7). Ion collection times are thus of the order of milliseconds, which imposes a rate limitation on the counter since stacking of signals will occur if events overlap in time. Diffusion is also much smaller for ions due to their greater mass.

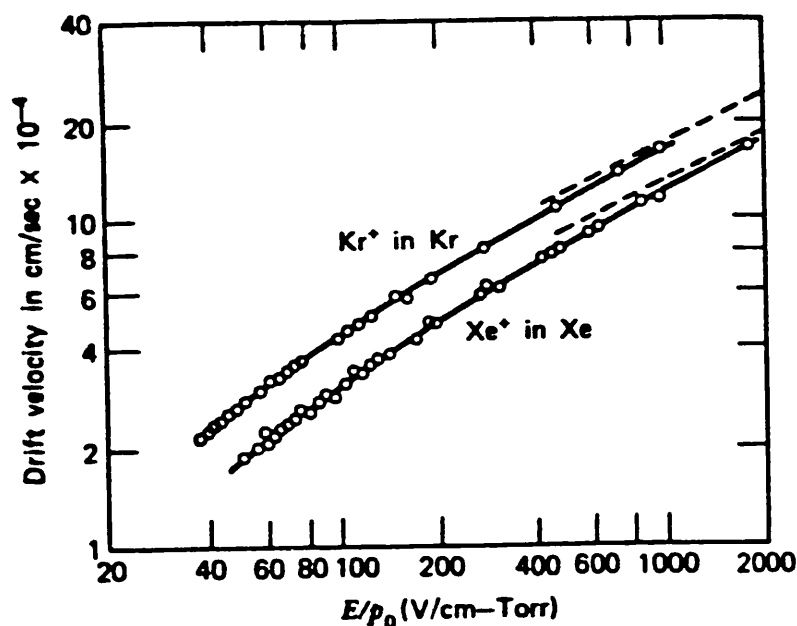


Fig. 2.7 Positive ion drift velocities plotted as a function of the reduced field [49].

At about $5 \mu m$ from the surface of the cathode the ions neutralise by extracting an electron from the metal surface [48]. The remaining energy, the difference between the ionization energy and the metal work function, is dissipated according to the ion species. Polyatomic quench gases are thought to dissociate, but if the charge carriers are noble gas atoms then inelastic collision with the electrode, uv emission or ejection of further electrons are possible. The latter two are clearly undesirable.

2.1.7 Signal formation

The time history of the detector pulses are divided into two distinct stages: the drift time taken by the primary electrons to travel from their original position to the multiplication region, and the multiplication time from the onset to the completion of the avalanche. The drift time is typically much greater than the multiplication time, though it is dependent on the position of the original ion pair, but the contribution to the output pulse during this time is negligible compared to the contribution by the much larger number of charge carriers in the avalanche [25,28]. The effect of the drift time is thus to introduce a delay between the time of formation of the original ion pair and the start of the corresponding output pulse.

Because of the exponential nature of the avalanche, most of the electrons and ions are created very close to the anode wire, and the electrons are collected very quickly. This does not constitute the detected signal since the close proximity of the ions results in an induced charge on the anode almost equal to that of the collected electrons. There is thus very little change in the potential of the anode, and the detected signal results from the reduction in induced charge on the anode (and the comensurate increase on the cathode) due to the motion of the positive ions as they drift outward along the field lines.

This motion is initially rapid due to the intense field near the anode wire, leading to a fast-rising initial component to the pulse. However, as the ions reach regions with a less intense field (greater radii in a coaxial geometry) their motion is slower, and the pulse rises correspondingly slowly. The total duration of the pulse can thus be relatively long and if the pulses are shaped using amplifiers with time constants not exceeding a few microseconds, the slow drift period no longer contributes to the pulse amplitude. The shaped pulse thus has an amplitude less than that which would be obtained with an infinite time constant by an amount known as the "ballistic deficit".

The expected pulse shape has been shown [43] to have the form

$$q(t) = q_0 C \ln(1+t/t_0) \quad \text{Eqn. 2.10}$$

where q_0 is the total avalanche charge, $C=1/\ln(r_c/r_a)^2$, r_c is the cathode radius and r_a is the anode wire radius (see Fig. 2.8).

The characteristic time t_0 is given by

$$t_0 = r_a^2 / 4\mu C V_a \quad \text{Eqn. 2.11}$$

where μ is the positive ion mobility and V_a is the operating voltage.

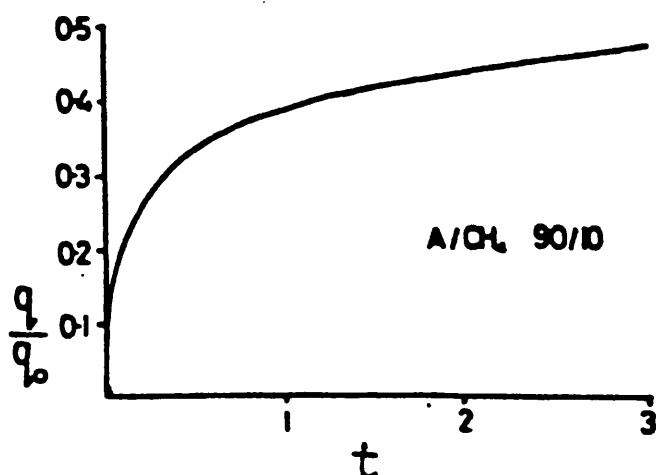


Fig. 2.8 Theoretical shape of the leading edge of the output pulse from a typical proportional counter.

2.2 Background rejection

The signal efficiency of a proportional counter is limited by the stopping power of the gas in the active volume, but the limit of detection can be improved if the background count rate is reduced, thus improving the signal to noise ratio. This is the main concern of the work in this thesis.

Background counts are produced in a proportional counter by relativistic charged particles, stopping charged particles, muons from cosmic rays which may either pass through the detector or decay to electrons within the chamber, and stray x-ray and γ -ray photons from the trace amounts of radioisotopes in the environment. The flux of the less penetrating of these can be reduced considerably if the counter is operated in a screened environment totally free of contaminants, though the screening material must

obviously be massive, and is thus not practicable for various applications, such as on satellites, where weight is at a premium.

Relativistic particles pass straight through a detector leaving a continuous charge track and can thus be detected by anticoincidence counters surrounding the detector, or by anticoincidence electrodes incorporated in the counter design. Most stopping particles deposit more energy in the active volume than the signal x-rays and may thus be rejected by discrimination based on the height of the shaped pulses. Charged particles, whether cosmic rays or Compton electrons produced by x-ray or γ -ray interactions with the counter material or gas, which deposit energy within the accepted range and are not eliminated by guard cells are more difficult to reject. Several systems have been developed to do this based on differences in the detector pulse shapes between x-ray and particle events [50-56], two of which are described in detail in Chapters 3 and 7.

CHAPTER 3

Pulse Shape Discrimination

3.1 Detector pulses

Equation 2.10 gives the theoretical pulse shape resulting from a single electron avalanche. However, a detector pulse is the sum of the signals from the N avalanches formed by the primary electrons, which will not be exactly coincident since the electrons will arrive at the multiplication radius over a finite time interval, τ , determined by the length and orientation of the initial ionization track and the effects of electron diffusion during the drift time. The risetime of the detector pulse is thus slowed by a factor dependent on this time interval. For low energy x-ray events, which form a highly localised charge cloud, τ results only from the extent of the cloud along the field lines due to the effects of photoelectron range and diffusion, and is thus small and has little effect on the pulse shape. An energetic particle passing through part of the detector will produce an ionization track over a larger spatial region, resulting in a greater variation in drift times, a larger value of τ , and a pulse that might have an appreciably slower rise (see Fig. 3.1).

One of the earliest, and simplest, methods of pulse shape discrimination in proportional counters [55,56] employs a doubly differentiating, singly integrating filter to produce a zero-crossing output waveform. The cross-over time, t_x , is dependent on the rise-time of the charge waveform, and measurement of this parameter therefore allows some limited discrimination to be made against events of spatially extended ionization. Most suggested methods involve converting the time interval between the leading edge of the shaped pulse and the zero-crossing point into an amplitude and defining a threshold above which events will be rejected. Culhane and Fabian [57] investigated three possible methods of detecting the leading edge of the shaped pulse, but a slightly different approach was adopted here.

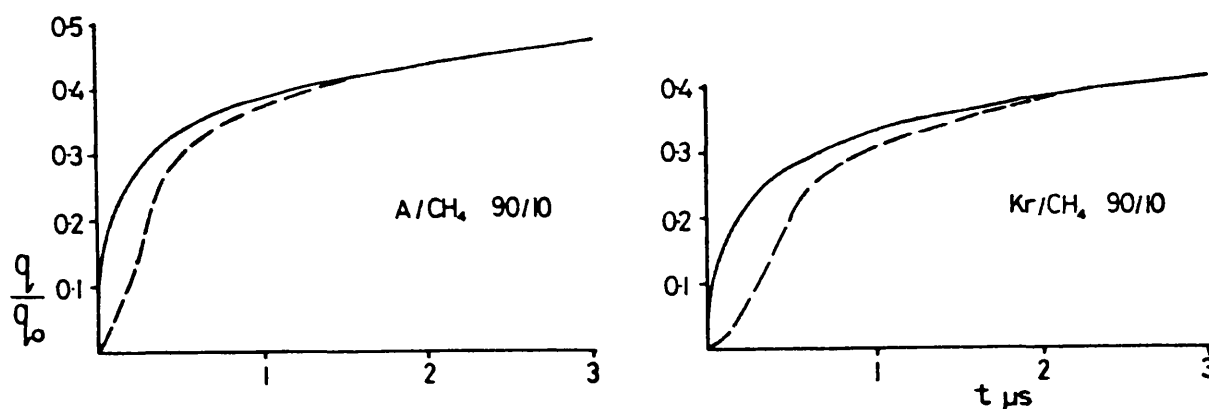


Fig. 3.1 Leading edge of the output pulse shape from a typical counter. The solid curve represents point ionisation, the broken curve distributed ionisation [28].

In order for discrimination based on this principle to be effective it is necessary to maximise the dependence of the cross-over time on τ , and to minimise the width of the measured cross-over spectrum.

The experimental cross-over time, t_c , will be given by $t_c = t_x - t_s$, where t_s is the experimental start time.. Both t_s and t_x will exhibit fluctuations due to electronic noise and t_s will also fluctuate with signal amplitude if the start signal is produced by some form of leading edge discriminator. Assuming that, after a common pre-amplifier stage, separate channels are employed to define the start and cross-over times, then the variance in t_c will be given by

$$\sigma_c^2 = \sigma_0^2 + \left[\frac{q_n}{q_0} \right]^2 (A_1^2 + A_2^2) + A_3^2 \quad \text{Eqn. 3.1}$$

where q_n is the rms equivalent noise charge, and is assumed to be the same for both channels. σ_0 represents an intrinsic time spread due to the extent of the charge cloud. A_1 is determined by the filter characteristics of the cross-over channel, while A_2 and A_3 are determined by those of the start channel. A_2 represents the fluctuations in t_s due to electronic noise, and A_3 those due to the spread in pulse heights, and is thus dependant on the range of q_0 values to be accepted by the electronic processing.

It has been shown [55,56] that A_1 may be minimised by choosing equal integrating and differentiating time constants, T_x , and by choosing T_x about $5t_0$. This minimum is very shallow, however, and several times this optimum value can be used without a serious deterioration in performance.

A_2 and A_3 can not be minimised, but their contribution to σ_e is inversely dependant on the risetime of the start channel pulse. The start channel integrating time constant, T_s , should thus be made as small as practicable.

The shape of the cross-over spectrum for background events can not be predicted theoretically due to the non-Gaussian pulse height spectrum and the variation in the extent of the initial ionization, but a simple model for an average extended ionization event can be considered [56]. If the primary electron charge is considered to arrive at the anode as a constant current of duration τ and experiences constant gas gain, the cross-over and start times may be readily calculated for the resultant chamber signal. These calculations show that the shift in the measured cross-over time from the case $\tau=0$ may be expressed as

$$\Delta t_e = \tau(b_1 - b_2(q_0)) \quad \text{Eqn. 3.2}$$

If T_x is approximately $5t_0$ then b_1 is very approximately 0.55. The value of b_2 depends on the signal amplitude and on the start channel integrating time constant, but if this is small compared with T_x then b_2 is small compared with b_1 . Typical values are ~ 0.15 [58].

This treatment is based on an idealised waveform describing an average extended event. In practice the different track orientations and extensions associated with

background events will produce a wide range of signal shapes, leading to a wide range of values of t_0 , but this model forms a useful baseline for comparing and describing system performance.

3.2 Experimental procedure

The pulse shape discrimination system was developed and assessed using a small coaxial proportional counter, containing a 2 atmosphere filling of Xe/20% CO₂. The anode wire radius was 25 μ m, and the cathode radius 11.7 mm, producing a gas gain of about 4.4×10^3 at an operating voltage of 2.45 kV.

The electronic system (see Fig. 3.2) consisted of a charge sensitive pre-amplifier, with nominal risetime 30 ns, feeding, in parallel, an energy selective channel, a fast start-pulse channel and a cross-over (RC-CR-CR filter) stop channel. A TAC was used to convert the time difference between the start and stop pulses into an amplitude, and the final pulse height analyser recorded the resultant cross-over spectrum. A delay could be introduced in either the start or stop channels in order to make the width of the measured spectrum compatible with the TAC range.

The nominal integrating and differentiating time constants of the fast channel were 10 ns and 5 μ s respectively, and the filter time constants of the

cross-over channel were 0.2 μ s. The actual output waveforms of the pre-amplifier and the fast and cross-over channels were determined by examining in detail, with a digital storage oscilloscope, the waveforms for a very fast step pulse input. This enabled a computer program, with adjustable time constants, to be developed to simulate the system and establish the correct time constants, and thus to predict the values of A_1 , A_2 and A_3 .

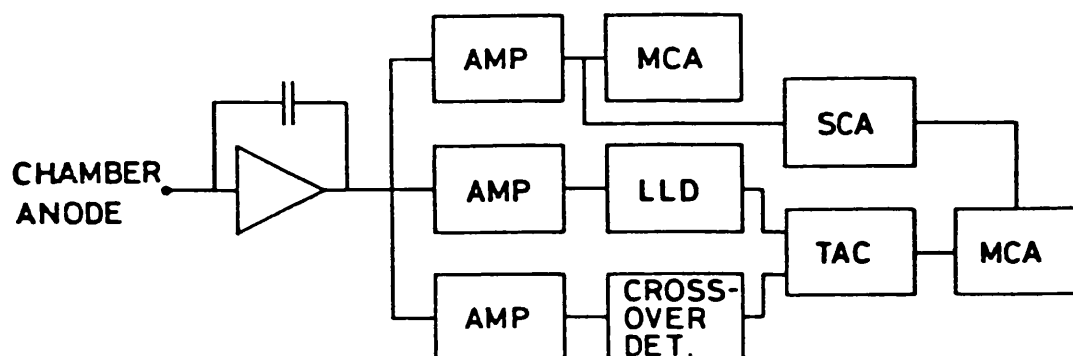


Fig. 3.2 Block diagram of the electronic system for pulse shape analysis. A single channel analyser is used after the TAC (in parallel with the MCA) to provide discrimination.

With the chamber detecting Cd^{109} x-rays (22 keV) the output waveform of the cross-over and start channels were again measured in detail. Because the zero time is poorly defined in this case, the shape of the leading edge of the waveform was explored by measuring the time interval between crossing an adjustable threshold and the zero-crossing point (of the cross-over channel) as a function of the threshold setting, which could be adjusted to a known fraction of the peak output pulse height. With the amplifier models

established by the step pulse input measurements, these data enabled approximate values of t_0 to be determined for the detector.

3.3 Experimental results

3.3.1 Pulse shape measurements

For a step input pulse, Eqn. 3.1 reduces to

$$\sigma_e = \frac{q_n}{q_0} (A_1^2 + A_2^2)^{1/2} \quad \text{Eqn. 3.3}$$

since σ_0 results from charge cloud characteristics and $A_3=0$. A_2 may also be eliminated by taking the TAC start signal directly from the pulser, leaving

$$\sigma_e = (q_n/q_0) A_1 \quad \text{Eqn. 3.4}$$

Knowledge of the value of q_n (measured as 950 e⁻s rms) thus allows A_1 to be determined experimentally from a plot of σ_e against $1/q_0$. (Fig. 3.3).

This in turn allows A_2 to be determined from data acquired using the electronic system to provide both the TAC start and the stop signals via Eqn. 3.3. Fig. 3.4 shows the close agreement between the experimental and theoretical

values, which suggests that it is valid to extend the procedure to consider x-ray pulses, for which the individual values of A_1 and A_2 , and of A_3 and σ_0 can not be separated experimentally.

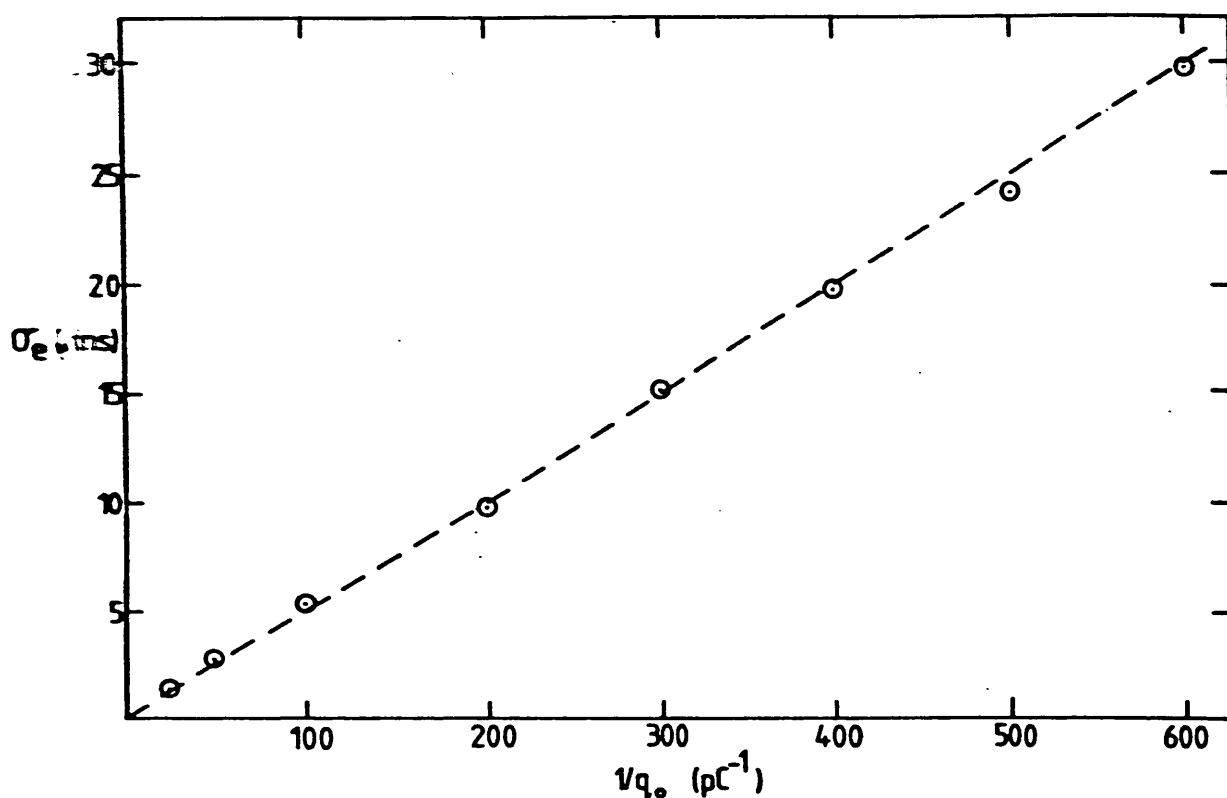


Fig. 3.3 Rms width of cross-over spectrum for a direct TAC start signal plotted as a function of $1/q$, where q is the step input charge. The broken line is the theoretical relationship derived from the measurement of rms equivalent noise charge, q_n , and determination of the system time constants.

Retaining the program parameters used to match the pulser waveforms, it is possible to deduce the chamber characteristic time, t_0 , required to provide a match to the output waveforms resulting from x-ray events. The value obtained, 48 ns, corresponding to an average ion mobility $\mu = 0.17$ cm²/Vs (0.34 cm²/Vs at 1 atmosphere) suggests that

charge transport during the early stages of pulse development is due to the atomic xenon ion, Xe^+ , consistent with the conclusions of other authors [59-61]. Ellis et al [62] found the mobility for this ion to be around $0.43 \text{ cm}^2/\text{Vs}$ at $E/p = 33 \text{ V/cm torr}$. Mobility is known to decrease slowly with increasing field strength [62,63], and in the chamber used E/p had a maximum value of 105 V/cm torr at the anode surface. The value obtained is thus not inconsistent with the measurement of Ellis et al. At low fields and after long periods (tens of microseconds), however, the ion species appears to be Xe^{2+} [64].

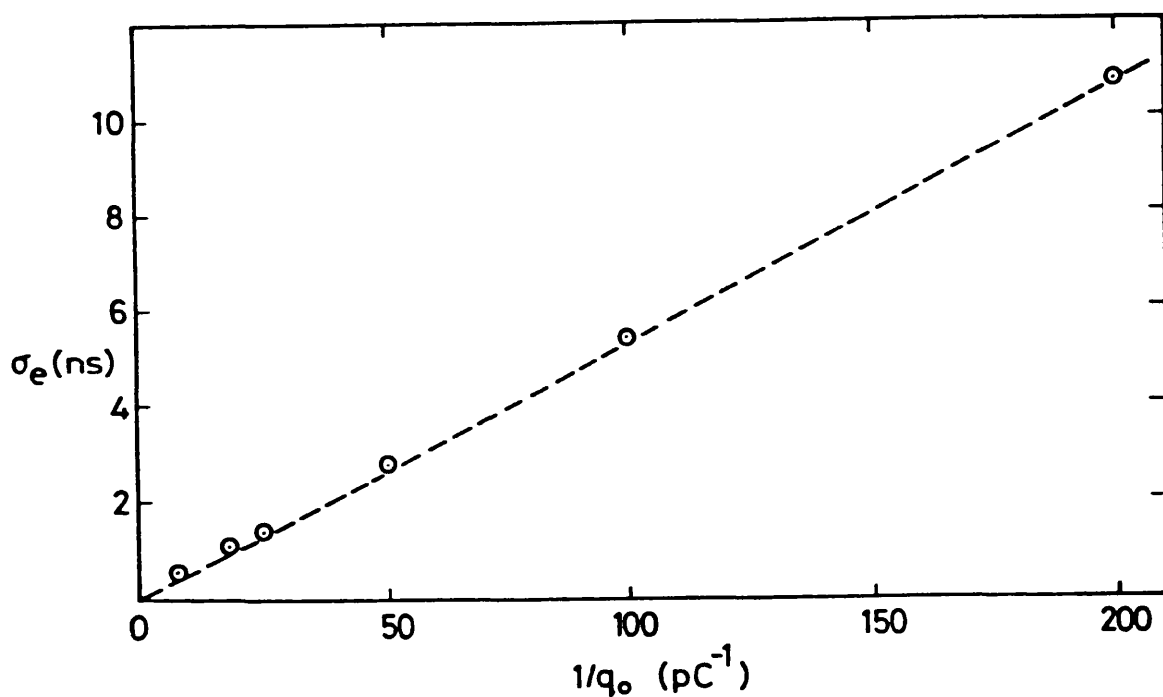


Fig. 3.4 Rms width of cross-over spectrum plotted as a function of $1/q_0$, where q_0 is the step input charge. The broken line is the theoretical relationship derived from the measurement of rms equivalent noise charge, q_n , and of the system time constants.

Assuming $\tau \approx 0$ for x-ray events, then theoretically $A_1 = 3.8 \mu\text{s}$ and $A_2 = 4.5 \mu\text{s}$ (giving $A_1^2 + A_2^2 = 35$). These values are much greater than those resulting from a step pulse input since these parameters are inversely dependent on the gradient of the waveform as it crosses the threshold discriminator level or the zero level, and the slower chamber signal increases the risetime and falltime of the shaped pulses.

A_3 can be calculated from the spread in start pulse height corresponding to the width of the acceptance energy window. Taking the rms width of the pulse height spectrum this gives a theoretical value of 0.25 ns.

Experimentally (see Fig. 3.5) $A_1^2 + A_2^2 = 35$, in agreement with the theoretical value, while $\sigma_0^2 + A_3^2 = 1.5 \text{ ns}^2$, which, assuming the theoretical value obtained for A_3 is valid, implies $\sigma_0 \approx 1.2 \text{ ns}$. This represents the rms fluctuation in τ , so τ itself is clearly only of the order of a few nanoseconds, which has a negligible effect on the chamber pulse. The original assumption that $\tau \approx 0$ is therefore valid.

In fact the values of A_2 and A_3 are dependent on the threshold used to provide the start pulse, A_3 increasing with increasing threshold while A_2 is inversely dependent on the gradient of the waveform at the discriminator level. This level will always be below the point of inflection of the leading edge of the start pulse waveform, so in practice

A_2 is inversely related to the threshold. Since A_3 contributes directly to σ_e while A_2 is related via $1/q_0^2$, the optimum threshold is also dependent on the operating charge level, and a relatively high threshold will also reduce the dependence on q_0 .

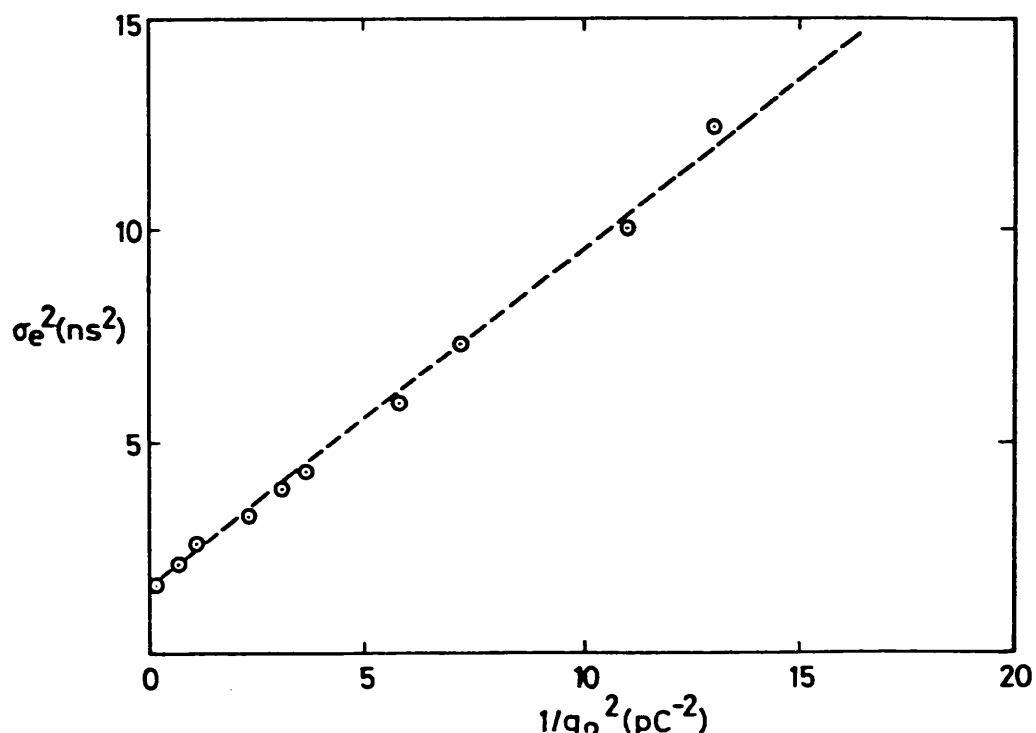


Fig. 3.5 Square of the rms width of cross-over spectrum for x-rays (22 keV) plotted as a function of $1/q_0^2$, where q_0 is the chamber avalanche charge. The gradient of the broken (theoretical) line has been determined theoretically, but the intercept has to be assumed.

For background events (simulated using a Co^{60} γ -ray source) the average experimental value of t_e (as defined by the centroid of the background cross-over spectrum) was found to be 0.16 μs longer than for x-ray events. The values of b_2 (Eqn. 3.2) can be calculated as a function of τ , and so, by a process of iteration, the value of τ required to match the measured value of t_e can be

calculated. This was found to be $\sim 0.4 \mu\text{s}$, and treatment similar to that employed for the x-ray spectrum shows that the measured value of σ_t ($\sim 0.23 \mu\text{s}$) is almost entirely due to real variations in t_e because of varying track orientations and extensions, with only a small contribution from A_1 , A_2 and A_3 .

3.3.2 Discrimination

Fig. 3.6 shows the cross-over spectra obtained for x-ray and background events. The rms spread of the x-ray peak ($\sim 1.8 \text{ ns}$ at the operating charge level $q_0 = 0.67 \text{ pC}$) is small compared to Δt_e ($\sim 160 \text{ ns}$), enabling a good level of background rejection to be achieved.

Fig. 3.7 shows the signal and background acceptance ratios (R_s and R_b) and the discrimination performance (as defined in Chapter 6) as a function of the discriminator level. The minimum of this function is shallow, and any threshold for which $R_b < 8\%$ and $R_s > 90\%$ provides comparable performance. In fact, the optimum occurs where $R_s \approx 94\%$ and $R_b \approx 5.5\%$, which compares favourably with results quoted by other workers [50,52,55].

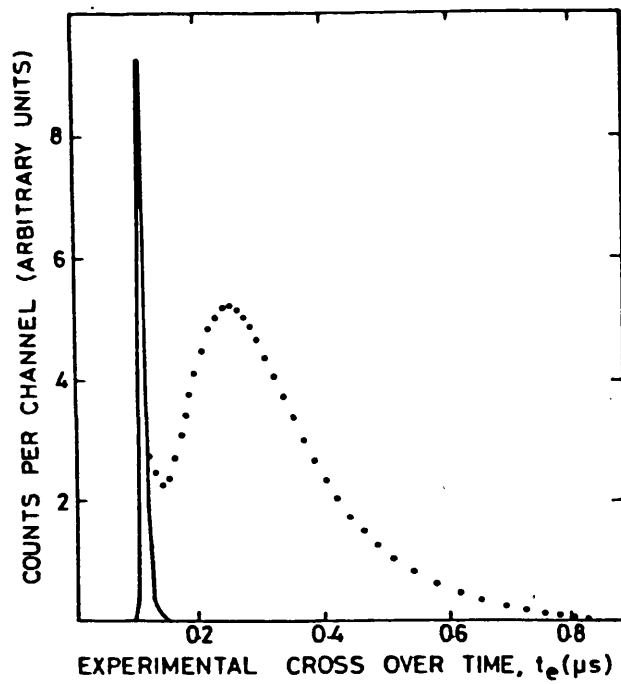


Fig. 3.6 Experimental cross-over spectra for x-rays , continuous curve, and for simulated background (from Co^{60} source), dotted curve. The time axis origin is at an arbitrary position.

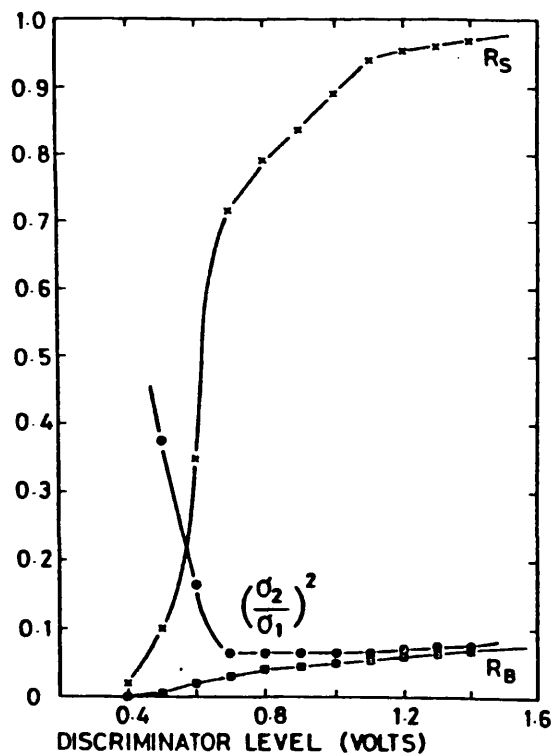


Fig. 3.7 Efficiency ratios R_s for x-rays, and R_b for background, plotted as a function of discriminator level. The system performance figure, as defined by Eqn. 6.5, is also shown.

Chapter 4

Ion Mobility Measurements

4.1 Theory

As mentioned in the previous chapter, matching a computer calculation of the amplifier waveforms to the observed forms for a step pulse input allows the filter time constants to be established. The chamber characteristic time, t_0 , can then be determined by matching the waveforms observed from the chamber, and this then allows the ion mobility, μ , to be calculated from the relation

$$t_0 = \frac{r^2}{4\mu CV_a} \quad \text{Eqn. 4.1}$$

The value of μ obtained by this process will be the average value of the mobility of the ions during the time interval between the start of the formation of the chamber signal and the point corresponding to where the ion motion no longer contributes to the pulse (as explained in Chapter 2). This time is dependent on the amplifier time constant, and so by using different filter times the mobility can be measured over different time intervals, and thus over different average field strengths.

The average velocity of the ions during this period, $\bar{v} = \bar{E}\bar{\mu}$, and, from Eqn. 2.1

$$\bar{v} = \frac{2CV_a \bar{\mu}}{\bar{v} t_f} \quad \text{Eqn. 4.2}$$

where t_f is the time of flight of the positive ions. This allows the mean ion velocity to be calculated, and hence the radial position, r_f at time $t=t_f$, the field at this point, and finally the average field strength in the region $r_a < r < r_f$.

To this end, the resulting waveforms from an RC-CR-CR filter were measured for step input pulses and for chamber events. In each case the integration time and differentiation times were equal, and could be set to nominal values of 0.2, 0.5, 1.0, 2.0 or 5.0 μs .

4.2 Results

The results obtained assuming t_f is equal to the integration time constant T_x are summarised in Table 4.1 and in Fig. 4.1.

The measured values are clearly consistent with those quoted by other workers [49,58,61,62,64,65], but suggest that the dominant ion species changes from the atomic ion Xe^+ to the molecular ion Xe^{2+} between 70 V/cm Torr $> E/p >$ 60 V/cm Torr ($0.5 \mu\text{s} < t_f < 2 \mu\text{s}$). This is again in broad agreement with Varney [58] and with Charles and Gott [59],

though the charge transfer apparently occurs rather more rapidly than is reported by the latter authors, even allowing for the greater chamber gas pressure in this case. Charge transfer from either xenon ion species to the CO₂ quench gas is energetically unfavourable and thus presumably does not occur.

Nominal T_x (μ s)	Calculated T_x (μ s)	Pulser t_r (μ s)	Chamber t_r (μ s)	t_o (ns)	Mobility cm^2/Vs	v m/s	r μm	E/p V/cmTor
0.2	0.22	0.128	0.20	48	0.163	170	37	74
0.5	0.445	0.222	0.32	44	0.178	126	56	69
1.0	1.07	0.403	0.55	26	0.301	106	114	62
2.0	2.17	0.704	1.00	20	0.391	85	184	59
5.0	5.9	1.70	2.3	23	0.340	48	283	57

Table 4.1 Calculated values of the chamber characteristic time (t_o), ion mobility (μ), ion drift velocity (v), and reduced field (E/p). The mobilities, velocities and reduced fields are the average values assuming a time of flight equal to the calculated amplifier time constants. In this time the ions cover a distance r .

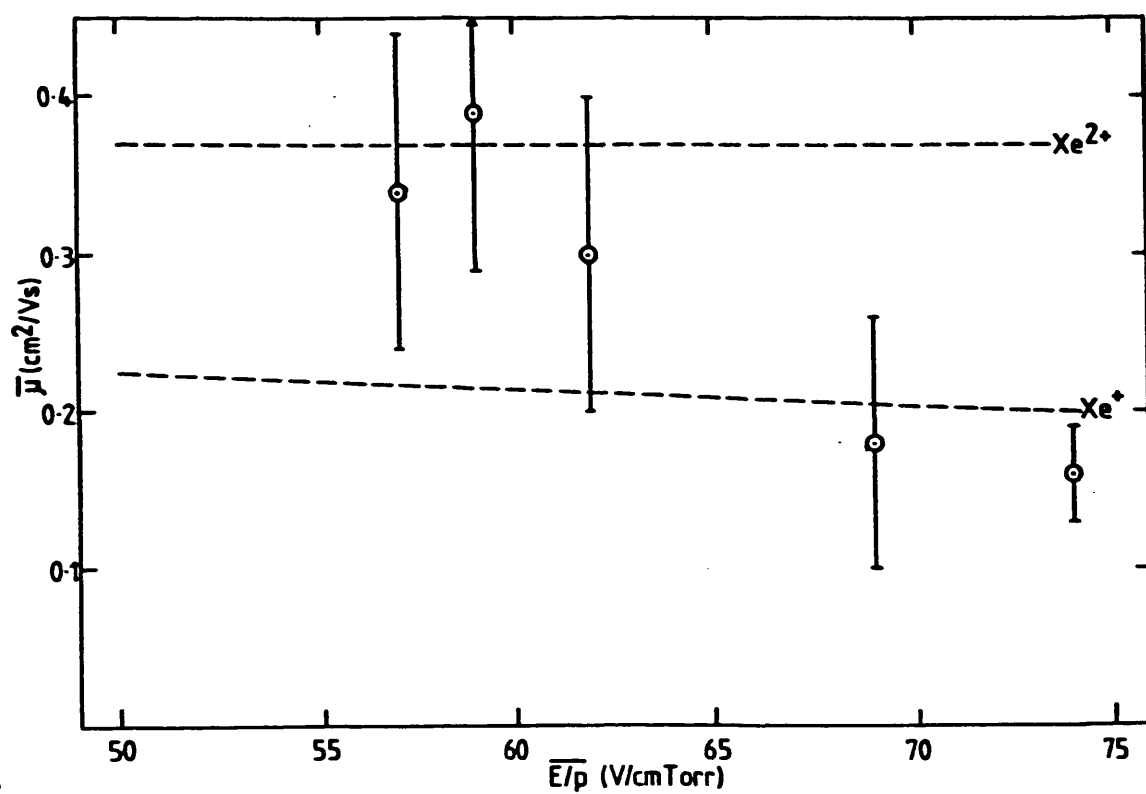


Fig. 4.1 Experimental values of positive ion mobility plotted against the reduced field E/P . The curves are from [49,66]

Chapter 5

Radiation Protection Monitoring

5.1 The radiation hazard

When radioactivity was first discovered it was regarded as a curing and animating property for human beings, and the healing properties of many natural spring waters were believed to be due to the trace amounts of radioactive substances they contained. However, harmful effects became apparent from effects noticed in luminous dial painters in the watch-making industry, and from deaths in the radium manufacturing industry in the 1930s. The connection between radiation exposure and cancer had been recognised by the time of the Second World War, and it is now usually assumed that very small volumes of radioactive substances deposited in the body can lead to serious damage of the organism, and possibly to death.

The population has always been exposed to naturally occurring radiation, but since the beginning of the atomic age the increasing production and usage of artificial and natural radioisotopes for weapons, nuclear power, industry, scientific research and medicine, has appreciably altered the chance of increased exposure to a large proportion of the population, particularly, of course, to those people

working in these fields. The determination of the total body content of incorporated radioactive substances is thus of ever-increasing importance.

The largest body of evidence on the effects of radiation poisoning comes from the epidemiology of cancers in luminisers, so it is also necessary to determine the content of natural radionuclides within the human body to identify what level of contamination produced the observed effects, and thus establish maximum permissible burdens (MPB). Safety standards for health protection of the general public and of workers were approved by the Council of the European Communities on 15th July 1980 [67].

One of the most important radionuclides with regard to internal contamination is plutonium, an α -emitter of long physical half-life. The only naturally occurring isotope is Pu^{239} , but much present day plutonium is produced artificially from uranium by neutron capture. Under these conditions the resulting material contains Pu^{239} , plus appreciable quantities of Pu^{240} and Pu^{241} produced by successive neutron capture during irradiation. Pu^{241} decays by β emission with a half life of 13.3 years to americium, so that the latter can build up to a considerable extent in a few months after the plutonium extraction. Plutonium decays by α emission to form uranium, which produces L x-rays of energies 13.6, 17.2, and 20.2 keV with yields of 1.67%, 2.38%, and 0.55% in the case of Pu^{239} (see Table 5.1). Am^{241} emits a 60 keV γ -ray in addition, with a

Table 5.1). Am^{241} emits a 60 keV γ -ray in addition, with a yield of 36%. The annual limits on intake of plutonium, as specified by the ICRP, are shown in Table 5.2.

Plutonium isotope	Specific activity Bq/ng	x-rays per alpha
238	633	0.115
239	2.30	0.0465
240	8.41	0.108
241	0.094	-
242	0.145	0.100

Table 5.1 Specific activities and x-ray emissions from the major plutonium isotopes [69]. That for Pu^{241} is for α decay only.

Metallic plutonium has a density of 19.9 g/cm^3 , and melts at 640°C . It is an actinide, atomic number 94, and has III, IV, V, or VI valence states. The IV state is the main oxidation state. Plutonium is insoluble as oxides, fluorides and oxalates, and is extremely insoluble as the hydroxide [68].

In the range pH 1.5-2.8 Pu^{IV} ions begin to hydrolyse and near pH 7 it is completely complexed with proteins or other constituents of body fluids, and forms polymeric products. Plutonium in blood is bound to transferrin, one of the specific proteins in blood serum. In the liver plutonium may be bound to ferritin [68].

Soluble plutonium compounds form an insoluble hydroxide in the gastrointestinal tract. But the plutonium may form stable soluble complexes with chelating ligands (eg DTPA), which compete successfully for the binding of plutonium from transferrin [68]. When these complexes are formed in blood plutonium is readily excreted in urine. This is the basis of chelation therapy for removal of plutonium from the blood, but since it is inoperative against intracellular plutonium the effect is not complete.

Plutonium isotope	Inhalation		Half life
	$f_1=1 \times 10^{-4}$ (Class W)	$f_1=1 \times 10^{-5}$ (Class Y)	
234	8×10^6	7×10^6	9 hrs
235	1×10^{11}	9×10^{10}	26 mins
236	7×10^2	1×10^3	2.9 yrs
237	1×10^8	1×10^8	45 days
238	2×10^2	6×10^2	86 yrs
239	2×10^2	5×10^2	24,000 yrs
240	2×10^2	5×10^2	6,580 yrs
241	1×10^4	2×10^4	13 yrs
242	2×10^2	6×10^2	4×10^5 yrs
243	1×10^9	1×10^9	5 hrs
244	2×10^2	6×10^2	7.5×10^7 yrs
245	2×10^8	2×10^8	10 hrs

Table 5.2 Annual Limits on intake, ALI (Bq) for plutonium isotopes [67].

5.2 Plutonium metabolism

Plutonium can enter the body by three processes:

- 1) ingestion, the bulk of which will be rapidly excreted
- 2) through a wound, and thence into the blood supply
- 3) inhalation via the lungs.

Inhalation is generally considered to be the main source of plutonium internal contamination.

The deposition of inhaled plutonium depends on various physical parameters, such as particle size, shape and density [70-73,115], and also on certain physiological considerations, such as tidal volume (the volume of air moved with each inspiration or expiration), breathing rate, and air flow rate [74]. Some particles will remain in suspension in the air, and will be exhaled. Many of the smaller particles will be quickly distributed throughout the lungs via the bronchi and bronchioles, but it is likely that appreciable quantities of any larger particles will be deposited in the upper bronchi.

Once deposited the agent can follow 3 major pathways: it may be raised by ciliary action and swallowed; absorbed into the blood; or remain in the lung with a certain finite residence time, removal being either by one of the aforementioned pathways or by phagocytotic action via the lymphatic system. Particles removed by this process will accumulate in the lymph nodes surrounding the upper bronchi and lower trachea (Fig. 5.1). Translocated material in the lymph nodes may reach concentrations 50-100 times greater

than those in the lung volume about 10 years after exposure, though biological evidence has not yet indicated that the concentration of material in the lymph nodes is detrimental to the well-being of the organism [75]. In principle intra-oesophageal detectors can be used to monitor such a concentration [68], though this would be unacceptable in practice.

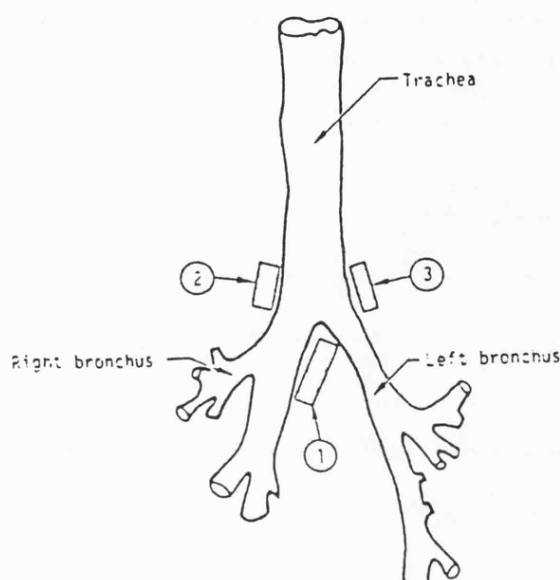


Fig. 5.1 Schematic diagram of the lower trachea, bronchii and the carina (1), and right (2) and Left (3) tracheobronchial lymph nodes.

The translocation of material from its original point of deposition is also dependent on the physical properties of the particles [74], and is further influenced by the total burden (greater biological half-lives are observed for greater burdens in animals [76]), the chemical properties of the contaminant (particularly its solubility) and the point of deposition [67,71,72,77]. Autopsy data suggest that plutonium is fairly uniformly deposited throughout the lung

at reasonably short times following exposure [78]. As time passes there seems to be concentration in some subpleural regions either by migration toward the pleura or preferential elimination from the parenchyma, or by a combination of both processes [75,78].

The ICRP has produced generalised models of material translocation for use in situations in which specific data is lacking [67,73]. The older, simple model [73] assumes 25% of the inhaled particles are exhaled, while 75% are deposited in the respiratory system, 2/3 of which are deposited in the upper respiratory tract (nasal passages, trachea and epithelium of the bronchi), rapidly removed from these sites to the throat by ciliary action and swallowed. Cilia can move particles up the bronchi and bronchioles at 0.15-1.0 cm/min and up the trachea at 3-4 cm/min [72], so these particles are rapidly cleared from the respiratory system. The remaining 1/3 (representing the smaller sizes) is deposited in the lower parts of the lung. 1/2 of these will also be elevated and swallowed within 24 hours, while the other 1/2 is transferred to body fluids with a biological half-life of 300 days. Other researchers [eg 79,81] are not in agreement with these figures. In the more recent model [67], the deposition pattern is assumed to vary with particle size, the possibility of translocation to the lymph nodes is recognised, and some clearance half-lives have been adjusted. This model predicts, for an intake of 1 μm particles of PuO_2 at the annual limit of 500Bq, a deposit available for detection of 75 Bq.

DEPOSITION

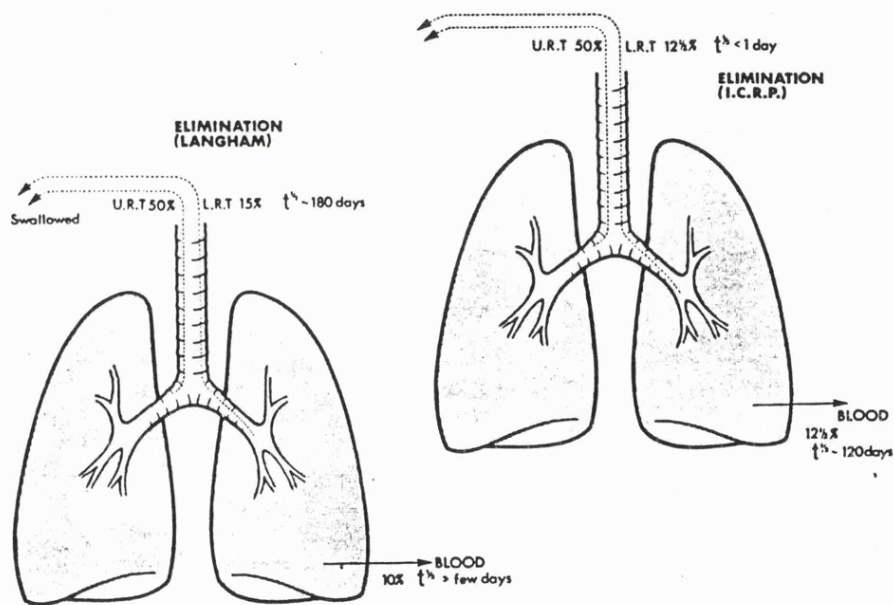
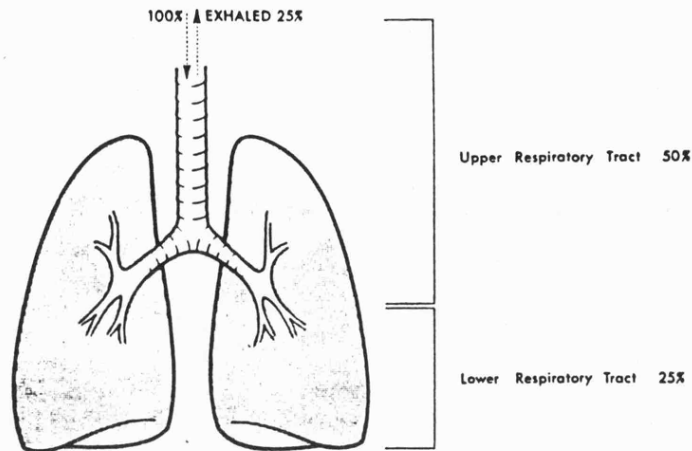


Fig. 5.2 Schematic diagram of the ICRP and Langham lung models [72].

Of the material swallowed, a small fraction may be absorbed into the blood. This fraction, f_1 , is strongly dependent on the chemical form of the plutonium - 2% for

soluble complexes (such as chelates), $3 \times 10^{-3}\%$ for soluble compounds, $10^{-4}\%$ for most other compounds, and $10^{-5}\%$ for the almost totally insoluble oxides and hydroxide [67,68,81]. These values are subject to considerable variation from individual to individual, and have also been shown to be dependent on the subject's age [67]. However, generally little absorption takes place, so most of the swallowed plutonium is directly excreted in the faeces.

Once in the blood stream material will either be deposited in tissue for a certain period or directly excreted in the urine. The relative deposition of plutonium from the blood has shown a considerable variability in human autopsy and experimental animal data, but accepted values are 0.45 fractional deposition in the liver, 0.45 deposition in bone, and 0.1 in other tissues and lost through early excretion [67]. The rate of urinary excretion is thus very small, and shows some dependence on the size of the contaminating particles, being greater for the smaller particles that are more readily absorbed into the blood [73,77]. The biological half-life is ~100 years for retention of plutonium in the skeleton and ~40 years in the liver [67,68]. Fractional translocation to the gonads is 3.5×10^{-4} for males, 1.1×10^{-4} for females ($\sim 10^{-5}$ per gram of gonadal tissue) for which retention is essentially permanent [67].

Radionuclides in true solution and those in soluble compounds behave in a similar fashion, but any large

colloidal complexes will be deposited in the lymph nodes, spleen, liver, and bone marrow as a result of phagocytosis [77]. Systemic radionuclides are gradually excreted by continuing exchange with stable isotopes of the same or diadochal elements.

Uptake of plutonium by the skeleton is initially restricted to the endosteal surfaces of mineral bone, and radioisotope deposition on the sensitive tissues of bone surfaces is known to induce bone tumours [82]. The plutonium is then slowly redistributed throughout the bone by processes such as resorption and burial [67], which can result in a severe radiation dose to the bone marrow.

Due to the long biological half-life of systemic plutonium, prolonged irradiation results from internal contamination, regardless of any subsequent precautions against further intake, and the high level of deposition in bone and liver and the long retention time make them critical tissues for plutonium contamination.

5.3 Means of detection

Generally, when an acute accidental intake of a radionuclide is known to have occurred, the primary object of any subsequent investigation is to estimate the radiation dose to the tissue of the body and, in particular, to the critical organ.

Although the skeleton and liver are the important locations of long-term plutonium contamination, it is not feasible to measure directly the burden in these places due to the limited amount of penetrating radiation from plutonium and the depth of tissue coverage. Neither would it be desirable to rely on such measurements since contamination builds up very slowly in these tissues after exposure. Instead, the potential systemic burden must be estimated before deposition occurs, either by bioassay or by direct counting of the penetrating radiation escaping through the chest wall from material deposited in the lung.

Bioassay involves measurement of the radiation content of the breath, faeces or urine. The interpretation of any results involves assumptions about how the elimination from the body represents the material deposited inside the body. There are well established retention and excretion functions for various soluble radioisotopes, but the behaviour of plutonium in the body is very complex. Estimates of the lung burden are thus linked to the rate of excretion by very complicated metabolic models, which depend on many parameters that are difficult to determine.

Considerable effort has been invested in attempting to determine plutonium excretion functions [68,71-73,77,83-85]. The initial rate of urinary excretion following an intake is not only very small due to the insolubility of plutonium (the intake of 1 MPB will result in the excretion of about 4 pCi/day (0.15 Bq) in the urine 2 months after exposure

[83]), but is also very dependent on the rate of release from the site of entry, as well as on the total systemic burden.

After about a year, when a small proportion of the contaminant has been metabolised, the excretion rate is less dependent on the rate of release, allowing a more reliable estimate of the body content to be made. The long-term excretion rate follows a power law [77]. In consequence there is no constant relationship between the urinary excretion rate and the body content, even following a single intake. This relationship becomes still more difficult to define if more than one intake has occurred. Hence an individual result does not provide a definitive burden measurement; all the previous results must also be brought into consideration in order to make a provisional estimate of the body content.

The degree of confidence of such an estimate depends on the nature of the contaminant and it can be assumed that a significant lung content could exist without the daily urinary level being consistently above the level of detection now achievable. Results are believed to be accurate to within a factor of about 2. In principle urine analysis only gives information on the systemic burden, though it has been suggested from rat studies that the initial lung content will be 10 times this value [84].

Levels of plutonium encountered in faeces following an inhalation exposure are normally orders of magnitude higher than those encountered in urine due to the rapid and usually massive clearance via the faeces of material deposited on the ciliated epithelium of the trachea and bronchi. However, interpretation of results is still dependent on complicated metabolic models.

An alternative method makes use of the ratio of the urinary to faecal excretion rate [84]. Both these methods require ~10 days after intake to allow for the initial clearance via faeces and for the "soluble" material to enter the systemic circulation and organs of deposition.

Bioassay methods are generally favoured in the routine, precautionary monitoring of exposed personnel for plutonium, such as through the collection of several days' output of urine at 3-6 month intervals. They provide the most sensitive indication of intakes through undetected low-level releases into the working environment, even if metabolic and other uncertainties make quantification of the intake imprecise. If a positive result appears, bioassay may be supplemented by the direct measurement of a lung deposit with counters viewing the chest. This latter approach would certainly be required after a known incident leading to airborne contamination, giving prompt indications of any large intake and the need for medical intervention. Chelation therapy is more likely to be effective if applied within hours of intake [86], whereas bioassay, involving

radiochemical procedures taking perhaps 24 hours, cannot give this early indication. Bioassay would still be appropriate, to establish the pattern of excretion for assessment of the integrated radiation dose from a known intake, and to provide metabolic data potentially useful in the evaluation of other cases. Where direct methods are applied periodically as routine procedure, despite their inherent insensitivity, they are used as an adjunct to other methods of control, primarily for reassurance that no significant burden has accumulated through long-term low-level exposure and escaped detection by other tests.

In vivo measurement is easy for γ emitters such as U^{235} , I^{131} , and Cs^{137} , which provide enough penetrating radiation to be detected by scintillation counters down to levels orders of magnitude below the MPB [87], typically 10-100 pCi (0.4-4 Bq). However, it is difficult to apply this technique in the case of plutonium isotopes because they emit very little penetrating radiation, the γ -rays having yields varying from 6×10^{-6} down to 10^{-10} . Instead, the uranium x-rays of 13 to 20 keV must be detected. About 60% of these x-rays will be absorbed in the lung itself. Bone, which covers approximately 40% of the frontal surface of the thorax, is essentially opaque at these energies, and the soft tissue of a typical chest wall (say 28mm thickness) will cause attenuation by a factor of ~25. About 1% of the emitted x-rays thus escape and can be detected [88]. It is therefore almost impossible to detect the systemically deposited plutonium in the skeleton, and direct assessment

is mainly limited to the content in the lung, and in some cases the liver.

A further possibility is by detecting the 60 keV γ -ray of Am^{241} (458 year half-life, 36% yield) produced by the decay of Pu^{241} . Assuming the ratio of the activity of the americium to that of the plutonium is the same in vivo as in the contaminant, the plutonium burden can be assessed by measurement of the americium. An estimate of this ratio may be obtained from analysis of material excreted in the faeces within the first few days after intake. Currently ~ 0.1 nCi (4 Bq) of americium can be detected in the lungs, which, for aged plutonium, corresponds to a few 100s of Bq of Pu^{239} [73]. This is subject to the assumption that plutonium and americium behave similarly in the body which is only true preabsorption. There is also, however, evidence of slight preferential loss of americium from the lung and lymph nodes and of uptake by the liver [84].

Americium also produces x-rays of similar energy to the U L x-rays, but with a 40% yield. Presence of americium can thus lead to an overestimate of the lung burden unless the composition of the contaminant is known or the 60 keV peak is measured.

Two methods involving irradiation of the subject have also been considered [84]:

- a) excitation of induced plutonium K x-rays
- b) neutron induced fission, which produces Xe^{138} which may

then be detected in the breath. Alternatively the prompt fission γ -rays, particularly that produced with an 11.3% yield at 139 keV, may be measured, or the delayed neutrons (those emitted by the fission products).

These methods obviously require irradiation of the patient (by 0.1-1 rem (1-10 mSv) of neutrons) and would only be of use if they offered significant improvement in the detection limit, for which there is as yet no evidence.

5.4 Detector criteria

The primary ability any detector used for chest counting must have is the capacity to measure signals that produce much lower count rates than does the background.

Since only about 1% of the uranium L x-rays escape through the chest wall, a detector with a 10% geometrical efficiency will see between 0.2 and 0.3 counts per minute from a lung burden equal to the retained annual limit on intake (RALI - see p.52) of 75 Bq of Pu^{239} . This tiny signal will have to be detected against a background rate that will be one or two orders of magnitude higher in even the best shielded detectors due to other radioactivity from the subject's body.

Numerous radioisotopes are present in the body in too little quantity to be detected, but the major contributors are the γ emitters K^{40} , Cs^{137} and Cs^{134} , which are soluble in body fluids and thus well dispersed throughout the body, mainly in muscle. Compton scattering of the high energy photons they emit may produce photons which will be counted in the low energy monitoring region. These photons can also be Compton-scattered in the detector and produce electrons in the same energy region.

The body content of potassium is fairly consistent, at about 140 g [67], but that of Cs^{137} is subject to temporal and local variations [89]. Levels rose in the 50s, and fell in the 60s, in parallel with the frequency of atomic weapons tests, and rose again in 1986 as a result of Chernobyl. It is also dependent on dietary considerations, so that, for example levels tend to be lower in oriental races who have a rice-based diet, and higher in the west due to the greater intake of dairy products.

The size, or rather the extent of the active area, of the detector is an important consideration. Large counters, apart from having a greater geometrical efficiency, also have the advantage that the count rate becomes less sensitive to the geometrical variations of the plutonium distribution inside the lung. The reasonable increase in area is limited by the geometrical dimensions of the source to be monitored, in this case the human chest. Increase in detector thickness is stopped as soon as a

considerable fraction of the incident radiation is absorbed, but all measures directed toward an increase in counter efficiency are only effective if, at the same time, the background is not considerably increased. It is also obviously essential to minimise attenuation in the counter window, by appropriate choice of materials and minimising window thickness.

Further requirements include:

- i) total energy deposition and collection in the active region
- ii) good energy resolution
- iii) low background
- iv) stable operating characteristics
- v) independence of the result on the subject's build
- vi) calibratable results
- vii) long-term stability
- viii) reproducibility of results
- ix) relative insensitivity to inhomogeneous contaminant distribution
- x) comfort for the patient
- xi) a short measuring period

This last consideration is particularly important for routine health monitoring applications, since it is not economically viable for workers to spend long unproductive periods under assessment at frequent intervals. When investigating a possible incident, it is reasonable to allow for greater measurement times, though of course speed is

still a consideration if a large number of people require monitoring.

5.5 Detector technology

The first basic equipment required for in vivo measurement is a screened environment to reduce the natural background radiation. The room in which the detector is mounted and in which measurements are taken typically has walls of 8 inches of pre-atomic steel, though some laboratories use 4 inches of lead. This is very efficient at absorbing radiation, but produces the 75 keV Pb K γ -ray. The lead walls are thus coated with a layer of cadmium, which absorbs this γ -ray, but produces its own characteristic x-ray at 22 keV. Some laboratories then use a copper or iron coating to absorb these x-rays, but they have been shown to be negligible in the screened room at the Body Radioactivity Measurement Section at AERE Harwell, presumably because of screening by the detector housing and by the subject's body [90]. The most penetrating component of cosmic rays at sea level is the ionising muon, and a 511 keV peak is produced by positron annihilation.

Even in the best shielded rooms there is always a certain flux of γ -rays from the shield itself and from other necessary objects. For this reason, when an object is placed near the detector to be counted, the background is always changed as a result of the passive action of the

object as a scatterer.

Determination of the amount of incorporated radionuclides by external direct measurements of radioactivity goes back to the early 1930s, when the first cases of radium poisoning were examined by means of ionization chambers, in order to investigate the distribution of the incorporated radon [89]. These detectors were not very sensitive, and in the 1950s an order of magnitude improvement was attained by use of high pressure ionization chamber and later by use of scintillation detectors.

The high intrinsic efficiency of solid absorbers makes possible the high counting rates on which the achievement of high statistical efficiency depends. Spectrometric properties arise from the nearly proportionate conversion of secondary electron energy into light and the conversion of the light flashes into electrical pulses by a photomultiplier tube. These pulses can then be analysed for amplitude and counted to give a pulse-height distribution which is related to the original photon spectrum.

NaI has a high absorption coefficient for γ -rays and has the highest energy conversion efficiency of any phosphors. A 0.25 mm NaI crystal has 95% efficiency for detecting U L x-rays of perpendicular incidence, though of course the effective efficiency is higher since most

incident rays follow longer paths through the crystal. This enables thin NaI crystals to be used and the reduction in material reduces the background without significant loss of signal. However, Compton events occurring in the body or walls of the detector are seen as low energy photons, but it is possible to use a backing of CsI to provide anticoincidence pulses. This is known as the phoswich (dual crystal detector), and is the most commonly used detector for chest counting. A typical phoswich consists of a thin (1-3mm) crystal of NaI(Tl) backed by, and optically coupled to, a thick (eg 50mm) crystal of CsI(Tl). The combination is usually viewed by a single photomultiplier tube. The difference in decay time of the light from the two crystals permits the exclusive detection of events which occur in the thin crystal (ie low energy quanta such as U L x-rays) while reducing the response to scattered higher energy photons. Typically the background can be reduced by a factor of 2-5 for a 10% loss of signal [91], which results in low background at low energies while maintaining high detection efficiency. Large area thick NaI detectors have a higher background, and thus a higher detection limit at low energy, though they are still used as the standard whole body counters for γ emitters.

Various factors affect the overall resolution of a phoswich detector, and among them efficient collection of light is paramount. The scintillator must have good optical transparency and be surrounded by material of high reflectance if scintillations arising in different parts of

a large crystal are to reach the photomultiplier with equal effectiveness. The number of photomultipliers used to collect the light and the uniformity of the photocathodes play a further part, and the photomultipliers must, of course, have stability of performance and, if there is more than one, they must be matched to produce a given photopeak at the same point on the pulse-height scale.

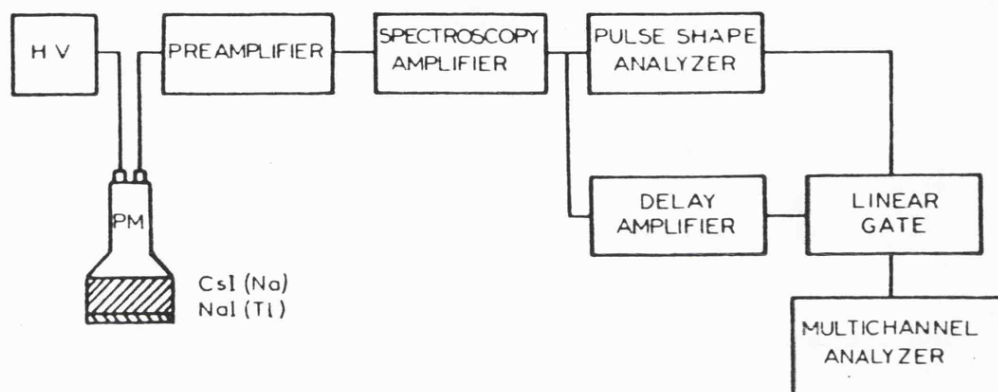


Fig. 5.3 Schematic diagram of a phoswich detector system [73].

Background can also be generated by radium and potassium in the photomultiplier glass envelope and the tube bases, and a small amount is produced by radioactive potassium in the crystal.

Paired 12.5 cm phoswich detectors viewing one lung each seem to be most useful for the routine measurement of low energy x-ray emitters in the lungs [73]. This is because the sternum is essentially opaque to x-rays of this energy, so little signal is lost by not viewing the centre of the rib cage.

An alternative is to use semiconductor detectors such as hyperpure germanium or lithium-drifted silicon [86,91-96]. These have excellent energy resolution (~480 eV at 18.9 keV (2.5%) [91]), but lower efficiency, so multiple detectors mounted on a single cryostat are used. The typical background level in a germanium detector is 2-3 times higher than in a phoswich over the same energy band [95], but this is compensated for by the narrower energy window required to cover the U L x-rays. They are, however, very expensive.

Claims of the relative performance of HPGe arrays to that of phoswich detectors differ [86,91-96], but they are generally not thought to offer a significant improvement. An exception would be when energy resolution becomes a significant consideration in addition to sensitivity. If interfering low energy radiations complicated interpretation of spectra from the phoswich, superior resolution would enable unknown or unexpected radionuclides to be identified. High resolution also allows improved estimation of subject background since levels just a few keV from the x-ray photopeaks can be taken.

Evaluation of the depth of plutonium in the body can theoretically be based on the correlation of the changes in the energies of the emitted photons with the depth of the tissue under which the activity is localised. These changes in photon energy are reflected in:

a) a shift in an unresolved photopeak to higher energy resulting from the greater absorption of the lower energy photons by tissue. A linear relationship up to 4 cm absorption depth is found.

b) a spread in the photopeak - reflected in its energy resolution - resulting from the scattering of the emitted photons in the tissue equivalent material. A linear relation with a negative slope for depths of 2 to 6 cm has been reported [97].

Energy resolution is clearly a prime consideration for this purpose, though a dose of several hundred times the ALI would be required to produce adequate counting statistics.

A Si(Li)-Na(Tl) detector combines the superior performance of semiconductor detectors with the background suppression of the phoswich, and a low sensitivity to γ -ray background because of the low atomic number of silicon [96]. This may provide an improvement when fully developed.

Proportional counters have been used for plutonium lung monitoring [eg 50,75,81,86,88,98-100], but the fall-off in counting efficiency with energy means they cannot be used to detect the 60 keV γ -ray of Am^{241} . Their major advantage is resolution, giving the same possibilities as germanium detectors. Choice of counter gas is important. Argon is relatively cheap, enabling a flow counter to be used which overcomes problems of gas degradation, but has a poor

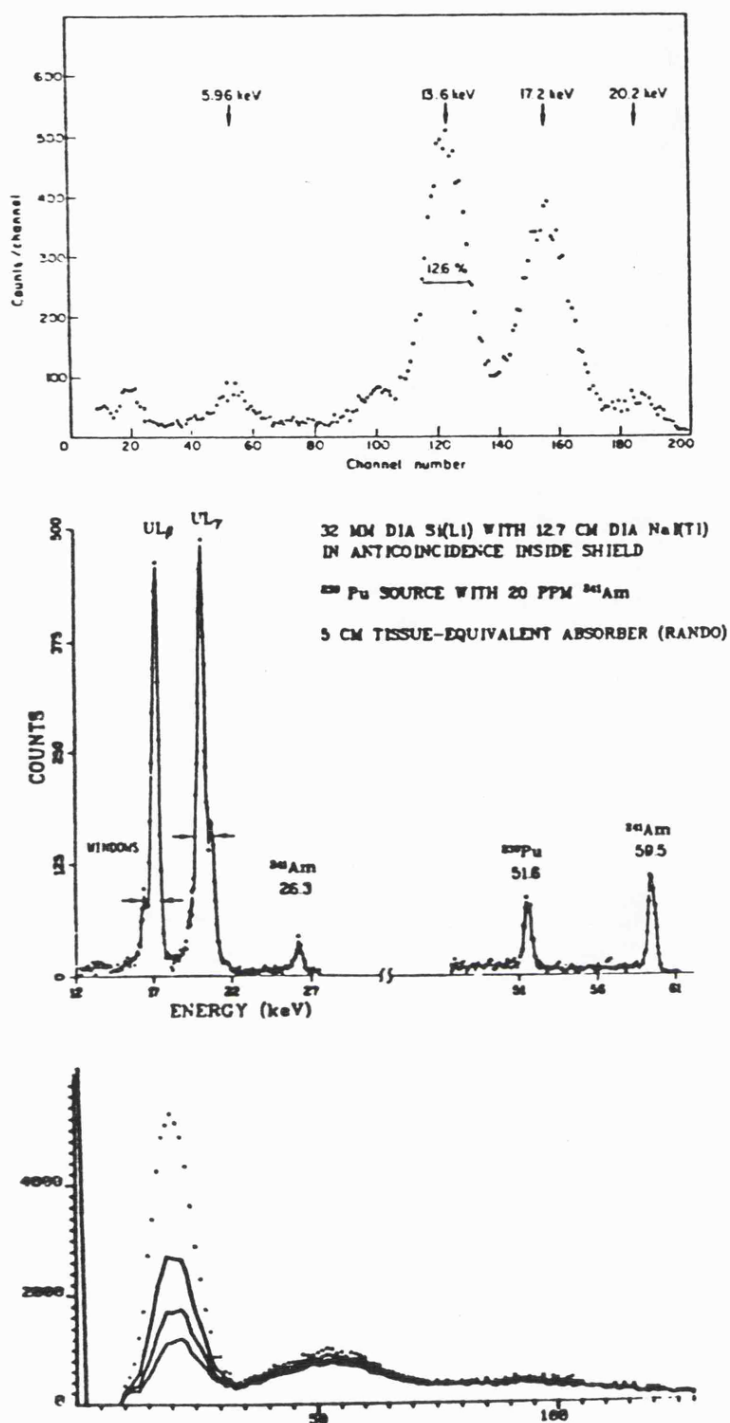


Fig. 5.4 Pulse height spectra for:

- a proportional detector viewing a Pu^{239} source [99].
- a Si(Li)-Na(Tl) detector viewing a Pu/Am source through an absorber simulating 5cm of tissue coverage [96].
- the phoswich detector used at the Body Radioactivity Measurement Section, Harwell, viewing the Livermore phantom (containing uniformly distributed Pu in the lungs), with a chest wall thickness of 20, 25, 30, and 53 mm.

stopping power (5 cm of argon is only 12% efficient for U L x-rays). Xenon is more efficient but is very expensive, so a sealed counter must be used. Krypton is the most efficient (88% for 5 cm), but contains radioactive Kr^{85} , so xenon has been used most frequently.

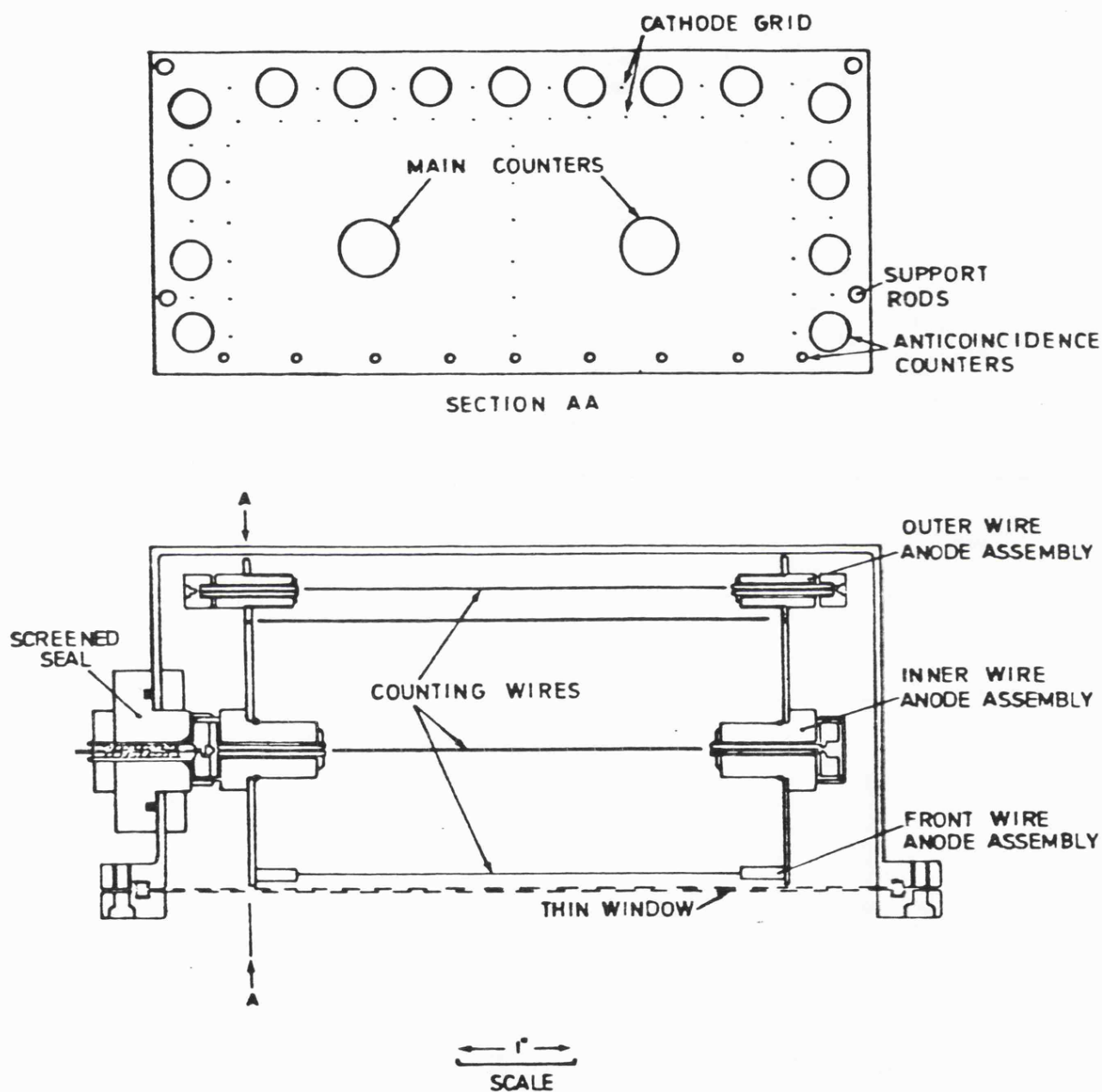


Fig. 5.5 Example of a proportional counter lung monitor [12].

A gas scintillation proportional counter has also been

investigated [101]. This provides ~100 times the light output of NaI, and 10 times better energy resolution, ~3.2% at 60 keV, but problems with radioactivity from the counter materials apparently prevented a meaningful assessment of its performance.

5.6 Calibration

Although counting statistics are a major consideration due to the relative sizes of the signal and background count rates, calibration and systematic errors significantly add to the errors associated with counting. For many purposes absolute measurements of radioactivity are required, and these call for a determination of the relationship between instrument response and known amounts of radioelements in bodies of different mass and size.

This response depends on a number of factors.

a) the specific isotopic composition of the material - the various plutonium isotopes have different x-ray yields, and the americium content is also significant.

b) an accurate assessment of the room background and that contributed by other radioactive materials in the individual - background is predicted either by comparison with non-exposed persons of similar build (estimated accuracy 15% at 2σ [75]) or by correlation of the count rate in an

energy band clear of photopeaks, such as 75-100 keV for a phoswich system (estimated accuracy 10-12% [75]).

c) photon absorption characteristics of the chest wall - chest wall thickness and composition can be assessed by ultrasonic scanning, and equations have been developed to link the effective chest wall thickness to the height, weight, and chest circumference of patient [75]. These equations are believed to be reliable for persons of approximately average build, but are less so for extreme types.

d) distribution of material within the lungs - autopsy data indicate a definite long-term trend of accumulation of plutonium in the outer areas of the lung and in the lymph nodes. The material remaining within the lung therefore becomes more "visible" to the detector with time due to the reduction in absorption within the lung. This distribution can produce a factor of 2.5-3 error in measurement of lung burden, and errors of $\pm 70\%$ can reasonably be assumed for distribution patterns [75]. Generally uniform distribution is assumed, which is reasonable shortly after intake.

e) presence of surface contamination - precount showers and alpha monitoring are used to reduce the possible contribution of surface contamination.

f) distribution in other organs and tissues - the presence of plutonium in the nearby organs and the skeleton can add

to the measured value of the lung burden, though this is more commonly a problem encountered when measuring higher photon energies, such as for Am^{241} .

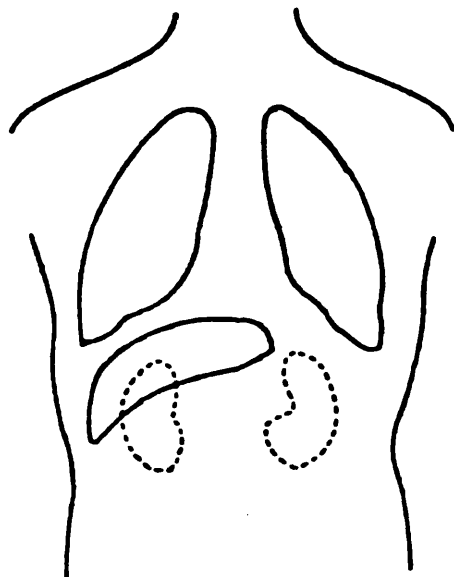


Fig. 5.6 Schematic diagram of the positions of the Lungs, Liver and kidneys.

Once data has been corrected for background, chemical composition etc, results are interpreted by calibration. Whether this is truly representative of the exposed subject is a final uncertainty in the counting procedure.

In principle the best calibration method is incorporating in humans known activities of the nuclides to be monitored, or of comparable short-lived isotopes, but in most cases incorporation is not possible and calibration must be made with a phantom or model. This is straightforward for some isotopes, particularly γ emitters with a homogeneous distribution throughout the body, and it has

been shown [102] that simple perspex cylinders of appropriate dimensions containing solutions of potassium or caesium provide excellent calibration factors. Some laboratories have used cadavers, but these are not ideal since the loss of body fluids alters the level of Compton scattering of photons [70]. Simple laminated phantoms have proved useful in the case of higher energy γ -rays, but are not sufficiently realistic to be of use at 17-60 keV.

To be valid for localised contamination detected by their x-ray photopeaks, this approach requires a phantom which is anatomically realistic and whose relevant organs and tissues are made of materials correctly attenuating the low energy x-rays. Many commonly used plutonium chest phantoms have been shown to be grossly deficient in these respects, leading in many cases to errors in calibration of a factor of 3 or larger [103]. For this reason the Lawrence Livermore National Laboratory undertook the development of a standard anthropomorphic phantom in 1974, which was completed in 1978.

The phantom represents the male thorax, between the 5th cervical and 4th lumbar vertebrae. It's relevant organs and tissues are made of polyurethane loaded with the proportions of CaCO_3 necessary to give the correct attenuation of U L x-rays. The principle internal structures (lungs, mediastinum, liver and surrounding tissues) are contained in a shell of muscle-equivalent material, representing the chest wall. The chest wall

incorporates a suitably loaded polyurethane sternum, rib cage, and vertebrae. The inactive lungs are replaced during calibration measurements by others uniformly impregnated with the nuclide of interest. The mean anterior chest wall thickness (CWT) is typically 16mm in those regions of the upper thorax commonly viewed by detectors in routine x-ray counting for plutonium, but close-fitting overlays of various thicknesses simulating muscle-equivalent tissue, 50/50 muscle/adipose tissue, or 13/87 muscle/adipose tissue are available to take the thickness to 42 mm [104].

The phantom was tested with volunteers inhaling $\text{Nb}^{92\text{m}}$. This produces 15.8 and 17.7 keV x-rays, simulating those from plutonium, and γ -rays that enable the actual activity to be assessed with scintillation counters. Data from Harwell, ANL, LLNL, and PNL suggest that use of the phantom for calibration would not generally lead to major systematic errors, though it is better for twin detectors viewing each lung than it is for one detector mounted above the sternum. Thus, for the most common arrangements of counters, in which paired detectors view the anterior surfaces of the upper thorax, use of the phantom should on average indicate the calibration factor to within 20% [104].

CHAPTER 6

The Prototype Proportional Chamber Lung Monitor

6.1 Chamber design

The chamber has been designed specifically for maximum signal efficiency in the 12-22 keV energy band (covering the uranium L x-rays) coupled with low intrinsic background. This requires the use of a xenon-based counter gas to provide an adequate x-ray stopping power in a reasonable absorption depth, which in turn necessitates the use of a sealed counter simply due to the prohibitive cost of a xenon flow counter. All materials incorporated in the chamber have been selected for minimum radioactive contamination, so, for example, pre-atomic steel had to be used for the chamber casing. The choice of window material also proved difficult. The best source of beryllium that could be found contained 2-4 ppm of uranium plus thorium, which is obviously too great for a detector specifically looking at uranium x-rays. Instead a 0.5 mm carbon fibre window, coated (on the inside) by a 13 μ m layer of aluminium to provide a conducting surface and a good seal, has been used. This allows 91% transmission of x-rays at 15.8 keV, though of course this refers to normal incidence (ie minimum photon path length through the window) and represents an upper limit to the transmission for large distributed sources.

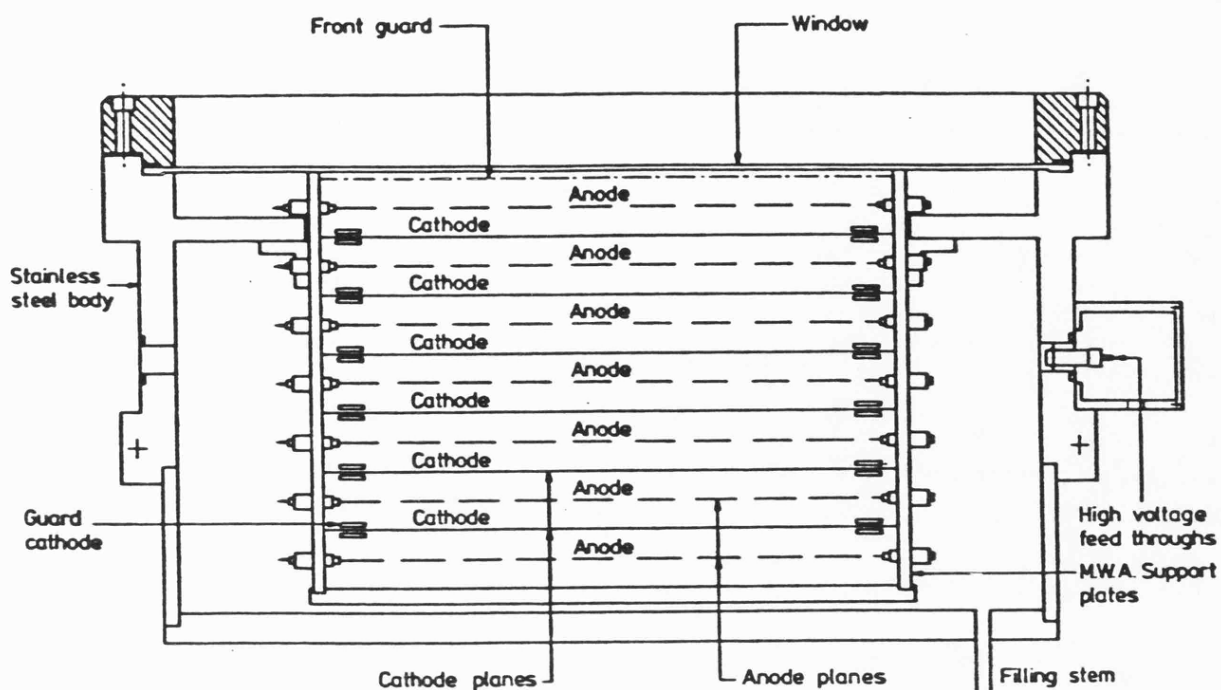


Fig. 6.1 Cross-sectional view of the prototype multiwire lung monitor [88].

The approximate dimensions of the chamber are defined by the purpose to which the counter is to be put - namely, that the depth of the active volume must be sufficient to provide adequate x-ray stopping power, and the sensitive area must be large enough to cover the chest wall of the patient. Due to the diffuse nature of the source, it is also important to maximise the viewing solid angle and avoid the use of window supports, so the gas filling must be at atmospheric pressure. In fact 0.97 atm has been used in order to prevent changes in atmospheric pressure bending the window. The dimensions adopted are a 20 cm square sensitive area, and a maximum absorption depth of 12 cm. For a Xe/5% CO₂ gas mix this provides 99.5% absorption at 13.6 keV, 93.1% at 17.2 keV, and 82.7% at 20.2 keV,

although, as will be seen later, it may be preferable to operate with a smaller absorption depth and correspondingly lower absorption efficiency.

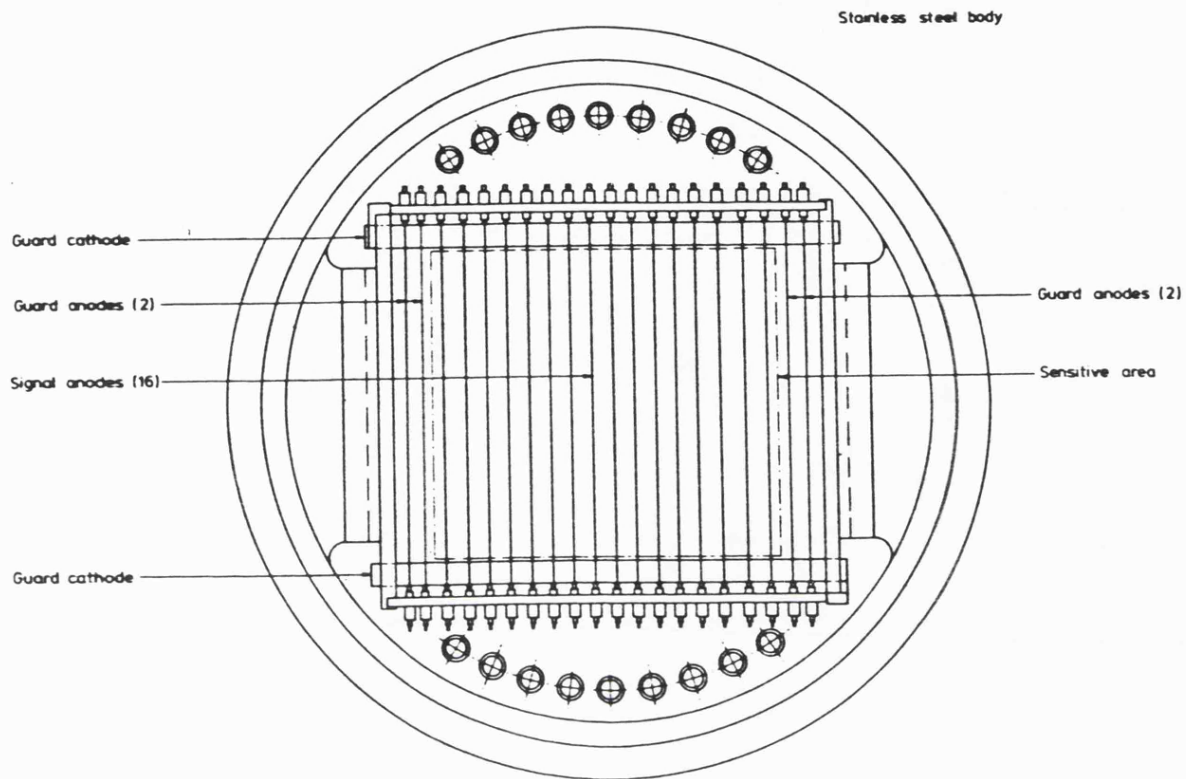


Fig. 6.2 Plan view of the prototype multiwire lung monitor [88].

The design of the electrode grids is similar to that of the EXOSAT x-ray satellite detectors, and were designed using a computer model to calculate the required wire positions. There are seven layers, each being 2 cm deep and containing 18 $20\ \mu\text{m}$ anode wires at a pitch of 1 cm. The edge wires are $30\ \mu\text{m}$ in diameter in order to reduce the intensity of the electric field at the extremities of the grids. Each layer is separated by a cathode plane consisting of earthed $20\ \mu\text{m}$ wires at a pitch of 2.5 mm. In

order to ensure equal gas gain on each anode wire it is important that they are accurately positioned and held in place. This was achieved by the design of the quartz insulator and aluminium alloy ferrule used to secure the wires. The wire positions on a single layer have been measured as having a mean error of $68\text{ }\mu\text{m}$, with a standard deviation of $47\text{ }\mu\text{m}$. [88].

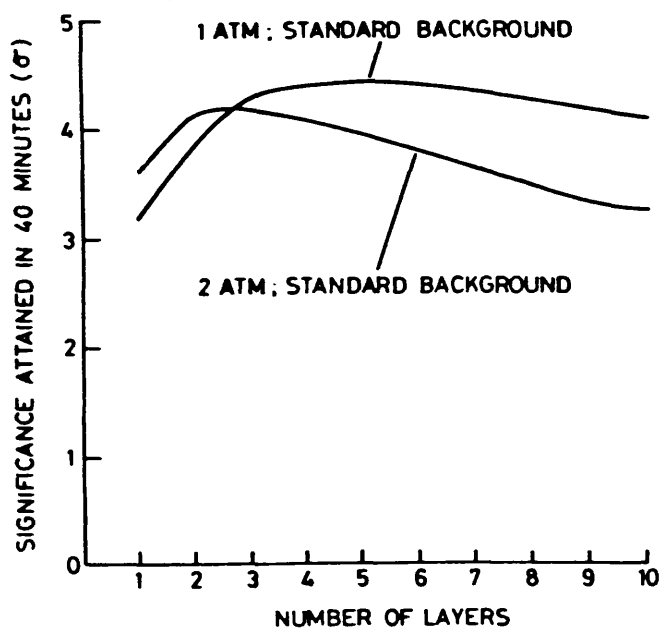


Fig. 6.3 Calculated response curves, showing the standard deviation associated with a 40 minute counting period for a 1 or 2 atm. filling, as a function of the number of 2cm layers used [88].

The number of layers employed in the detector is a compromise, since each layer (except the first) has a similar background level but progressively smaller signal due to the exponential attenuation of the incident x-rays. The original calculations [88] suggested that 5 layers (giving an absorption depth of 10 cm) would be the optimum, but the chamber has been constructed with seven layers in

order to allow this to be checked.

6.2 Background rejection

In order to minimise the number of background events produced within the chamber it is necessary to minimise the amount of material present within, or in contact with, the active volume. To this end, the guard cells around the active volume are not defined by solid walls (so-called mass-less guards), and electrostatic separation of the volume is achieved horizontally by the cathode wires and vertically by suitable connection of the anode wires. This minimises the cross-section for X-ray interactions, and in fact leaves the xenon gas itself as the dominant source of internally generated background events.

In order to reject the residual background that is unavoidable in such a detector, each anode layer can be operated in anticoincidence with all other layers, the rear layer being used as a rear guard cell. The efficiencies of various methods of rise-time discrimination have also been assessed, a technique which is aided by the small dependence of the electron collection time on the position of the x-ray interaction associated with the detector geometry. A front guard is provided by a layer of cathode wires (to which a voltage can be applied) 2 mm below the front window. Most of the electrons produced "above" the guard will be the result of γ -ray interactions with the window material. A

negative bias will repel electrons from this region; a positive bias will collect them. Either effect will stop these false signals being detected on signal layer 1.

In addition to this, full six-sided anticoincidence is provided by side and end guard cells and the use of the rear anode layer as a rear guard cell. The side cell consists of the two outermost wires at each side of each anode grid, which thus form a guard cell 2 cm wide. End guards are provided by strip cathodes, as used on EXOSAT [105,106] the width of which is dependent on the associated processing electronics. The purpose of these guard cells is to reject events resulting from the absorption of Compton electrons emitted by γ -ray interactions with the walls of the chamber. They do this on an unselective basis by rejecting all events detected on the extremities of the anode arrays.

6.3 Processing electronics

The processing electronics used on each layer of the counter are shown in a simplified flow diagram by Fig. 6.4.

Canberra 2002A preamplifiers are used by virtue of being the lowest noise amplifiers available. The PET microcomputer can be programmed to configure the coincidence units to accept anticoincidence pulses from the required locations, defines the time over which these signals will be accepted and displays the counts accumulated. It also

controls the duration of measurements.

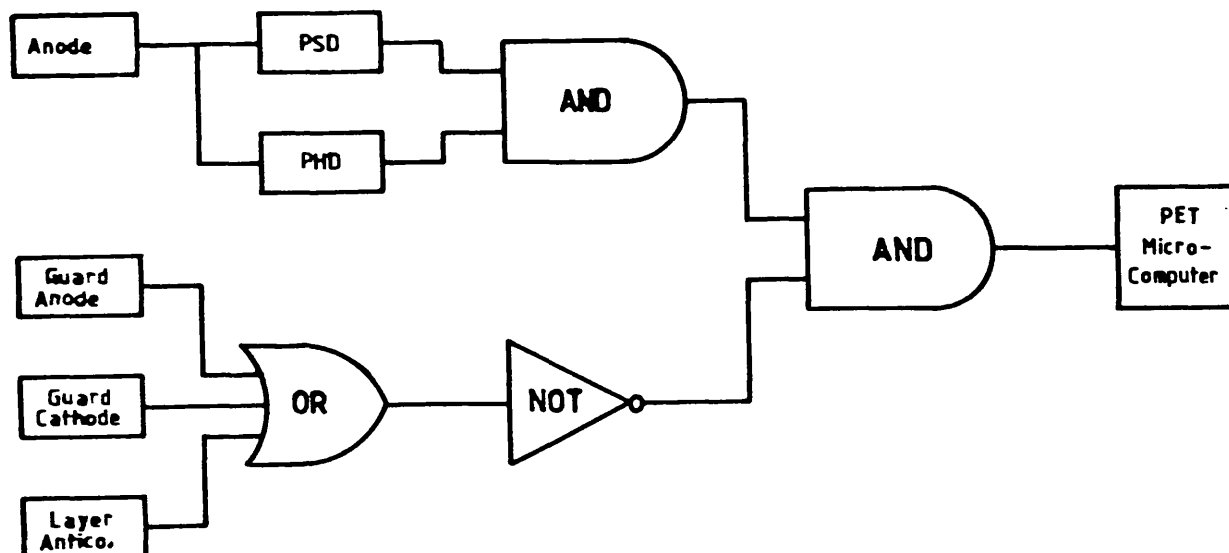


Fig. 6.4 Schematic diagram of the electronics associated with a single layer. The required timing delays are provided by the units.

Full details of the operation of each of the discrimination systems are given in Chapter 7.

6.4 Performance figures

The number of background and signal events rejected by the discrimination systems is, of course, dependent on the settings of the processing electronics. All these settings must be optimised in order to determine the true performance of the counter, and to do this some form of performance figure is required to monitor the relative performance of the detector as a function of these variable settings.

For a variety of reasons it is not convenient to employ a single figure of merit such as the "discrimination factor" defined by Gatti et al [107] and others [108]. For the application envisaged for the detector it is convenient to base this on the relative standard deviation associated with a measurement, of duration t , of a signal providing count rate S_1 , against a background rate B_1 ,

$$\sigma = \left[\frac{1 + aB_1/S_1}{S_1 t} \right]^{1/2} \quad \text{Eqn. 6.1}$$

where the constant, a , is determined by the precision with which the background count rate can be determined. If B_1 is determined from a measurement of the same duration, t , then $a=2$, and as the background measurement time is increased a tends toward unity. However, for lung monitor applications, considerations other than statistics have to be accounted for (such as variability in background due to the subject's build and radioisotope content) which increases the uncertainty of the background count rate. Previous workers [88,109] have adopted an empirical value of $a = 2.38$.

Now, the application of any form of discrimination to the system will change the acceptance ratio of the detector for both source and background events. Defining R_s as the ratio of the source count rates after applying discrimination to that achieved beforehand, and R_b as this

ratio for the background rate, then

$$S_2 = R_S S_1$$

and

Eqn. 6.2

$$B_2 = R_B B_1$$

where S_2 and B_2 are the measured count rates after applying the electronic discrimination. The variances on the new measurements are thus given by

$$(\sigma_1)^2 = \frac{1}{S_1 t} \left[1 + \frac{a B_1}{S_1} \right] \quad \text{Eqn. 6.3}$$

and

$$(\sigma_2)^2 = \frac{1}{S_1 t} \left[\frac{1}{R_S} + \frac{a R_B}{R_S} \frac{B_1}{S_1} \right] \quad \text{Eqn. 6.4}$$

From this it may be shown that the ratio of variances

$$\left[\frac{\sigma_2}{\sigma_1} \right]^2 = \frac{1 + (R_B/R_S) a B_1/S_1}{R_S (1 + a B_1/S_1)} \quad \text{Eqn. 6.5}$$

Any efficacious discrimination system must reduce this ratio below unity, and preferably make it as small as possible. It is important to note that this ratio is a function of three variables: (R_B/R_S) , R_S , and (B_1/S_1) , with the first two of these being determined by adjustment of the

discrimination settings and the third being dependent on external conditions. The value of (B_1/S_1) adopted throughout this work is 1000, since this corresponds to the the values obtained for the background detected from a patient and the signal that would be detected from the LL phantom if the lungs contained activity equal to the ALI of ^{239}Pu (500 Bq). This effectively reduces the figure of merit to

$$\left[\frac{\sigma_2}{\sigma_1} \right]^2 = \frac{R_B}{R_S^2} \quad \text{Eqn. 6.6}$$

The behaviour of this performance figure, F , is shown in Fig. 6.5 where contours of equal F are plotted as a function of R_B and R_S . Any point to the left of the $F = 1$ line indicates worsened performance.

Since the discrimination systems are not totally independent of each other (i.e. some background events will be rejected by more than one system), the counter should ideally be optimised by a process of iteration while employing all discrimination systems simultaneously. However, this process would be prohibitively time-consuming due to the duration of measurements required to obtain statistically significant background measurements at high discrimination levels. This is particularly true in a screened environment where the background can not be adequately simulated by use of γ -ray sources. Instead,

each system was optimised individually, and those that do interact were investigated with the more efficient system pre-optimised. Thus, for example, the guard cathodes were optimised with layer anticoincidence already in use, and rise-time discrimination with all other systems.

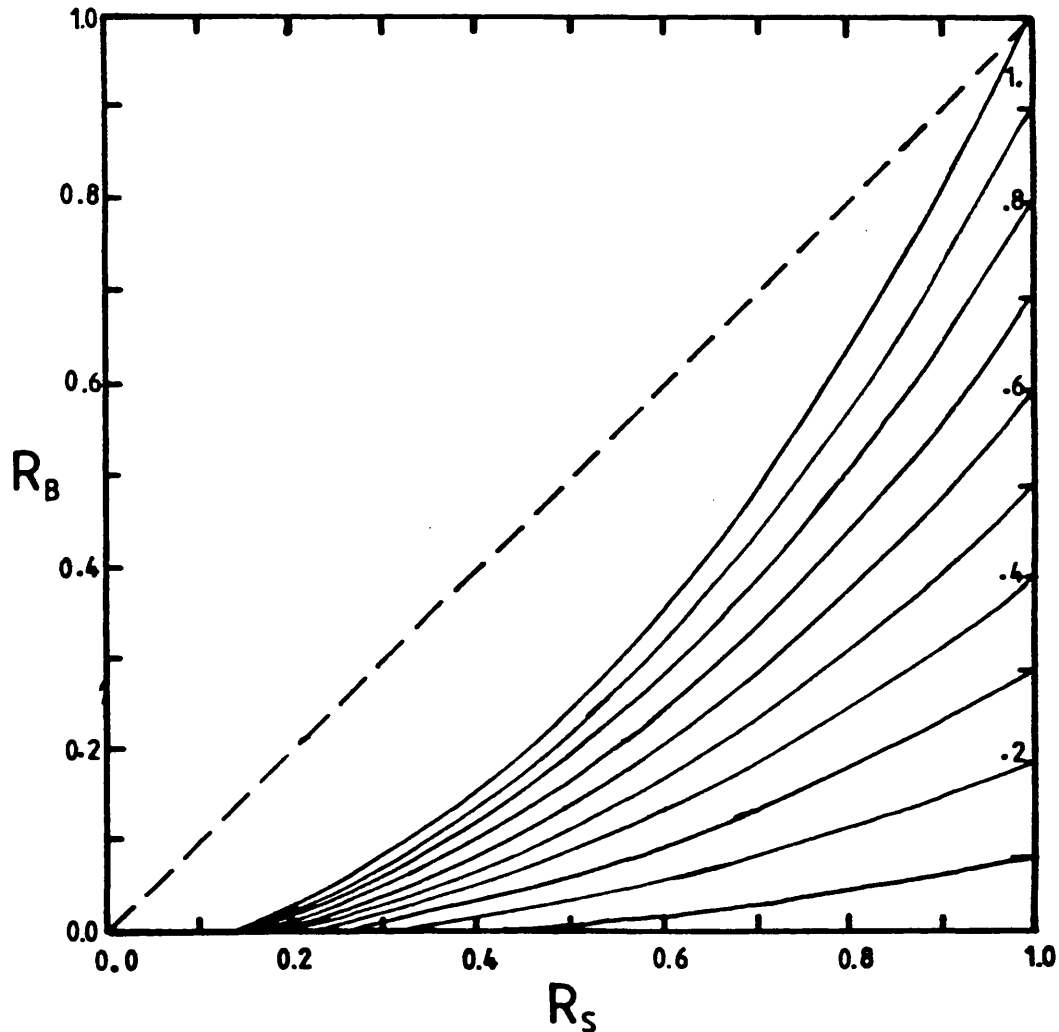


Fig. 6.5 Contours of equal F plotted as a function of R_S and R_B . The broken line corresponds to $R_S = R_B$.

In the following chapter then, the objective is to minimise R_B while keeping R_S as close to unity as possible. F provides a quantitative measure of the level of success in achieving this.

Chapter 7

Evaluation of the Prototype Lung Monitor

7.1.1 Proportionality

For an operating voltage of 1.72 kV, the energy proportionality of the six possible signal anode layers have been measured for the range 12 - 45 keV. The results are shown in Fig. 7.1 which clearly demonstrates that the detector response is linear throughout the region of interest.

7.1.2 Gain

The gas gain of the detector, has been calculated as being of the order 3.4×10^3 . The consistency of the gain has been measured using a collimated Ag K source (22keV) as a function of position across the two central axes of the detector, ie parallel to (defined as the x-axis), and perpendicular to (defined as the y-axis), the anode wires, for each of the six anodes. The results are displayed in Figs. 7.2 and 7.3, and in Table 7.1. The gain generally rises towards the extremities of the anode grids, but otherwise shows a good degree of uniformity. The 10th wire in the first layer evidently has some form of blemish that

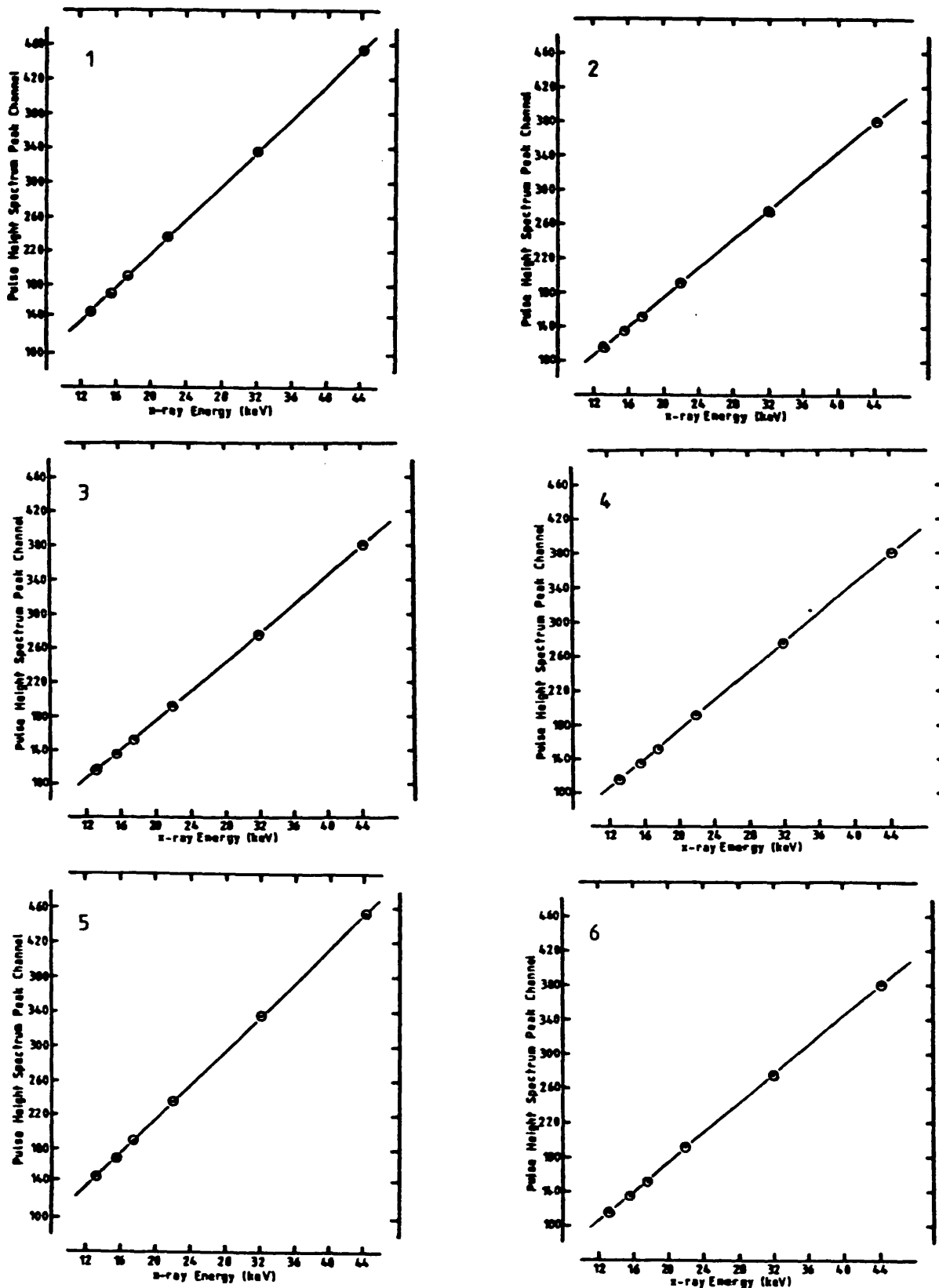


Fig. 7.1 Energy proportionality of the six possible signal layers of the detector. They are numbered 1-6 from the anode nearest the chamber window.

results in a suppression of the gain for a region about 2 cm in extent. This had not been noted previously [88], but is the only evidence for a deterioration in the condition of the wire grids. However, this effect is apparently carried through to the second layer to a certain extent.

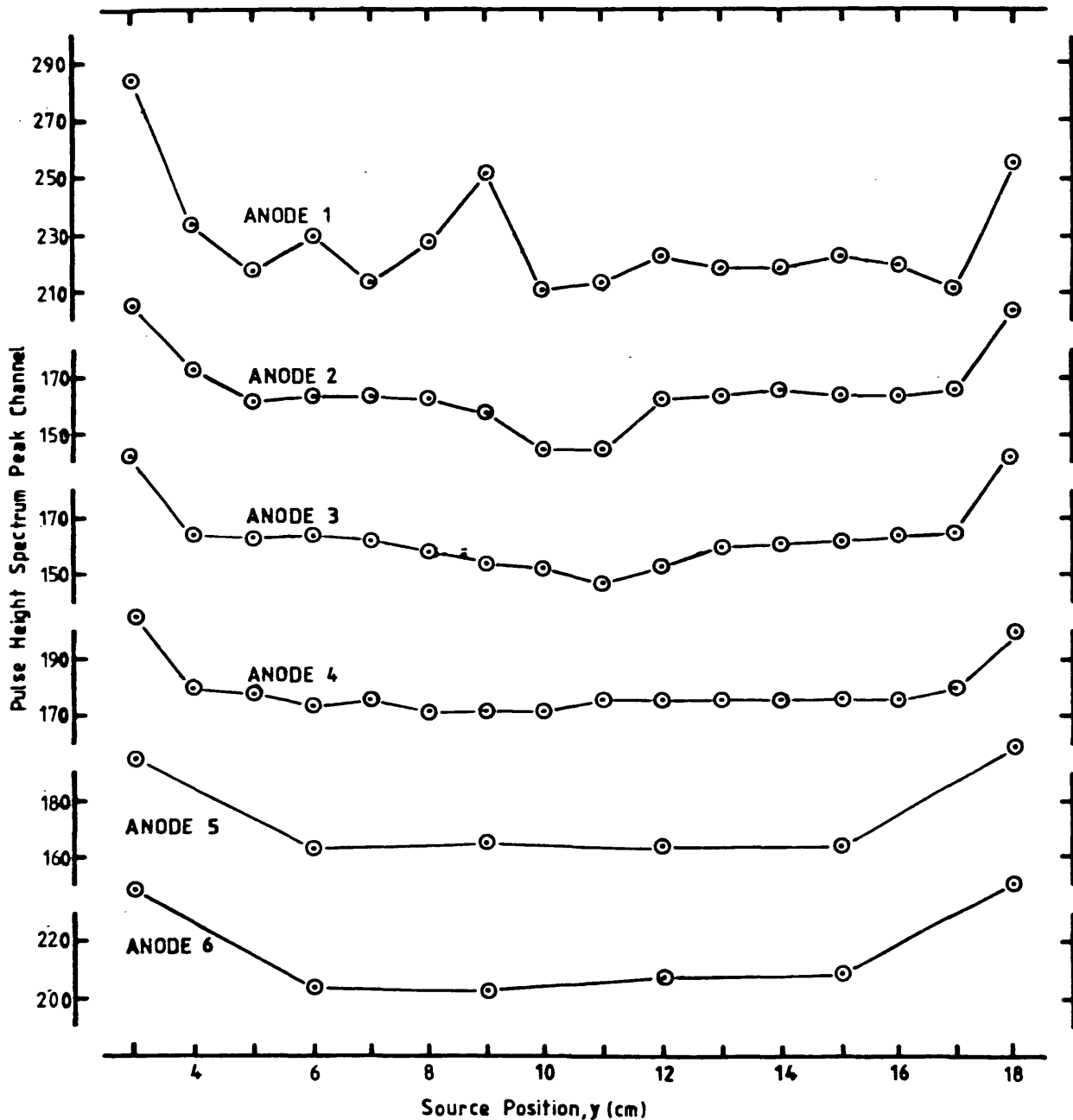


Fig. 7.2 Measured gain of each signal layer as a function of position perpendicular to the anode wires ($x=10$).

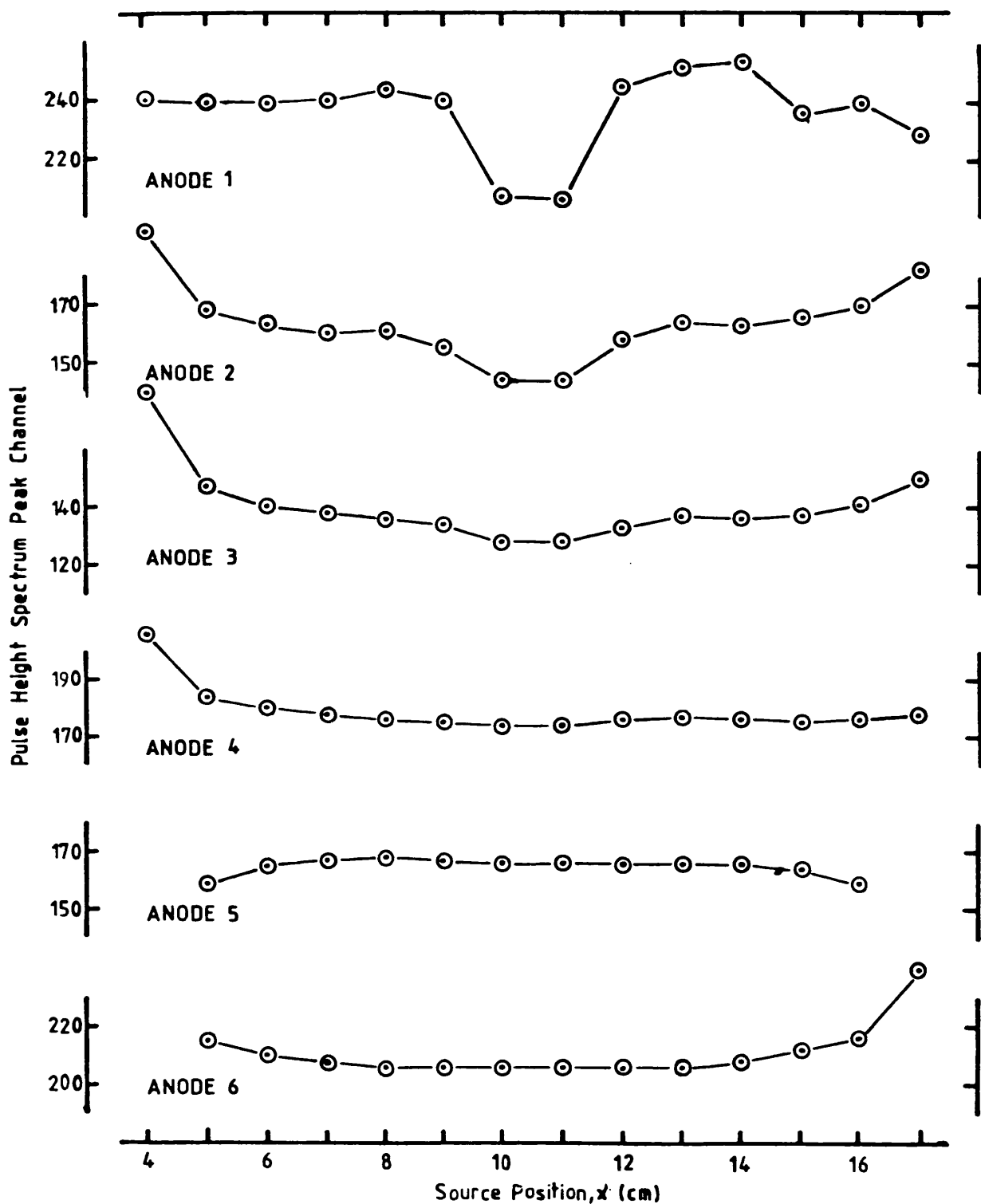


Fig. 7.3 Measured gain of each signal layer as a function of position parallel to the anode wires ($y=10$).

The lower layers do not show any significant variation in gain, apart from near the guard cells. Real variations would be less evident on these layers due to the divergence of the x-ray beam as it passes through the detector, but would be reflected in a deterioration in energy resolution.

Anode	Maximum pulse height	Minimum pulse height	Variation (%)
1	254	206	19
2	173	144	17
3	167	147	12
4	184	172	6.5
5	168	159	5.4
6	215	203	5.6

Table 7.1 Variation in gain on each anode. The peripheral regions affected by the guard cells are not included.

7.1.3 Resolution

The energy resolution has been measured in a similar way to the gain, using the same 22 keV source. The results are displayed in Table 7.2 and in Figs. 7.4.

The resolution is poor in the damaged section of signal anode one, and in the corresponding section of anode 2, but elsewhere is good, and consistent, over each anode grid. Since the resolution is good on the lower anodes there can be no significant variations in gain that are masked by the divergence of the x-ray beam.

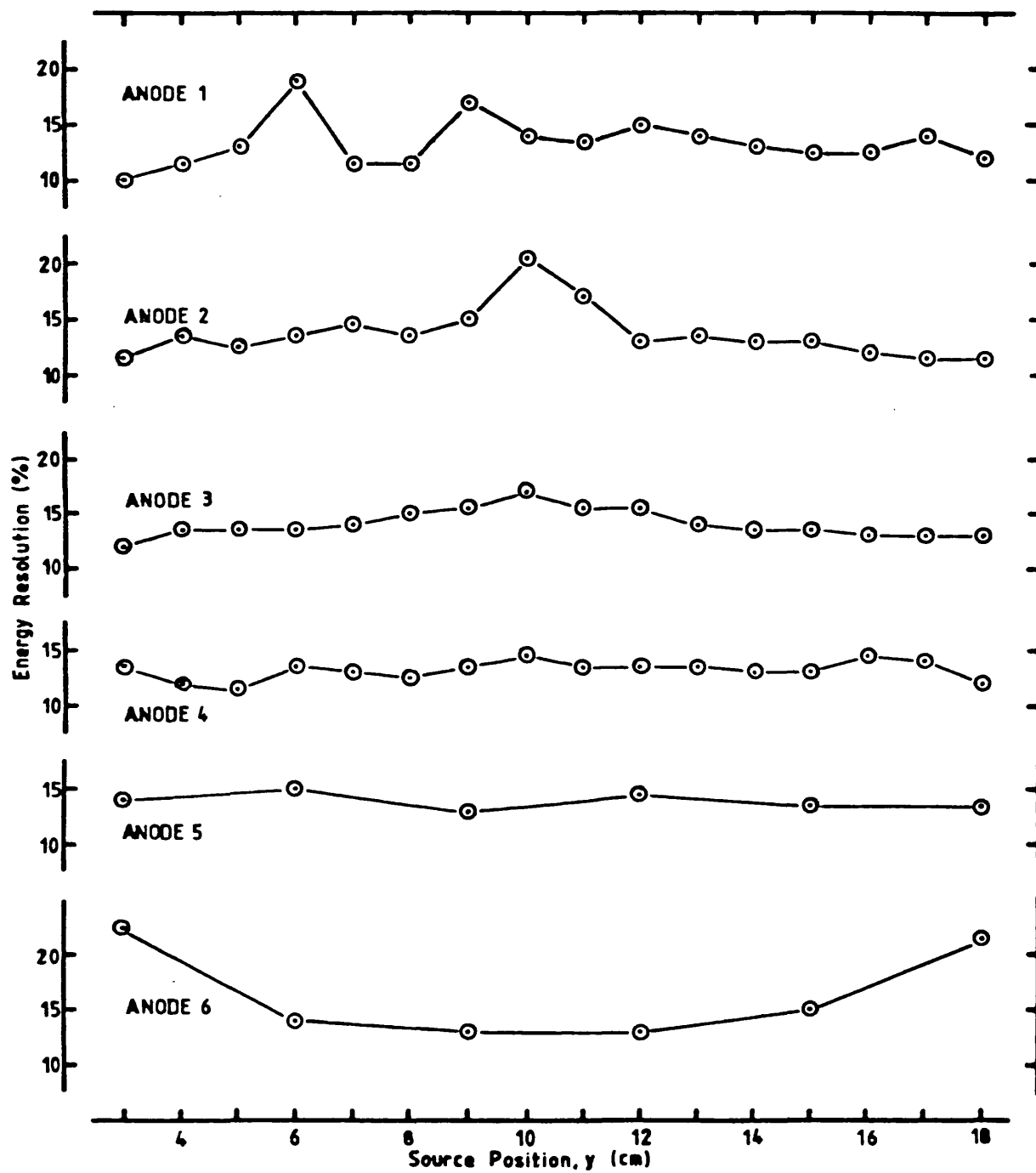


Fig. 7.4a Resolution of each layer measured as a function of source position perpendicular to the anode wires ($x=10$).

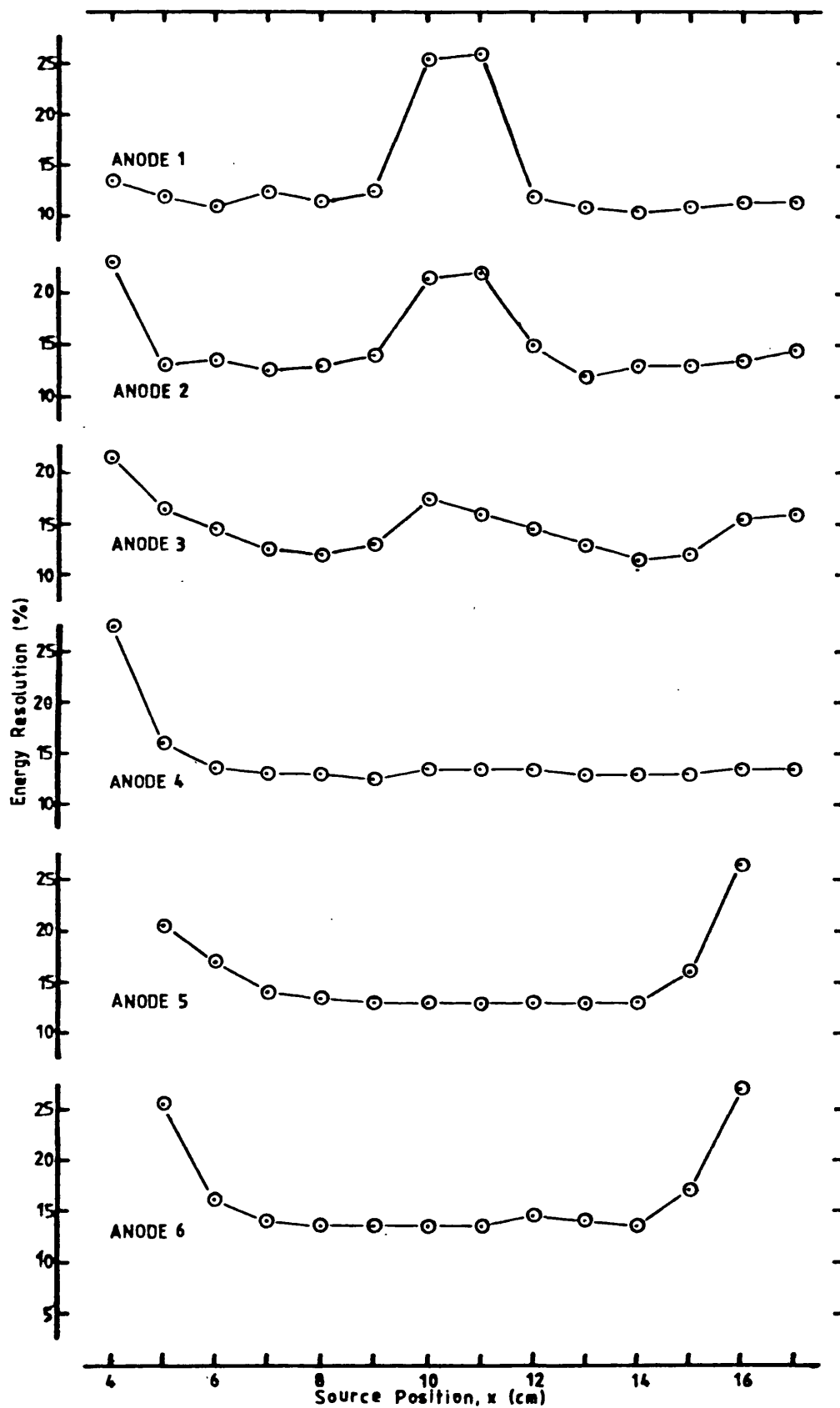


Fig. 7.4b Resolution of each Layer measured as a function of source position parallel to the anode wires ($y=10$).

Anode	Maximum resolution (%)	Minimum resolution (%)	Variation (%)
1	10.1	26.2	16.1
2	11.3	23.1	11.8
3	11.4	17.6	6.2
4	11.7	14.5	2.8
5	12.8	14.8	2.0
6	12.8	15.2	2.4

Table 7.2 Variation in resolution on each anode. The peripheral regions affected by the guard cells are not included.

7.1.4 Window transmission

The original 2mm carbon fibre window allowed only 75% transmission of 15.8 keV x-rays, which results in an unacceptably low detection efficiency for uranium L x-rays. This has been replaced by one of 0.5 mm thickness, allowing 91% transmission at this energy. Obviously it would be helpful to improve the transmission still further, but the window must be rigid enough not to bow with varying atmospheric pressure, and resilient enough to withstand the wear and tear involved with use as a lung monitor.

7.2 Background rejection

Each of the background rejection systems have been assessed by calculating the performance figure derived in Chapter 6 as a function of the relevant settings. This has been done both in a normal laboratory and in the screened room at the Body Radioactivity Measurement Section at Harwell, the normal working environment for the lung monitors in use at that establishment at present. The walls of this room are lined with 4" of lead, coated with cadmium. This alters the nature as well as the quantity of background radiation, and thus influences the performance of the detector.

7.2.1 Layer anticoincidence

This is the single most effective discrimination system due to the high efficiency at eliminating background events and small loss of signal. This is not surprising since true x-ray events can only produce signals on adjacent layers if the original photoelectron crosses between layers. In fact, these events would be rejected by pulse height discrimination since the detected charge will be split between the layers. The only loss of signal will thus arise when a signal event happens to occur at the same time (or rather within the coincidence time defined by the processing electronics) as either another signal event, or a background event, on a layer providing anticoincidence

pulses. The number of these "accidental" rejections, n_a , is given by

$$n_a = t n_1 n_2 \quad \text{Eqn. 7.1}$$

where t is the coincidence time, n_1 is the signal count rate, and n_2 is the total count rate on the anticoincidence layer. τ is defined in the computer program as 9 μ s, while n_1 will be $\sim 10^{-3} \text{ s}^{-1}$ (for a measurement of a contaminated patient, obviously much larger when using a source to assess and optimise the detector), and $n_2 \sim 1 \text{ s}^{-1}$, making $n_a \sim 10^{-8} \text{ s}^{-1}$, or $\sim 0.001\%$ of the signal count rate. This is one positive feature of the very low count rates involved in this application.

Since the long track background events rejected by this system can not produce signals on two non-neighbouring anodes and miss the one between, using only neighbouring anodes for anticoincidence signals minimises the false rejection of signal without being detrimental to the background rejection. This assumption is born out in the results detailed in Table 7.3.

The electronics associated with anticoincidence between layers are shown in Fig. 7.5. The settings of the discriminator thresholds are not critical, and need only be set above the noise level.

Anode	Antico layer x-1			Antico layer x+1			Antico with both		
	R_S	R_B	F	R_S	R_B	F	R_S	R_B	F
1	—	—	—	0.967	0.131	0.140	0.967	0.131	0.140
2	0.960	0.126	0.137	0.971	0.120	0.127	0.945	0.0451	0.051
3	0.978	0.132	0.138	0.979	0.136	0.142	0.964	0.0495	0.053
4	0.923	0.261	0.306	0.916	0.144	0.171	0.882	0.0686	0.088
5	0.974	0.131	0.138	0.981	0.143	0.149	0.969	0.0447	0.048

Table 7.3 Signal and background efficiencies, and the associated figure of merit, for layer anticoincidence. The signal efficiencies are for uniform irradiation by a plutonium source, and the background efficiencies are for that detected in the screened room.

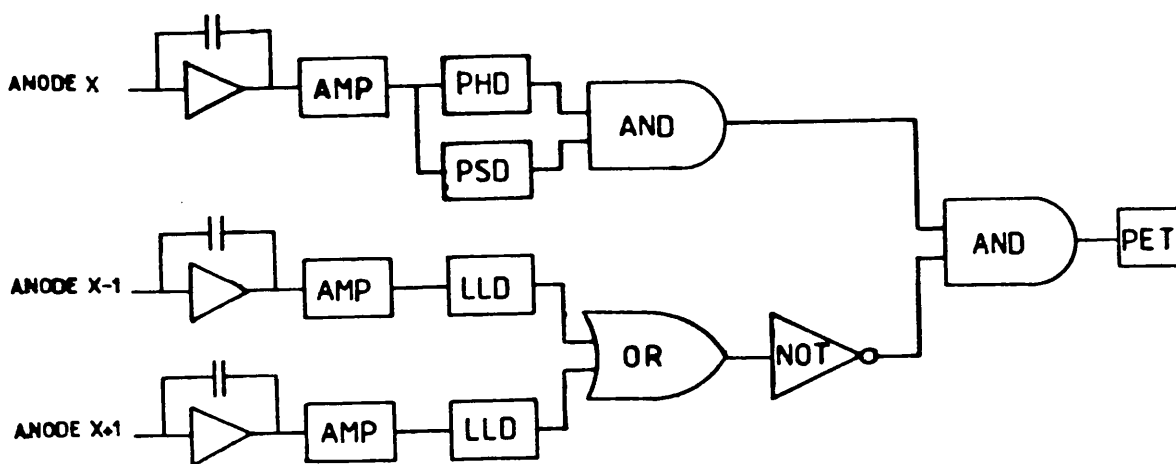


Fig. 7.5 Schematic diagram of the electronics for anticoincidence between layers. Required timing delays are provided by the units.

7.2.2 Guard anodes

Anode	R_S	R_B	F
1	0.993	0.833	0.845
2	0.988	0.661	0.677
3	0.963	0.656	0.707
4	0.991	0.664	0.676
5	0.991	0.690	0.703

Table 7.4 Signal and background efficiencies, and the associated figure of merit, for the guard anodes. The signal efficiencies are for uniform irradiation by a plutonium source, and the background efficiencies for that detected in the screened room.

The guard anodes for each side of each layer are connected together internally and taken out through two feed-throughs to one preamplifier. Any resulting signal above the noise level is then used as an anticoincidence pulse for all the signal layers. This results in the rejection of all signals occurring at the edge of the electrodes, on the principle that the majority will be due to γ -ray interactions with the walls of the detector chamber. This reduces the width of the sensitive area to 16 cm. The performance of the guard anodes is not sensitively dependent on the setting of the threshold discriminator, and they also have the advantage of being largely independent of the other systems.

7.2.3 Guard cathodes

The end guards consist of strip cathodes which provide anticoincidence pulses when events occur near the end of the anode wires. For these guards the width of the guard cell is controlled by the configuration in which they are operated and by the processing electronics. Obviously as the width of the cell is increased, the residual background detected on a layer will be reduced, along with the signal count rate. If the guard cathodes are investigated in isolation, this gives a large optimum cell width, but many of these background events will be eliminated by anticoincidence between layers of the detector. When assessing the performance of the guard cathodes it is thus important that they be operated in conjunction with layer anticoincidence, as is born out by the results below.

The same assumption (that the majority of these peripheral events will be background) as is made for the guard anodes applies. However, instead of all the guard cathodes being connected together, as with the anodes, only the four strips associated with each signal anode are connected, thus providing separate outputs for each layer.

The guard cathodes can be used in three different configurations. The simplest approach is to use the guard cathode signals to trigger the anticoincidence pulse directly, in the same way as is used for the guard anodes (see Fig. 7.6).

The results obtained are shown in Table 7.5. Direct comparison with those quoted above for layer anticoincidence can not be made due to the different sources used for both signal and background.

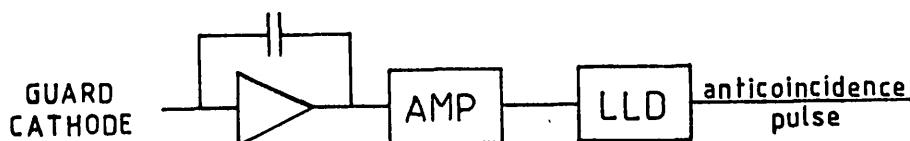


Fig. 7.6 Simplest guard cathode configuration. An anticoincidence pulse is produced when the cathode signal crosses a definable threshold.

However, in this configuration, the magnitude of the guard cathode signal is a function not only of the energy of the detected event but also of its position within the detector. If a long track event passing through the detector parallel to the anode wires is to deposit energy within the range accepted by pulse height discrimination, the charge must thinly spread over this length with only a small amount near the edge of the detector, and so only a small signal will result on the guard cathode. Since this is the very event the guard is supposed to reject, the threshold must obviously be set low enough to trigger the anticoincidence pulse for such an event. However, a genuine x-ray event occurring deep within the active area of the detector can also induce a small signal on the guard cathode, and thus reject itself.

In order to overcome this, the guard cathodes can be made position, rather than charge, sensitive. A simple way

to do this, involving summing the anode and guard cathode signals was employed on the EXOSAT detectors, but was not investigated in detail on the lung monitor.

A more complicated, and more effective method, is to determine the ratio of the cathode to anode signals electronically. This ratio is a function of position only, not of energy, and can be used to provide the input of the lower level discriminator. This system is capable of sharply defining the width of the guard cell (Fig. 7.7).

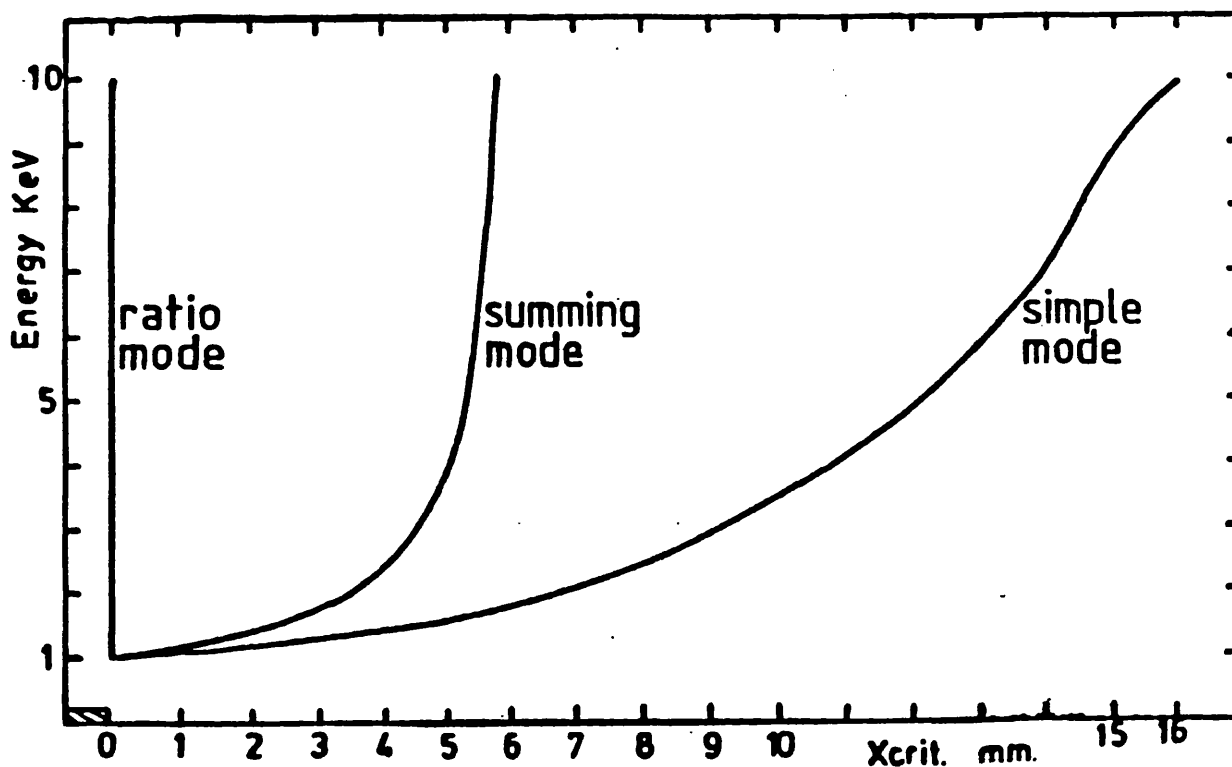


Fig. 7.7 Extension of the guard cathode cell width with event energy for the three methods of signal processing. These results are for the EXOSAT detectors [105].

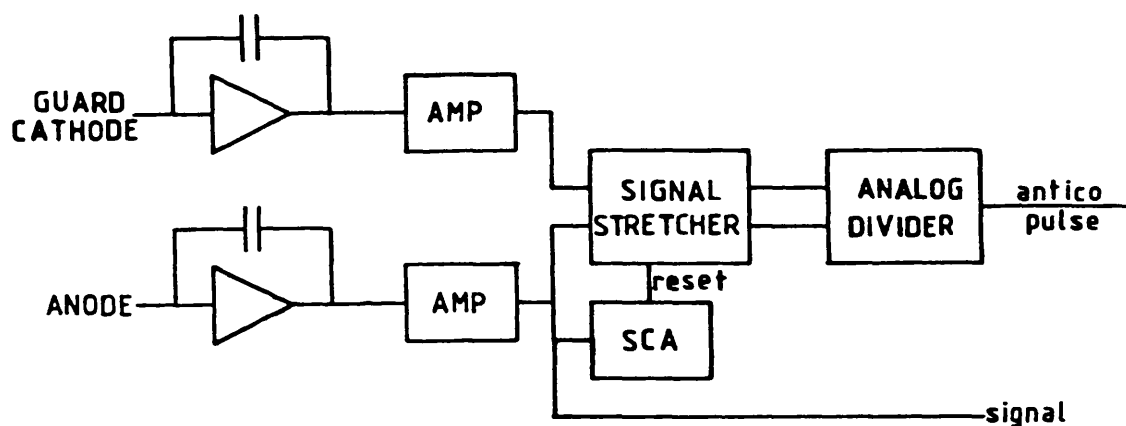


Fig. 7.8 Signal processing arrangement for the "ratio" method.

Anode	Simple mode			Ratio mode		
	R_S	R_B	F	R_S	R_B	F
1	0.943	0.229	0.258	0.917	0.212	0.252
2	0.947	0.0789	0.088	0.898	0.0762	0.094
3	0.951	0.0743	0.082	0.958	0.0945	0.103

Table 7.5 Performance of the guard cathodes in conjunction with layer anticoincidence. These results are for a monochromatic x-ray source and background simulated by Co^{60} .

The ratio method, while improving the spatial definition of the guard cell does not improve the performance of the guard cathode system. This is no doubt partly because the anode gain is greater at the ends of the anode wires because the position of the guard cathodes below the cathode grids increases the field in this region.

Signal events will thus be rejected by the pulse height discrimination in this zone, and so use of the simple configuration has not resulted in loss of signal.

The performance figures are somewhat different for results taken using a plutonium source and for the natural background in the low background room. These results are shown in Table 7.6.

Anode	Simple mode			Ratio mode		
	R_S	R_B	F	R_S	R_B	F
1	0.919	0.233	0.275	0.917	0.243	0.289
2	—	—	—	0.912	0.0442	0.053
3	—	—	—	0.907	0.0379	0.046
4	—	—	—	0.868	0.0403	0.053
5	—	—	—	0.911	0.0247	0.030

Table 7.6 Performance of the guard cathodes in conjunction with layer anticoincidence. These results are for the natural background encountered in the low background room and for a plutonium source.

These figures are directly comparable with those quoted for layer anticoincidence in Table 7.3, and show that the guard cells do make a small but significant contribution to the performance. There is little difference in the performance of the end guard cells in the two configurations

investigated, and neither showed a strong dependence on the settings of the processing electronics. This is in itself an indication that the change in gain at the end of the anode wires results in a loss of signal in this region, and thus reduces the importance of limiting the extent of the end guard cell.

7.2.4 Front guard

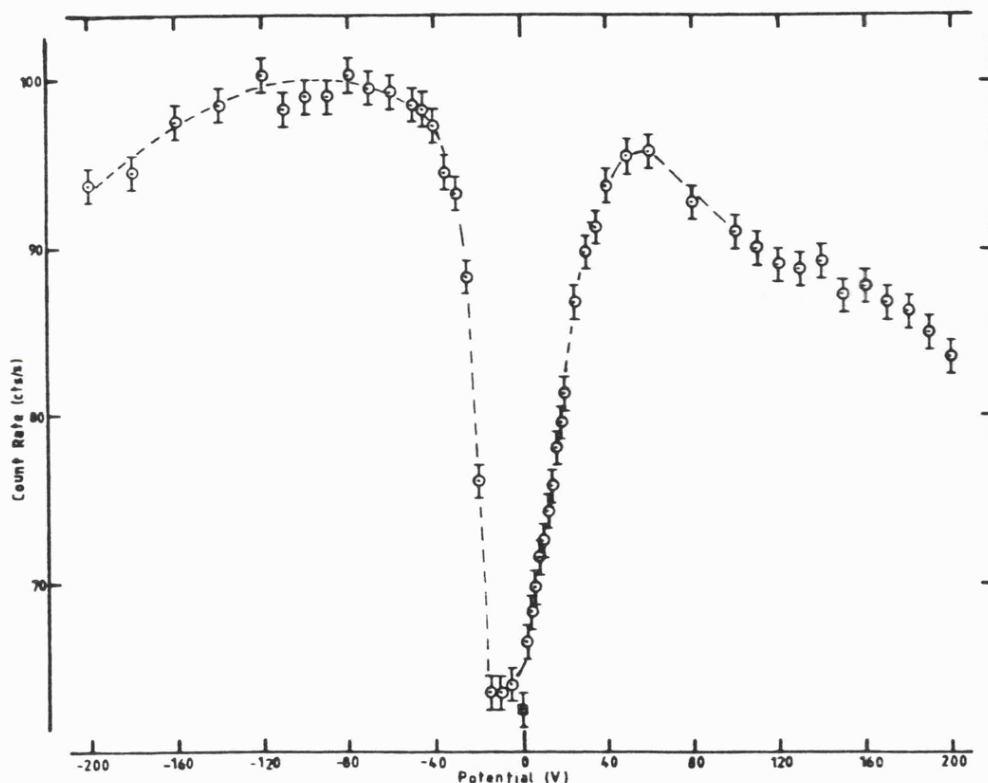


Fig. 7.9 Background count rate detected on signal anode 1 measured as a function of the bias applied to the front guard cathode. The isolated point, marked by a box, is for the guard earthed.

The front guard reduces the number of background events

detected on the front anode (see p.81). The performance of the guard in both respects is dependent on the bias applied to the cathode. Fig. 7.9 shows the background count rate obtained on signal anode 1 as a function of the bias applied to the front guard.

The front guard is clearly most efficient when earthed. This does not indicate that it should not be included, as the absence of an applied potential does not mean that it does not influence the electric field in the chamber.

7.2.5 Pulse shape discrimination

Three pulse shape discrimination systems have been examined on the prototype lung monitor: the Adams/White PSD unit [108], an Ortec 458 pulse shape analyser, and the cross-over discrimination system described in Chapter 3.

The Adams/White PSD unit was designed primarily to distinguish between neutron and γ -ray events in scintillation detectors, and works on the principle of charge comparison. For this application, the photomultiplier anode current is integrated by two separate linear gated integrators for times T_1 and T_2 , with $T_2 > T_1$, and the outputs of these integrators are weighted and compared. If the output of integrator 2 is found to exceed that of integrator 1, a neutron event (ie long duration) is indicated, and if the converse is true a γ -ray (ie short

duration) event is indicated. This is obviously directly applicable to the situation in hand, except, of course, that the required integration times will be different from those needed for a scintillation detector.

Although these units are convenient to use, being relatively easy to optimise and containing all the circuitry required for pulse shape discrimination, pulse height discrimination, and layer anticoincidence, their disappointing performance when applied to the prototype lung monitor has been noted before [88] and is verified by the more definitive figures given in Table 7.7 and in Fig. 7.13.

Anode	Laboratory			Screened room		
	R_S	R_B	F	R_S	R_B	F
1	0.890	0.252	0.318	0.819	0.054	0.081
2	0.784	0.203	0.330	0.785	0.041	0.067
3	0.778	0.174	0.287	0.842	0.080	0.112
4	0.728	0.122	0.230	0.866	0.115	0.153

Table 7.7 Performance for the Adams/White PSD unit using a monochromatic x-ray source and simulated background in the unscreened laboratory and a plutonium source and the natural background in the screened room.

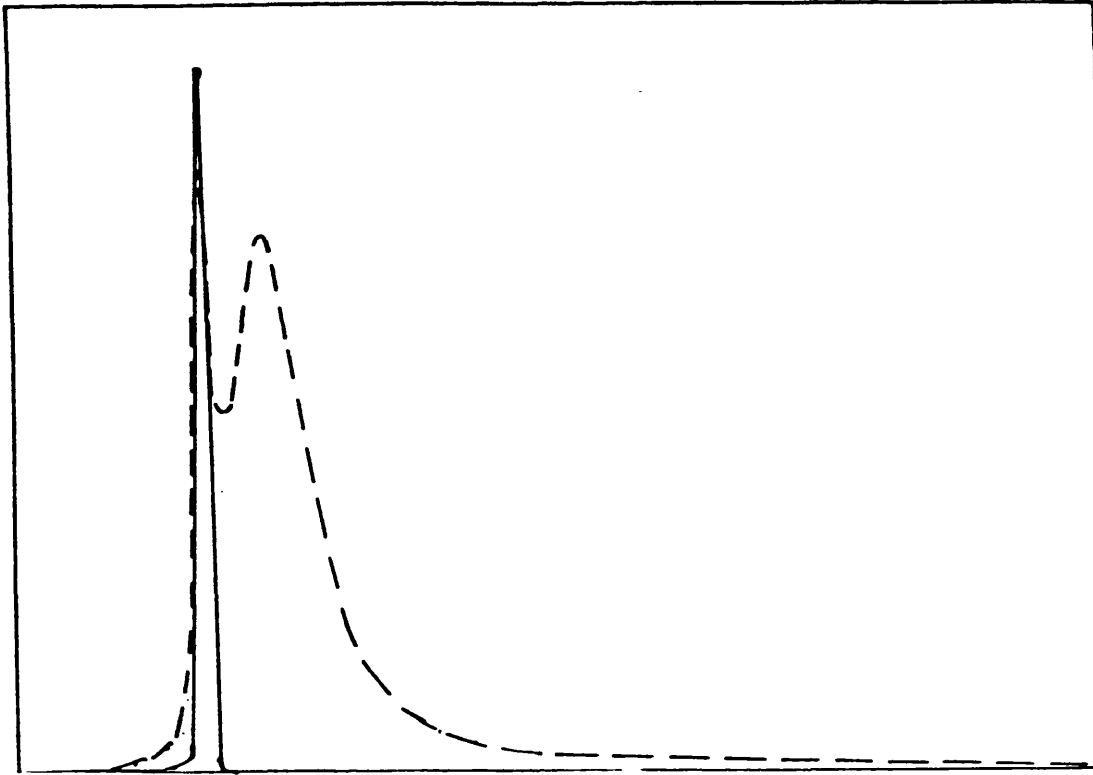


Fig. 7.10 Pulse fall time spectra for x-ray (continuous curve) and for simulated background (broken curve) events.

The Ortec 458 PSA measures the 90%-10% falltime of a bipolar signal, and generates a linear output pulse of amplitude proportional to this time. It also provides an SCA output to produce a logic pulse when the falltime lies within a set range. Obviously the same criterion as to the optimum amplifier shaping time constants applies as for the cross-over discrimination technique, but this unit requires times in the range 0.2 - 10 μ s. Unlike the Adams/White unit, this module does not provide pulse height discrimination itself, so a separate facility must be employed and used in coincidence with the unit's SCA signal. The pulse falltime spectrum obtained from this unit for x-ray and for background (simulated by a Co^{60} source) is shown in Fig. 7.10, and the background and signal acceptance

ratios, together with the performance figure, are shown as a function of discriminator position in Table 7.8.

It must be stressed that these are the results obtained with pulse height discrimination in operation, and vastly inferior results are obtained if it is not used. However, these results do show that this system provides better discrimination than the Adams/White unit for this particular application.

Anode	R_S	R_B	F
1	0.858	0.216	0.293
2	0.917	0.155	0.184

Table 7.8 Data for the Ortec 458 PSA. These results were obtained in the normal laboratory using monochromatic x-rays and induced background.

However, the Ortec unit only makes use of the dependence of the faltime of the shaped pulse on the nature of the ionising event, and calculations by Mathieson [110] show that this is only a slowly varying function of the electron collection time, τ , most of the information being carried in the leading edge of the pulse. The cross-over discrimination technique described in Chapter 3 should thus provide considerably better performance.

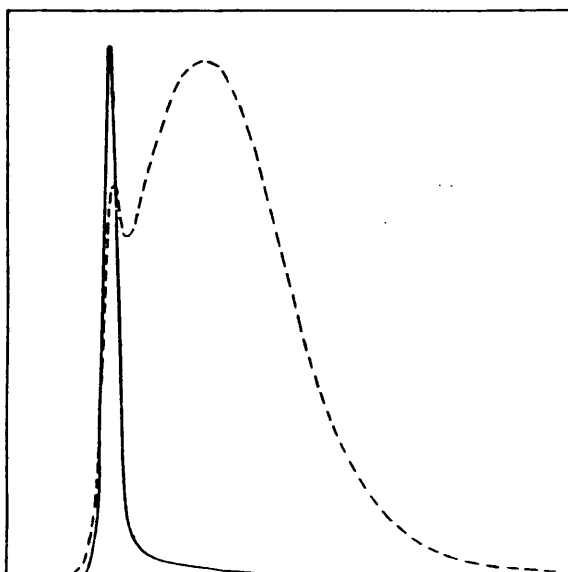


Fig. 7.11 Cross-over spectra for x-ray (continuous curve) and for simulated background (broken curve) events.

Anode	R_S	R_B	F
1	0.830	0.0929	0.134
2	0.803	0.0907	0.141
3	0.795	0.0724	0.114
4	0.836	0.175	0.250
5	0.792	0.0677	0.108

Table 7.9 Data for the cross-over discrimination system, taken in the normal laboratory using monochromatic x-rays and simulated background.

This is shown in Table 7.9 and in Fig. 7.11 which shows the superior definition between the x-ray and background cross-over peaks compared to the pulse falltime spectra.

It is also noticeable, however, that the definition between cross-over peaks is not as good as achieved on the coaxial counter. This is because the uniform field in the multiwire chamber reduces the dependence of the cross-over time on the extent of the initial charge track. However, in the screened room improved definition is obtained due to the reduction in the number of short cross-over background events (see Fig. 7.12).

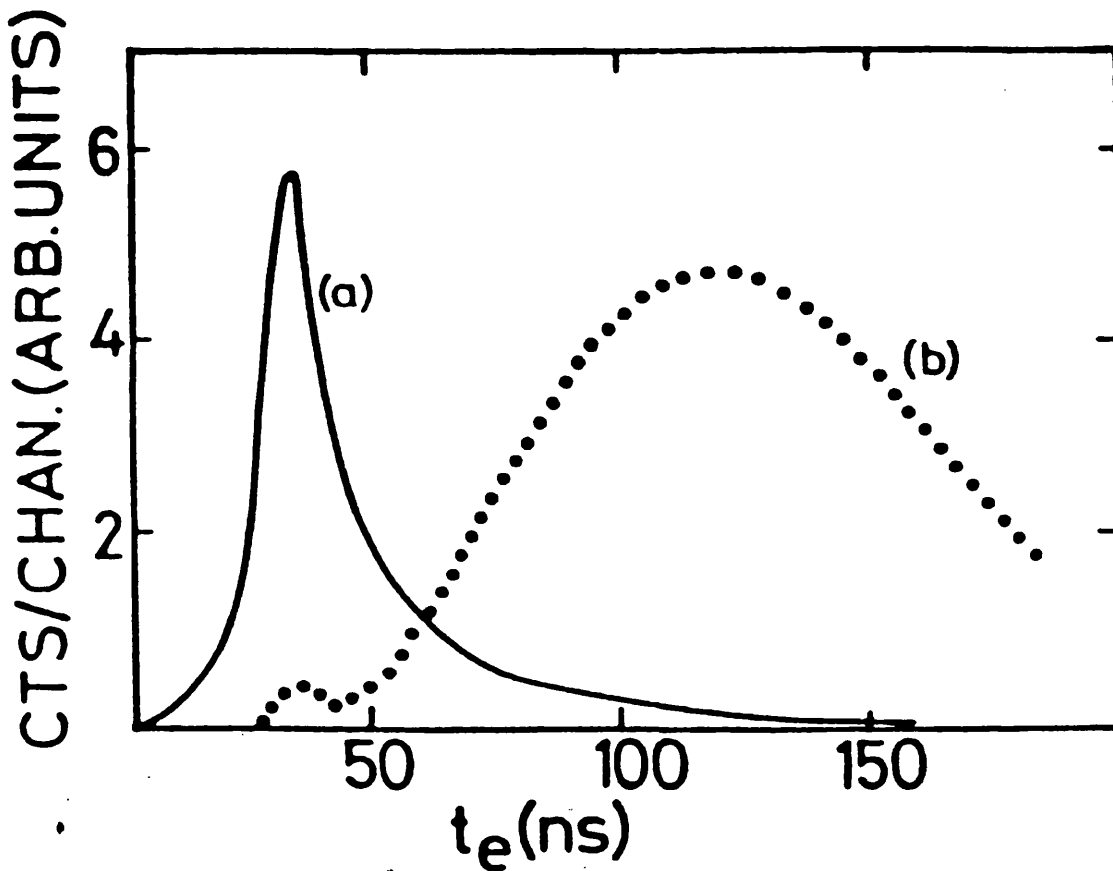


Fig. 7.12 Crossover spectra (a) for Pu source and (b) for natural background radiation measured in the screened room. The x-ray peak is spread because of the spread in t_e due to the range in pulse heights for a plutonium source.

Fig. 7.13 shows the performance of each of the systems

as a function of the signal acceptance ratio.

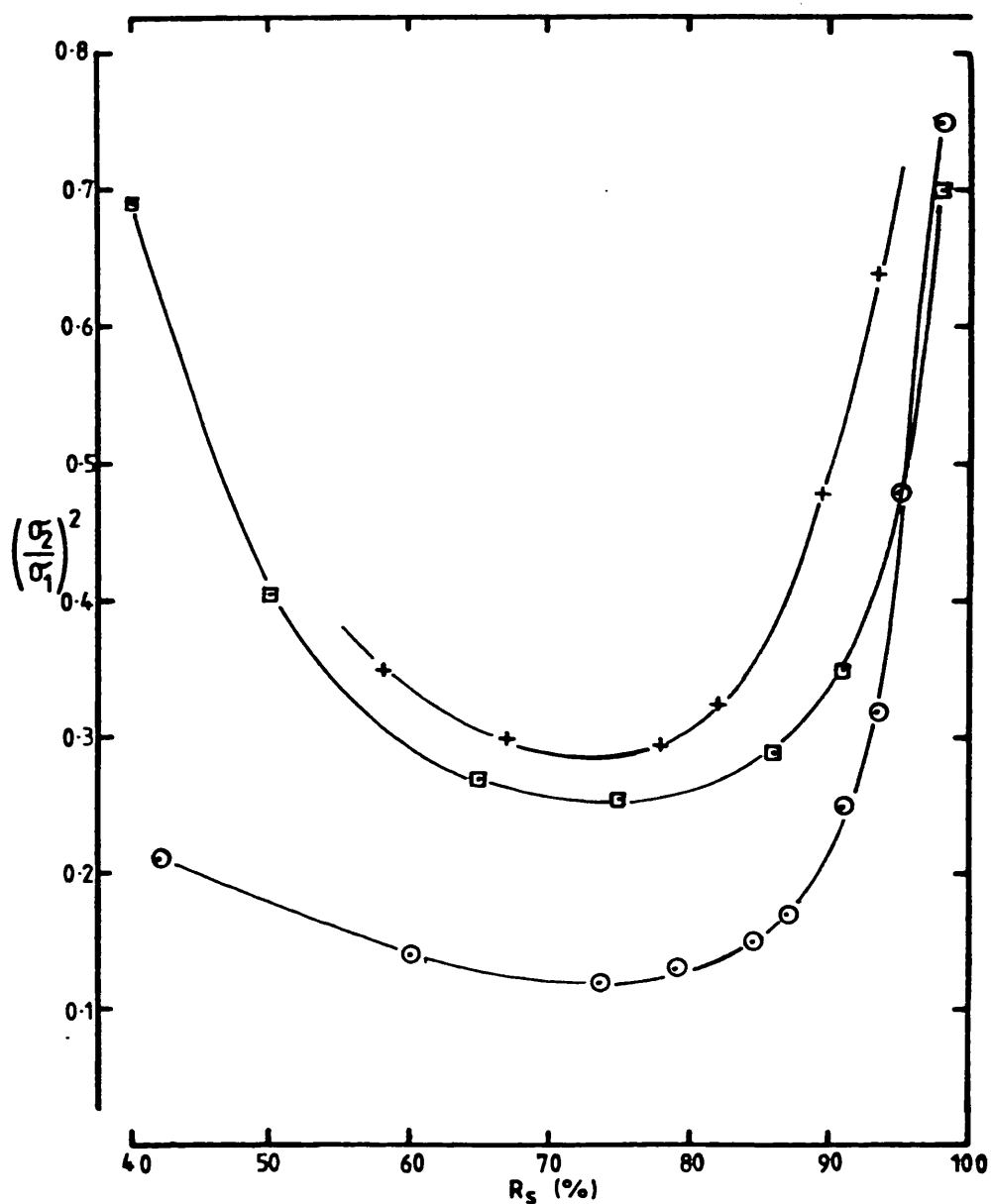


Fig. 7.13 The figure of merit, measured as a function of R_s , for the three methods of pulse shape discrimination investigated on signal anode 1. Circled data points are for the cross-over discrimination system, those marked with a box are for the Ortec 458 PSA unit, and those marked with a cross for the Adams/White PSD unit. These results are for a monochromatic source and induced background.

7.3 Overall performance

The performance of each layer of the detector, measured as a function of the discrimination systems applied in the screened room, is given in Table 7.10. It is clear that the optimum configuration of systems is as suggested by the above results, and that all systems do make a positive contribution to the overall detector performance.

Anode	GA	Antico	Both+GC	PSD	Total		
					R_S	R_B	F
1	0.746	0.140	0.0762	0.139	0.781	0.0166	0.0272
2	0.677	0.0505	0.0412	0.311	0.806	0.0129	0.0199
3	0.707	0.0533	0.0419	0.180	0.850	0.0120	0.0166
4	0.676	0.0882	0.0488	0.960	0.830	0.0130	0.0189
5	0.703	0.0476	0.0269	0.912	0.872	0.0175	0.0230

Table 7.10. Combined system performance for measurement of plutonium x-rays and the natural background radiation encountered in the screened room.

The figures in the above table represent the optimum operating condition, and not the optimum performance of each individual system. The figures for crossover discrimination are thus very different on signal anodes 4 and 5 than on the others because it was found to be profitable to operate the system at relatively high values of R_S and R_B due to the efficiency of the other systems.

Operating in this optimum configuration, measurements of the LL phantom and of the natural background and potassium and caesium phantoms were taken in the screened room as a function of the width of the acceptance energy window. It was found that the severe attenuation of the $U L_{\alpha}$ x-rays by the chest wall of the phantom (or patient) make it advantageous to limit the window to covering the L_{β} and L_{γ} x-rays only, even on the front signal anode, where, due to the high x-ray cross-section of xenon at 13.6 keV, the bulk of the L_{α} x-rays are detected. (See Fig.7.15 and Table 7.11).

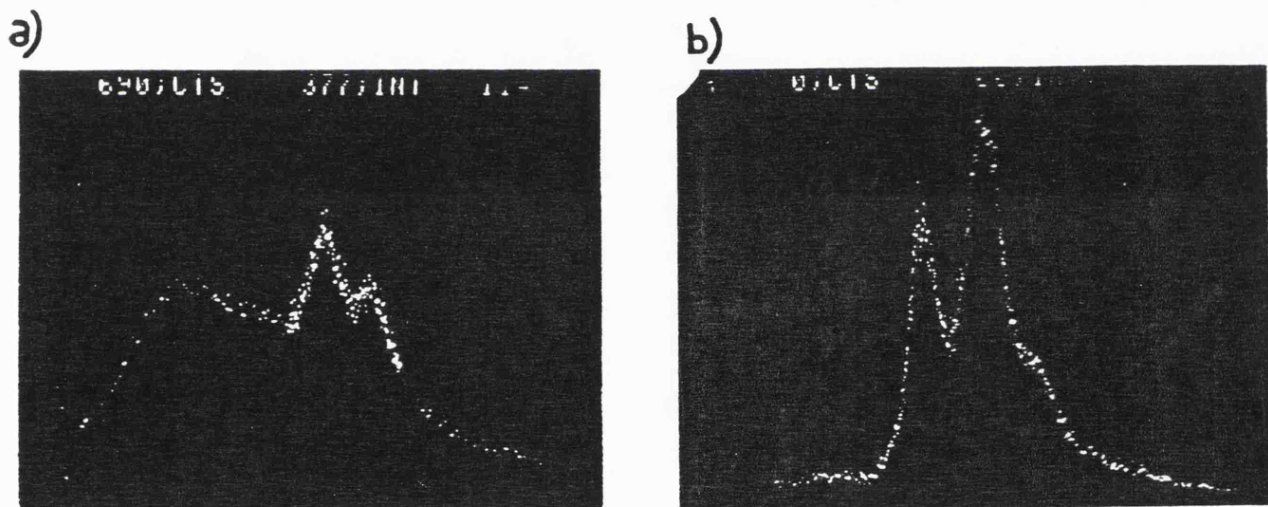


Fig. 7.15 Pulse height spectrum detected on signal anode 1 from the LL phantom (a) compared to that from a plutonium source (b).

Anode	R_S	R_B	F
1	0.87	0.60	0.79
2	0.91	0.66	0.80
3	0.85	0.66	0.91
4	0.89	0.71	0.80
5	0.86	0.57	0.77

Table 7.11 Measurements of the signal and background acceptance ratios resulting from narrowing the energy window.

Layer	ϵ per 10^4	R_S	R_B	B_1 [min^{-1}]	S_1 [min^{-1}]	$(\sigma_2/\sigma_1)^2$	σ
1	0.934	0.781	0.017	73	0.130	2.9×10^{-2}	2.74
2	0.414	0.806	0.013	63	5.8×10^{-2}	2.1×10^{-2}	4.81
3	0.314	0.812	0.012	54	4.4×10^{-2}	1.8×10^{-2}	5.54
4	0.302	0.830	0.013	46	2.8×10^{-2}	1.9×10^{-2}	8.15
5	0.130	0.872	0.017	38	1.8×10^{-2}	2.3×10^{-2}	12.53
Total	1.994	0.802	0.015	274	0.278	2.4×10^{-2}	2.24

Table 7.12 Performance as a lung monitor. σ is calculated from Eqn. 6.1 using $a = 2.38$.

Table 7.12 shows the final performance of each layer, and of the counter as a whole. ϵ is the number of photons detected, within the acceptance energy band, per 10^4 emitted within the lung, and σ is the relative standard deviation obtained for a counting period of 40 minutes. S_1 is the number of (source) counts that would be detected before electronic discrimination from the standard phantom (26 mm chest wall) for an activity of 500 Bq of Pu^{239} in the lungs. B_1 is the background count rate that would be obtained from an "average" subject within the same energy band, including counts from the natural background of the room, scattered photons from the patient, and from the patient's natural content of potassium and caesium.

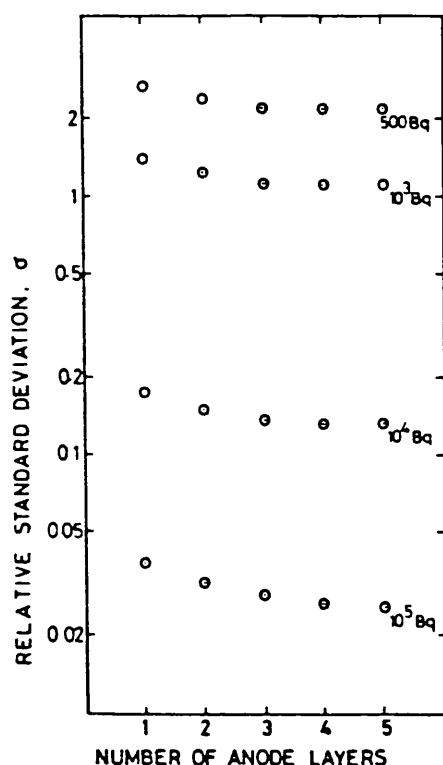


Fig. 7.16 Relative standard deviation of source measurement plotted as a function of the number of layers used for various Pu^{239} lung burdens.

Fig. 7.16 shows the performance of the detector as a function of the number of layers in use for various signal strengths (lung burdens). Although the original calculations suggested that the optimum number of layers would be 5 [88], these results show that this is only true for lung burdens greater than about 10^4 Bq, or approximately 20 times the ALI. For signals below this level it is advantageous to reduce the background count rate by using just four signal anodes, and employing the fifth layer as the rear guard, since the source count rate on the fifth anode is so low.

7.4 Comparison with other monitors

Comparison with other monitors is not always straightforward, since the performance figure used here is particular to a given monitor, and figures such as the minimum detectable activity (MDA) depend on the operating environment, the phantoms used in assessment, and on the definition employed for this value. However, a direct comparison of the prototype lung monitor can be made with the 8" diameter phoswich detector employed in the Body Radioactivity Measurement Section at Harwell since the counters could be operated in the same environment and using the same phantoms.

Here we have defined the MDA as that source strength within the lungs of an "average male" (conforming to the

lung configuration and chest wall thickness of the LL phantom) that would give rise to a measured count equal to twice the standard deviation of the measurement for a 40 minute counting period. The assumed background level includes contributions due to body potassium and scattered photons, and is not just the natural background count rate of the room.

Under these criteria, and with the same 26 mm chest wall on the Livermore phantom, the phoswich detector achieves an MDA of approximately 60 nCi (2.2 kBq) [104, 111], while for the proportional counter (normalised to the same sensitive area as the phoswich) this value was measured as 55 nCi (2.0 kBq), a modest improvement. However, due to temporary physical restrictions, the monitor could not be placed in the optimum sensing position during the course of these measurements, and it has been shown [112] that the detector response is critically dependent on the position and orientation of the detector relative to the phantom, so that, for example, a longitudinal displacement of 3 cm can lead to a 20% change in detected count rate. It has been calculated that if a geometrical efficiency equal to that obtained by the phoswich had been possible, and for the same chest wall thickness (by assuming an incident x-ray flux on the proportional counter window over an area corresponding to the active volume of the detector equal to that quoted for the phoswich (4 x-rays per 10^4 emitted in the lungs [104])), then the MDA would have been around 45 nCi (1.7 kBq) [58]. This represents an improvement (of some 25%)

over the performance of the phoswich detector in use at present if the assumed value of $a=2.38$ used throughout the calculations is appropriate for both detectors. This value represents uncertain factors involved in predicting the "body" background, and has been relatively well established for the phoswich [109]. It was adopted for the proportional counter in the absence of a more reliable figure for which measurements of dozens of control subjects would be required. Although as many variables as possible have been made common between the two detectors, direct comparisons must be tentative for this reason. It must also be admitted that the proportional chamber is much the more complicated both in terms of equipment and operation.

Evidently neither instrument is satisfactory for the intended purpose. Firstly, as mentioned in Chapter 5, in practice one does not want to detect the ALI (500 Bq) but rather the smaller amount of retained material (RALI - 75 Bq). Moreover, in order to comply with the law, an investigation is required should an intake in excess of 30% of the limit is suspected, which for the case we are considering represents a burden of ~25 Bq. Also, even if it were possible to detect such a small signal at the 2σ level, a patient containing that burden would still only have a 50% chance of giving a signal equal to or greater than this level. In order to stand a strong (98%) chance of doing so, the subject would have to contain twice as much plutonium.

Chapter 8

Charge Shape Discrimination

8.1 Theory

Pulse shape discrimination (see Chapter 3) provides information on the nature of an ionising event from the spread in the electron arrival times, and is thus related to the extent of the charge cloud perpendicular to the detector anode. Similar information is contained in the extent of the charge cloud parallel to the plane of the anode in a multiwire counter, and thus in the breadth of the induced charge distribution on the cathodes.

Van Beek et al [113] described a method by which the lateral extent of the charge cloud in both dimensions parallel to the anode plane could be measured at the same time as providing two-dimensional position sensitive detection. This system employed six readout signals, and enabled events due to particles traversing the counter in directions deviating from perpendicular to the anode by more than about 2° to be rejected.

The width of the induced charge distribution can be measured in one dimension, that perpendicular to the cathode wires, using a simple cathode divided into strips of equal width. Each third strip is connected together, thus

producing three output signals (see Fig. 8.1).

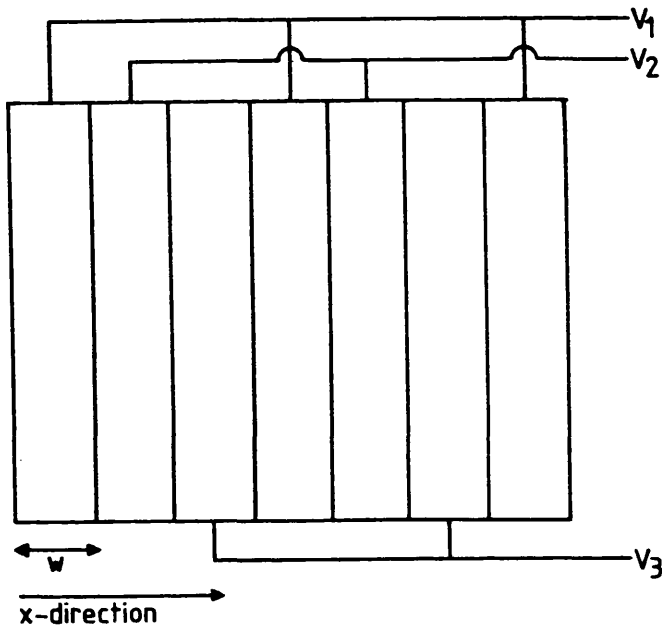


Fig. 8.1 Division of the sensing cathode into strips. See section 8.2.2 for description of the experimental version.

If the strip width, w , is comparable to the width of the induced charge distribution, the amplified signal from each set of strips will vary cyclicly with the position of the event in the x direction. The peak amplitude will obviously coincide with the centres of the strips. Also, if the strip widths are uniform, and the gas gain of the detector and the gain of the amplifiers are uniform and equal, the responses from each set of strips will be the same, but shifted in phase by $2\pi/3$.

The variation in the amplified signal, $V(x)$, with position depends on the relative width of the strips to that of the charge distribution (Fig. 8.2).

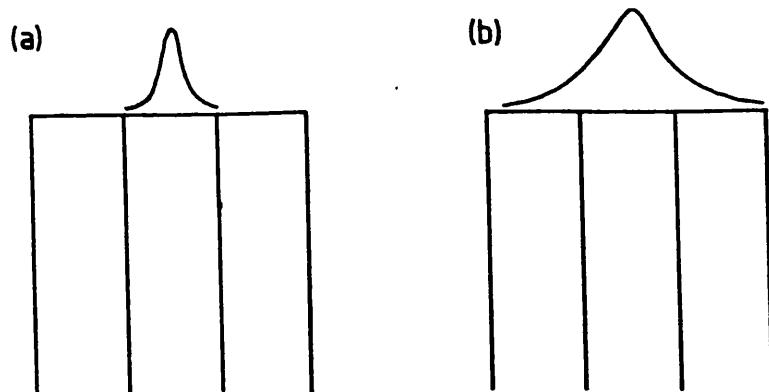


Fig. 8.2 For a relatively narrow charge distribution (a) the signal from each set of strips will vary between 0 and 100% of the total induced charge, while for a broad distribution (b) the fluctuation is smaller.

The algorithm

$$Q(x) = \frac{V_h(x) - V_l(x)}{\Sigma V(x)} \quad \text{Eqn. 8.1}$$

where $V_h(x)$ is the highest value of the three signals at position x , and $V_l(x)$ is the lowest, thus provides a value dependent on the width of the induced charge distribution: for a narrow peak $V_h(x) \gg V_l(x)$ and $Q(x) \rightarrow 1$; and for a broad peak $V_h(x) \approx V_l(x)$ and $Q(x) \rightarrow 0$. The denominator, $\Sigma V(x)$, normalises $Q(x)$ with respect to the total charge induced on the sensing cathode in order to eliminate the effects of the finite energy resolution of the detector and of the avalanche angle.

Due to the form of $V_h(x)$ and $V_l(x)$, $Q(x)$ will be position dependent to a certain extent (see Fig. 8.3).

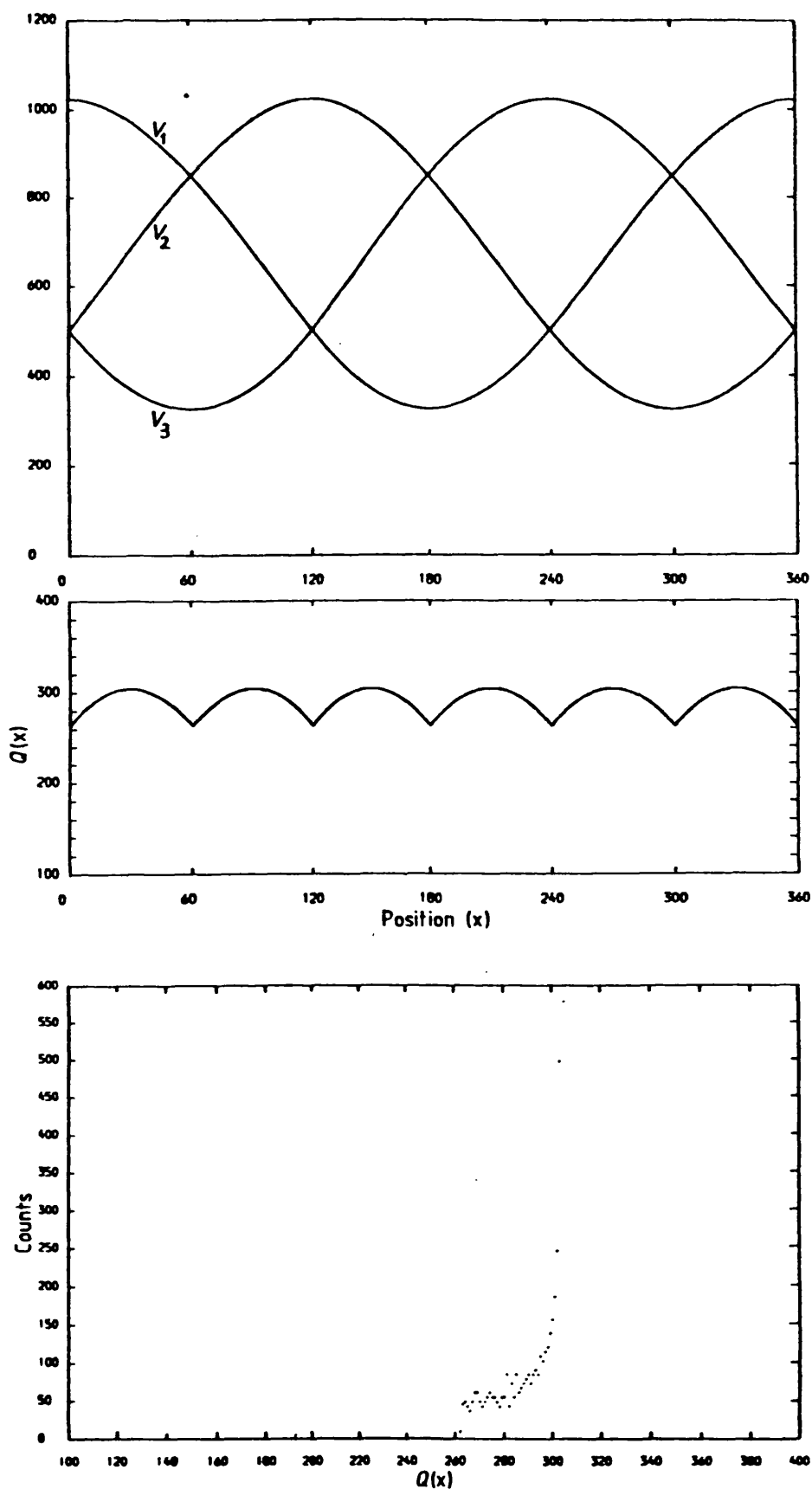


Fig. 8.3 Example of V_1 , V_2 , V_3 , Q and the spectrum of Q measured as a function of position, using a sinusoidal form as a crude approximation, and assuming zero noise. The spectrum is displayed as it would be seen on a 1024 channel MCA, and the calculations model the digital signal processing employed experimentally.

For a given charge distribution width the extent of this dependence is related to the strip width, and may be reduced by using narrower strips. This, however, while reducing the width of the spectrum, also reduces the dependence on the extent of the charge cloud. For purposes of discrimination, these two considerations are thus in direct conflict. This is demonstrated in Fig. 8.4, which shows charge width spectra calculated assuming a basic rectangular induced charge distribution. The avalanche extension, X , is defined as

$$X = w_a / w \quad \text{Eqn. 8.2}$$

where w_a is the width of the avalanche and w is the strip width.

8.2 Apparatus

A system has been developed to assess the practicability of this method for background rejection.

8.2.1 The chamber

The chamber consists of an 18 x 18 x 4.5 cm gas volume surrounded by the biasing network housing. Contacts with the electrodes are via feed-throughs passing through glass/metal insulating seals. The electrodes are mounted

on four pillars, spaced 11cm apart, and consisting of stainless steel rods covered by a ceramic collar. The separation of the electrodes could be adjusted using spacing washers, the minimum being 4mm (Fig. 8.5).

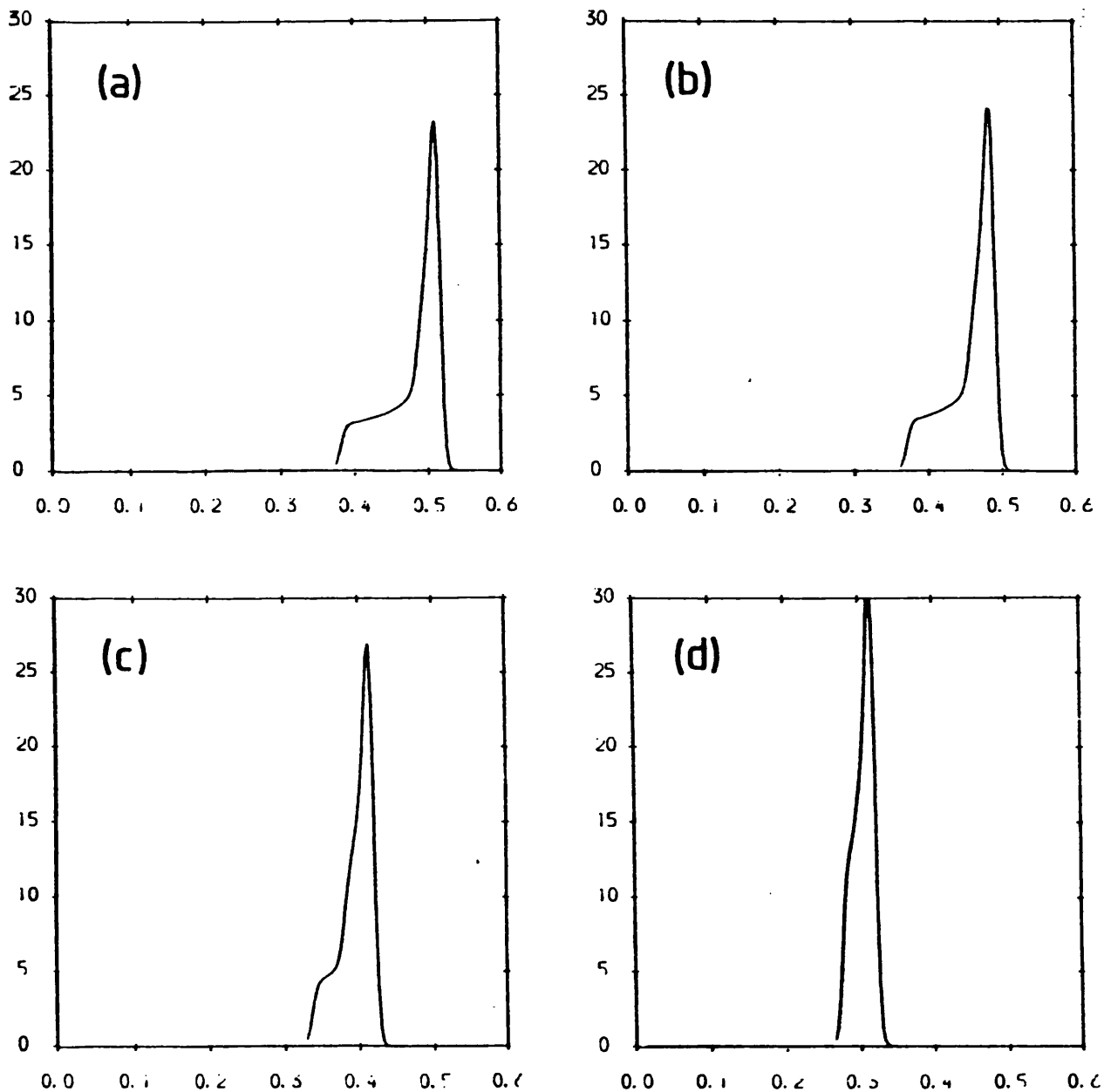


Fig. 8.4 Charge width spectra calculated using a model charge distribution and assuming a signal to noise ratio of 100.

(a) $X=0$, (b) $X=0.5$, (c) $X=1.0$, (d) $X=1.5$. In each case $w/h=1.0$.

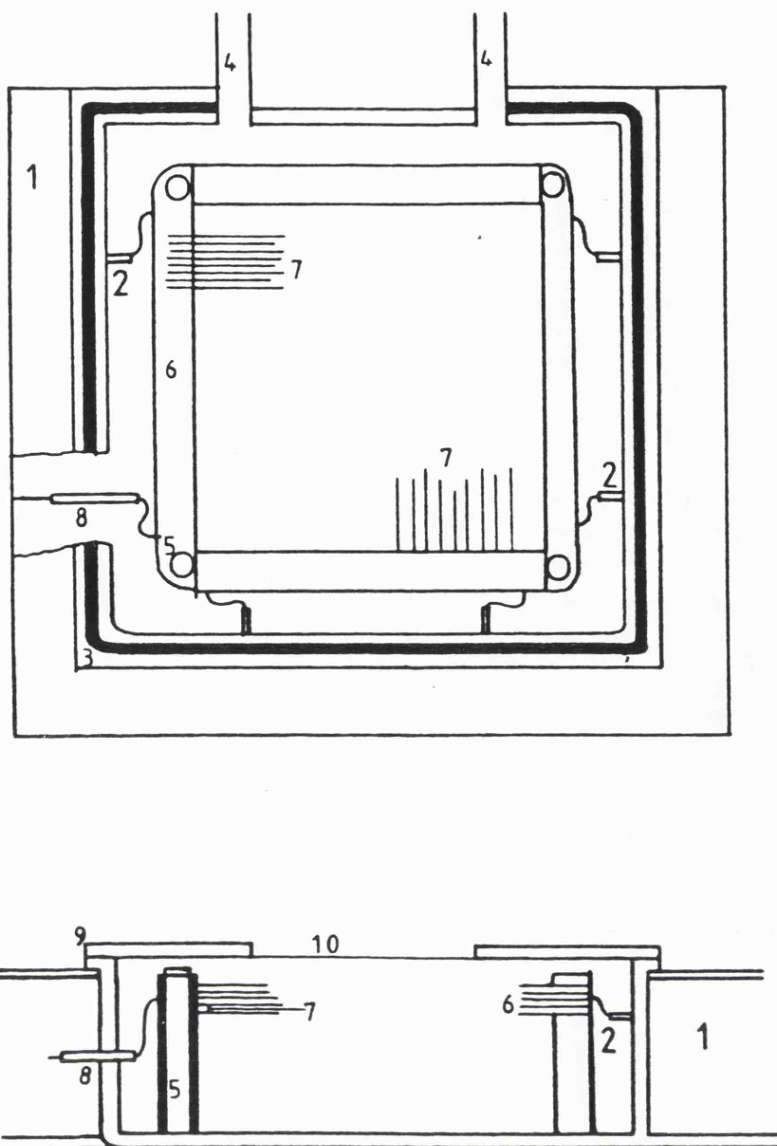


Fig. 8.5 Plan and cross-section of the proportional chamber.

- | | |
|--------------------|--------------------------------|
| 1 Manifold | 6 Electrode frames |
| 2 Feed-throughs | 7 Electrode wires |
| 3 O-ring | 8 Glass/metal seals |
| 4 Gas ports | 9 Chamber Lid |
| 5 Mounting pillars | 10 Aluminium foil x-ray window |

The chamber lid contains a 7 x 7 cm window of 4 μ m aluminium foil, supported by a tungsten mesh which prevents bowing. A gas-tight seal between the lid and walls is obtained with a rubber "O" ring located in the top of the chamber walls.

Two gas ports provide an inlet and outlet for the counter gas (P10, 90% argon 10% methane), enabling a constant flow to be maintained.

8.2.2 The electrodes

The wire electrode arrays are 9cm square, and were hand-wound and checked for geometrical accuracy. The anode wires are of 15 μ m copper wire at a pitch of 2mm, with the edge wires increasing in diameter (up to 115 μ m) to reduce the intensity of the electric field at the edge of the grids. The cathode wires are 50 μ m diameter, at a pitch of 1mm. Calculations [114] suggested that for the minimum electrode spacing (4mm) the cathode strip width should be approximately 4mm also. Each strip thus consisted of 4 neighbouring wires connected together, which each third strip connected to provide the three output signals.

A negative bias of 250 V was applied to the cathode to minimise displacement of events by cathode wire modulation.

8.3 Preliminary results

In order to check the cathode wiring, the signals from each of the three outputs were measured as a function of position using a collimated Al K (1.5 KeV) x-ray source at a charge level of 0.2 pC.

Angular localisation of the avalanche results in significantly different induced charge distributions on the cathode for events occurring on the same side of the anode array as the sensing cathode (near-side events) from those occurring on the far side (far-side events) [25]. For far-side events the liberated positive ions drift away from the sensing cathode, resulting in a lower and broader induced charge distribution than occurs when the ions drift toward the cathode after near-side events (Fig. 8.8). These events were measured separately using crossover discrimination on the non-sensing cathode to distinguish between the two.

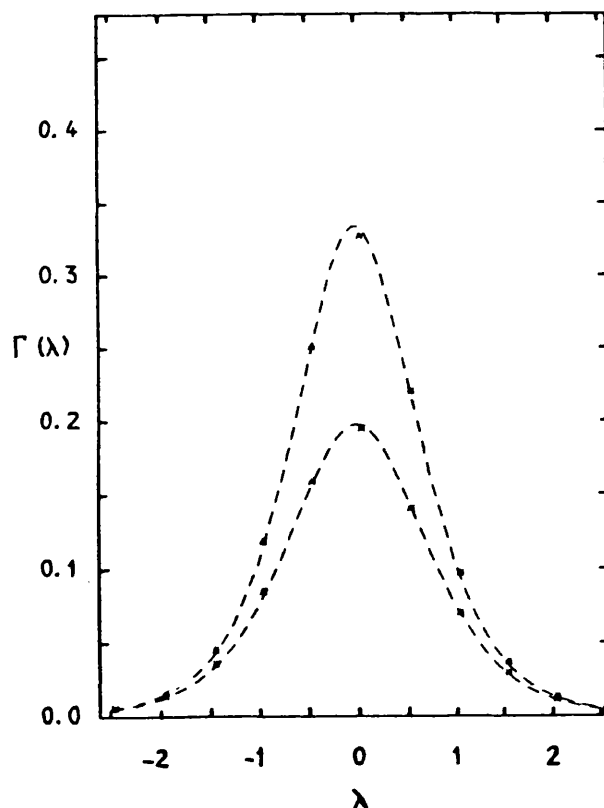


Fig. 8.6 Experimental and theoretical cathode induced charge distribution functions for near-side (upper curve) and for far-side (lower curve) events [25].

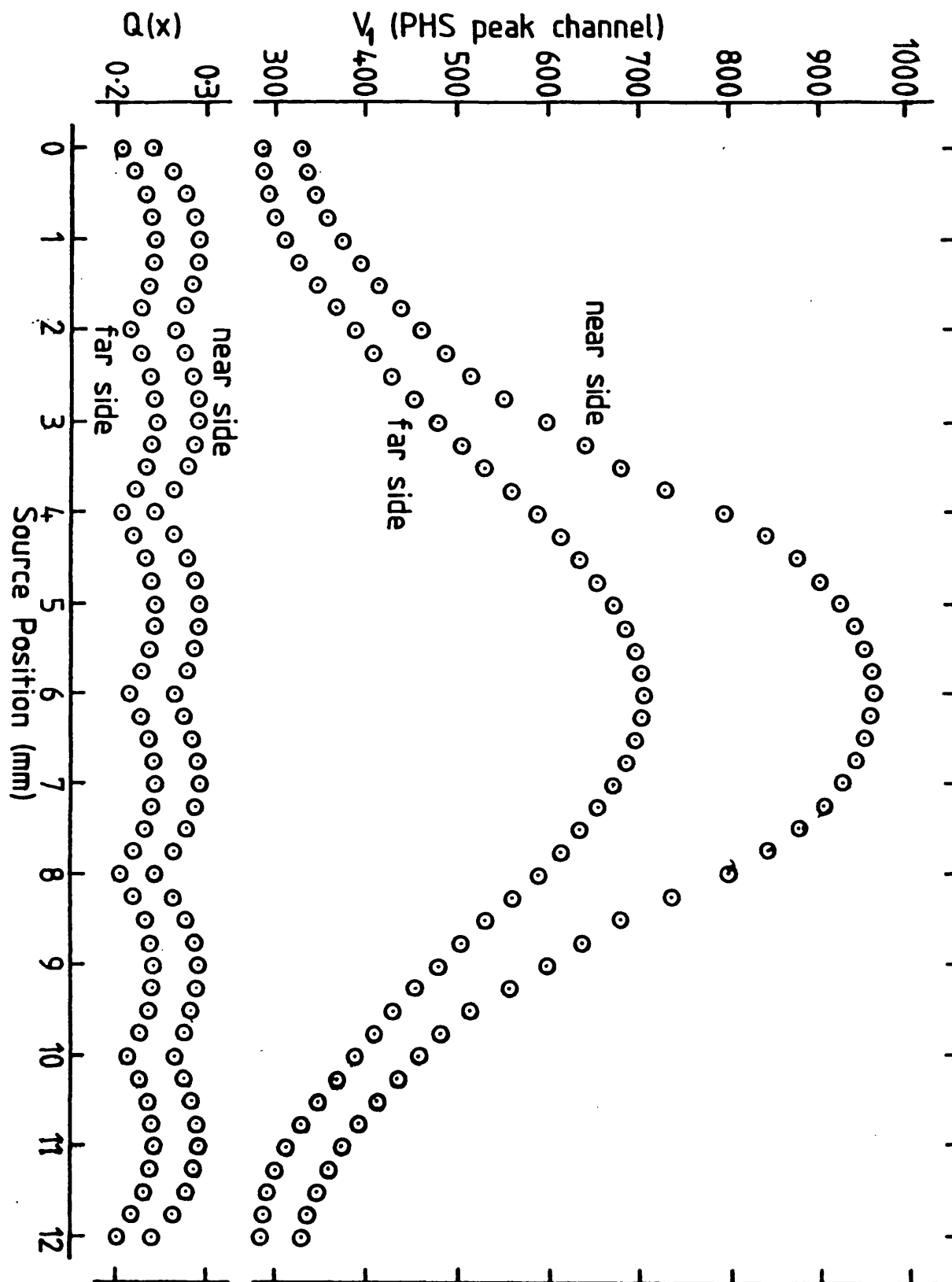


Fig. 8.7 V_1 , V_2 , V_3 and Q , measured as a function of position for "near-side" and for "far-side" events.

The spectra of Q signals can be calculated from these results, neglecting the effects of noise and resolution (Fig. 8.10), and have also been calculated for $w/h=2/3$, using results obtained with a grid spacing of 6mm.

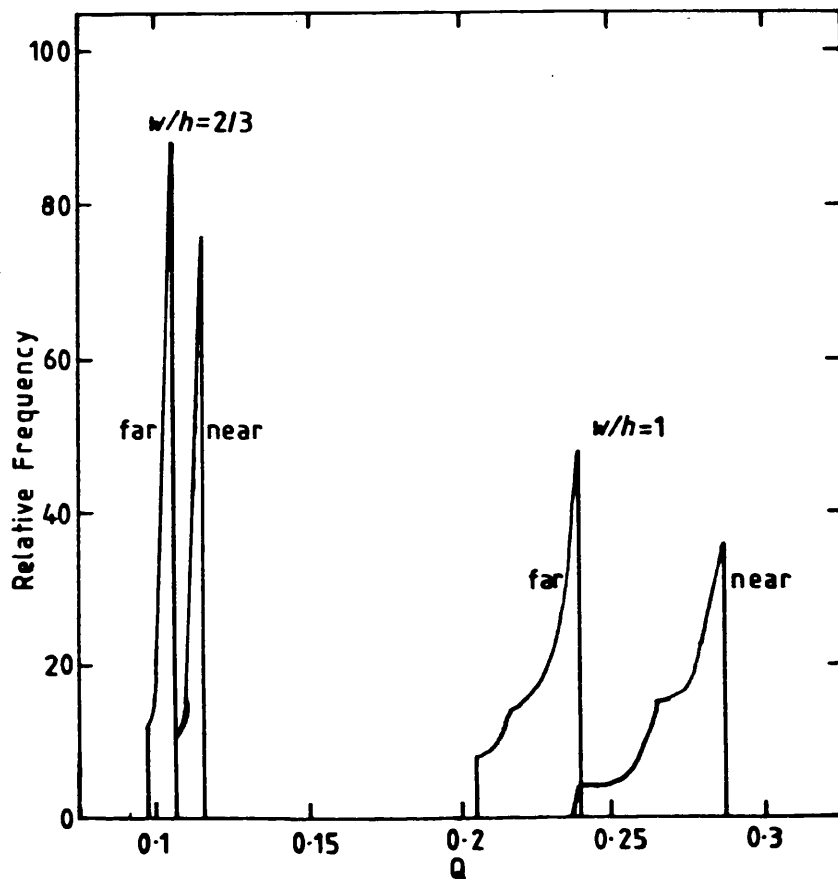


Fig. 8.8 Calculated spectra of Q signals for near-side and for far-side events for $w/h=1$ and for $w/h=2/3$.

It is noticeable that for a given grid spacing, the difference in the induced charge distribution for near-side and for far-side events is sufficient to result in resolvable charge width spectra, though of course it must be remembered that these are essentially theoretical results and that experimental spectra will be blurred due to noise. The broader distribution associated with far-side events

results in lower values of Q and a narrower spectrum. Increasing the grid spacing (which is, of course, equivalent to reducing the strip width) also broadens the induced charge distribution, resulting in narrower peaks at lower values of Q , separated by a smaller amount. These two effects, however, apparently cancel, resulting in a similar degree of resolution between near-side and far-side events.

8.4 Results

In the final system the cathode signals are processed by matched amplifiers and ADCs, which feed a BBC microcomputer via an interface (Fig. 8.9).

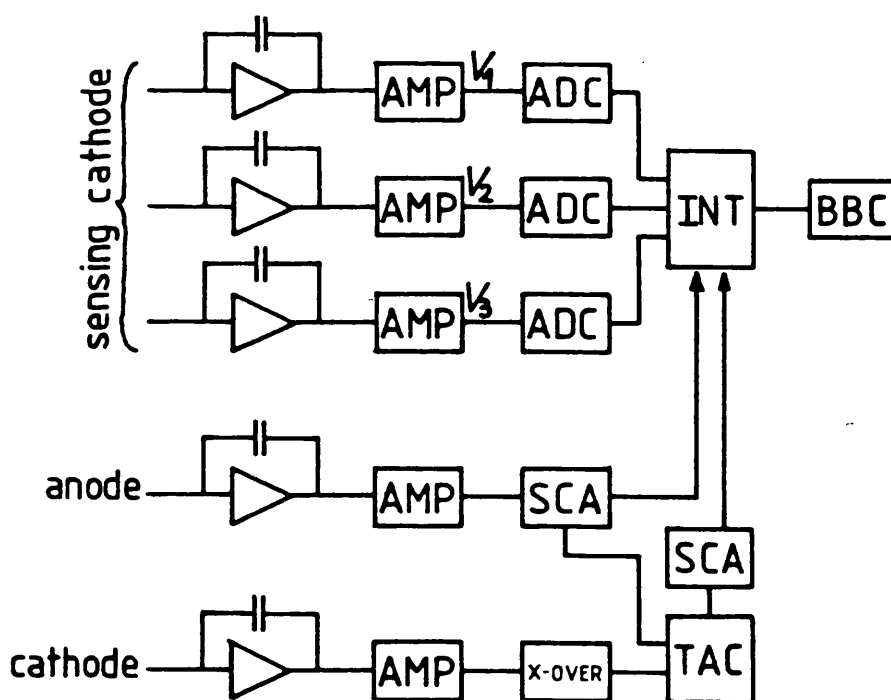


Fig. 8.9 Circuit diagram for measuring charge width spectra.

The interface also allows the use of a coincidence signal, which may be employed to produce pulse height or crossover discrimination. A basic program simulates a multichannel analyser for storing the spectra of Q , calculated by a machine code subroutine activated by interrupts from the ADCs.

Figs. 8.10 and 8.11 show examples of charge width spectra obtained using this system.

The reduction in the values of Q for the larger electrode spacing results from greater diffusion extending the induced charge distribution. The "structure" seen in these spectra, the evidence of unresolved peaks in Fig. 8.10 a) and the discontinuities in all four spectra, are the result of slightly mismatched amplifier gains or ADC baselines, and do not represent a chamber effect. In fact, the predicted chamber effects due to event position and cathode modulation are not noticeable due to the greater influence of resolution and processing effects. This is demonstrated in Figs. 8.12 and 8.13. A discrepancy as small as 4% in amplifier gain or 3% in the mean digital signal is sufficient to produce this effect.

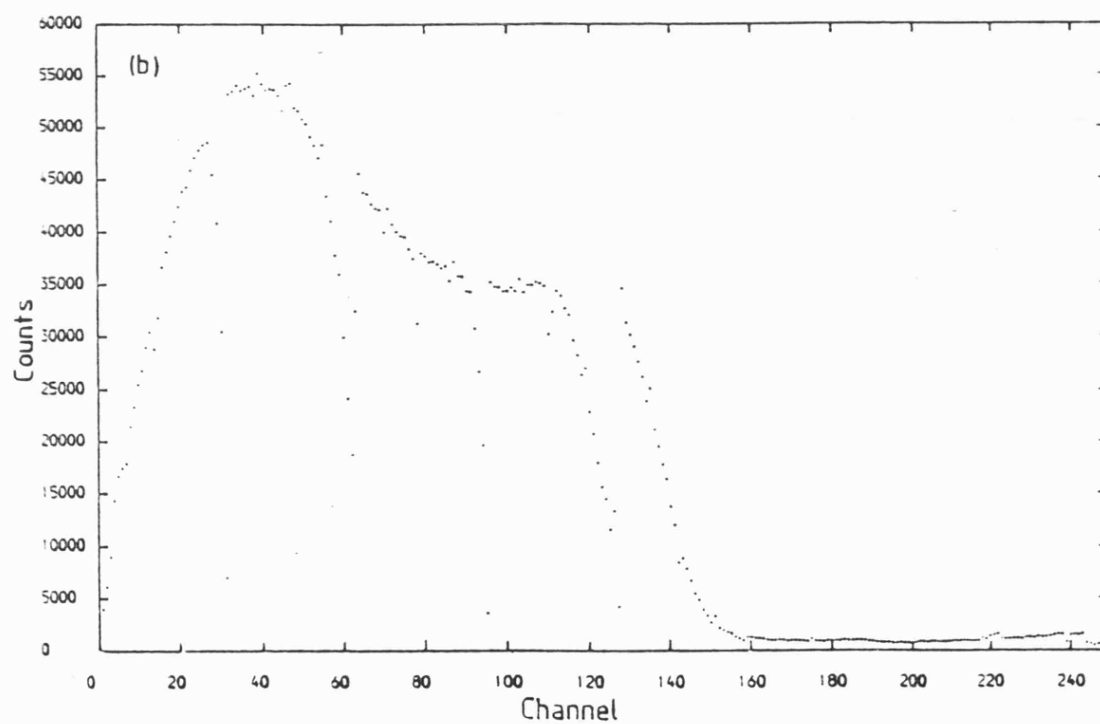
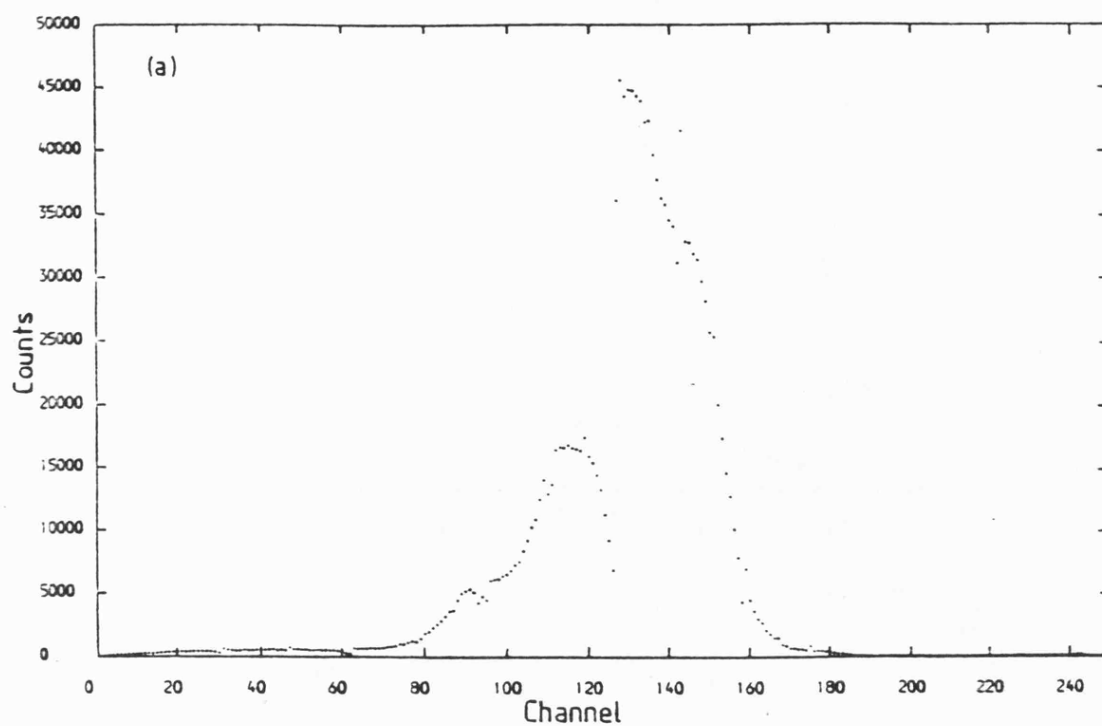


Fig. 8.10 Examples of experimental charge width spectra obtained with a grid spacing of 4mm.

a) Mn K x-rays.

b) Background radiation.

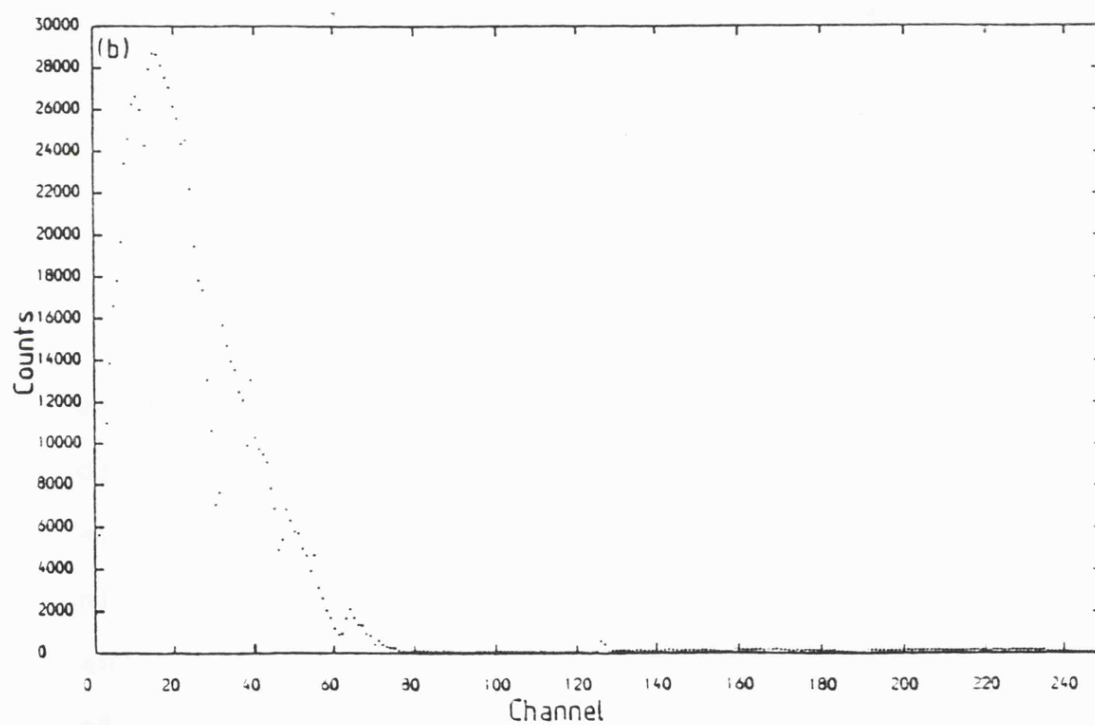
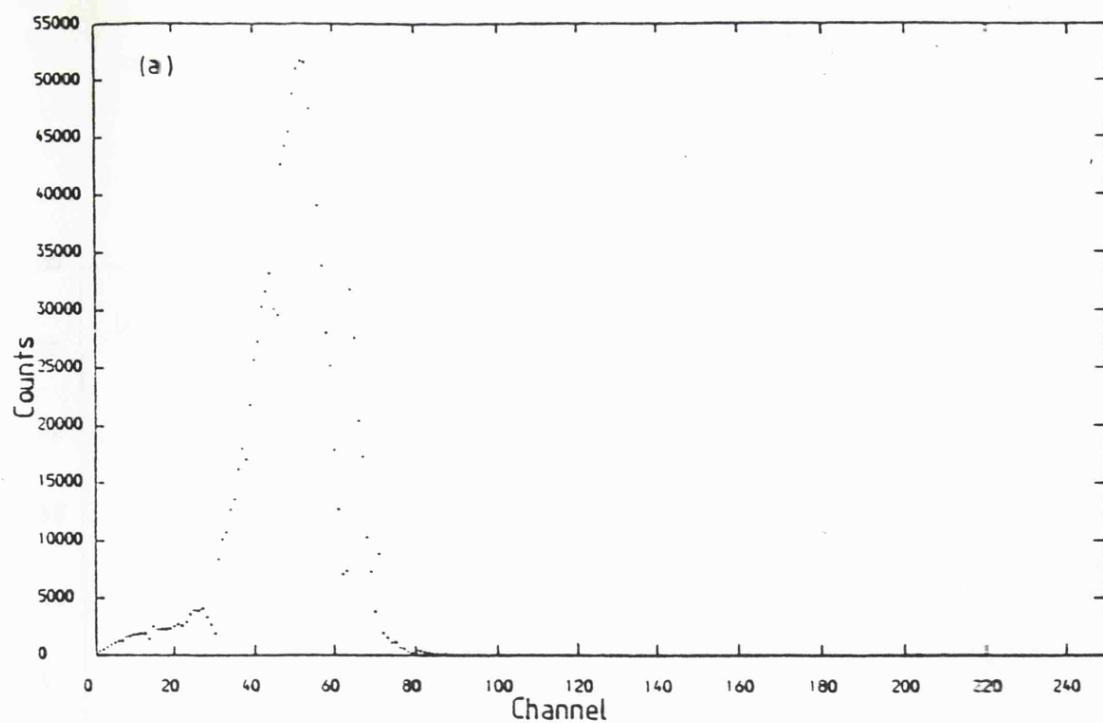


Fig. 8.11 Examples of experimental charge width spectra obtained with a grid spacing of 6mm.

a) Mn K x-rays

b) Background radiation

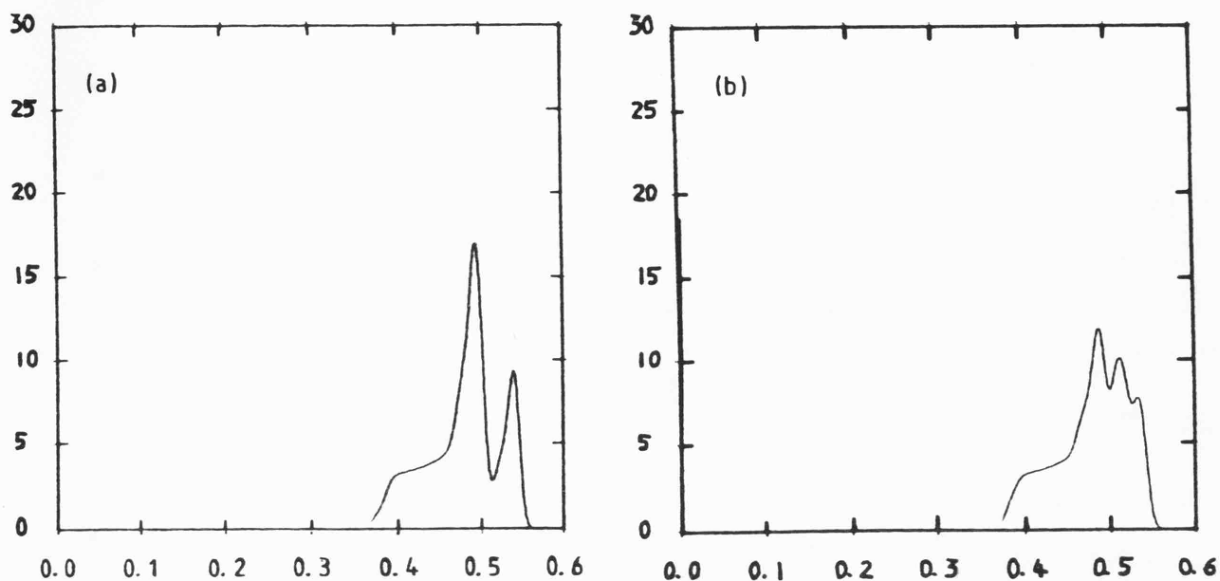


Fig. 8.12 These spectra show how multiple peaking results from mismatching of amplifiers or ADC baselines.

- a) 10% increase in the gain of V_3
- b) 5% increase in V_3 and decrease in V_1

While this effect is obviously unwanted, so long as the mis-matching is slight, it has little effect on the level of discrimination possible between signal and background events. This is evident from the great difference in the signal and background spectra shown in Figs. 8.10 and 8.11, and in Fig. 8.14, which shows the signal and background efficiencies, and the associated figure of merit (again as defined in Chapter 6) as a function of the position of the discrimination level relative to the charge width spectra.

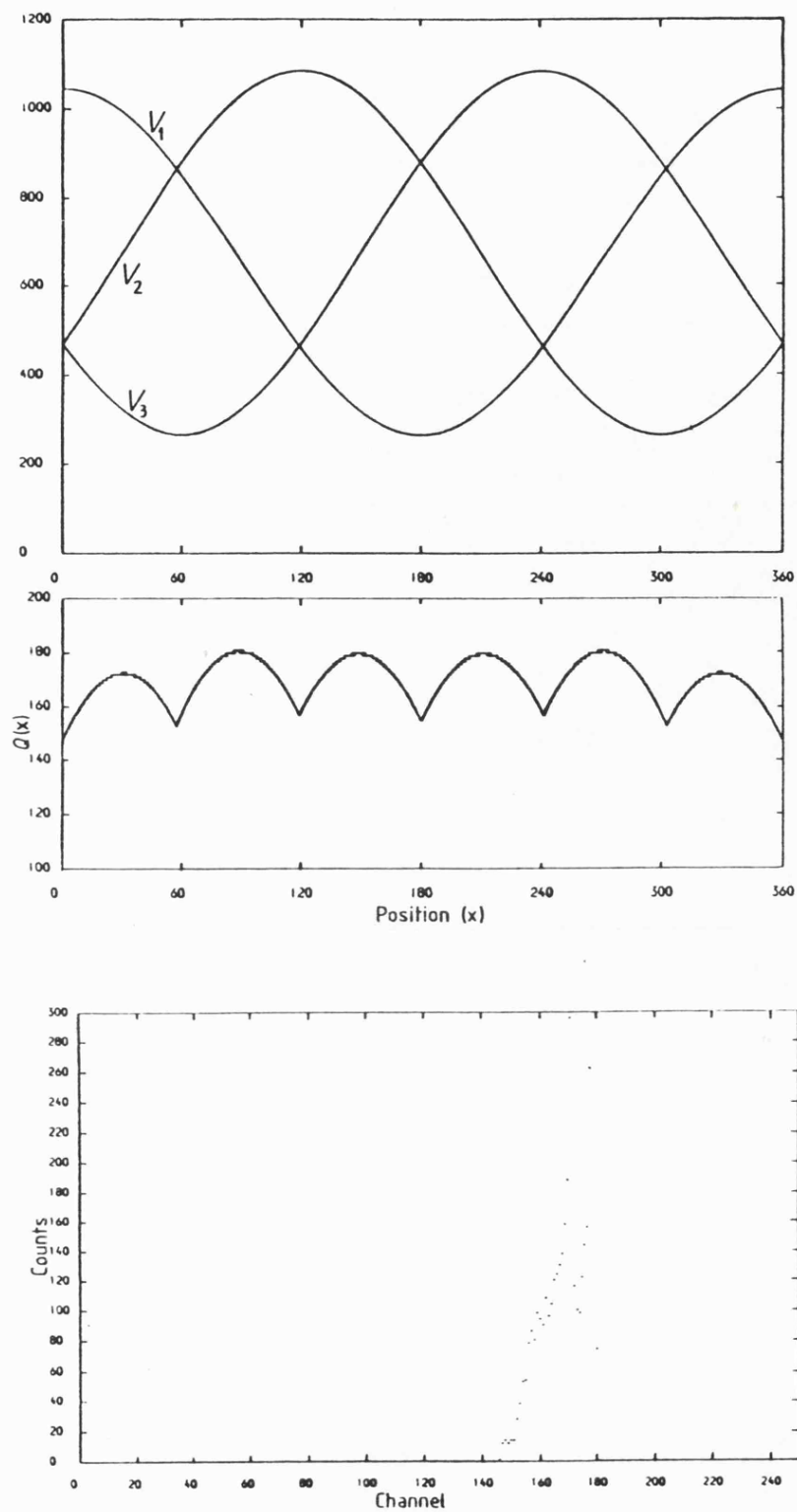


Fig. 8.13 V_1 has 5% lower gain than the other signals, and a baseline offset has been included to make V_{low} consistent. This represents the most likely experimental conditions. V_{high} and Q thus show 360° periodicity. The digital processing results in two peaks, with a sharp discontinuity between.

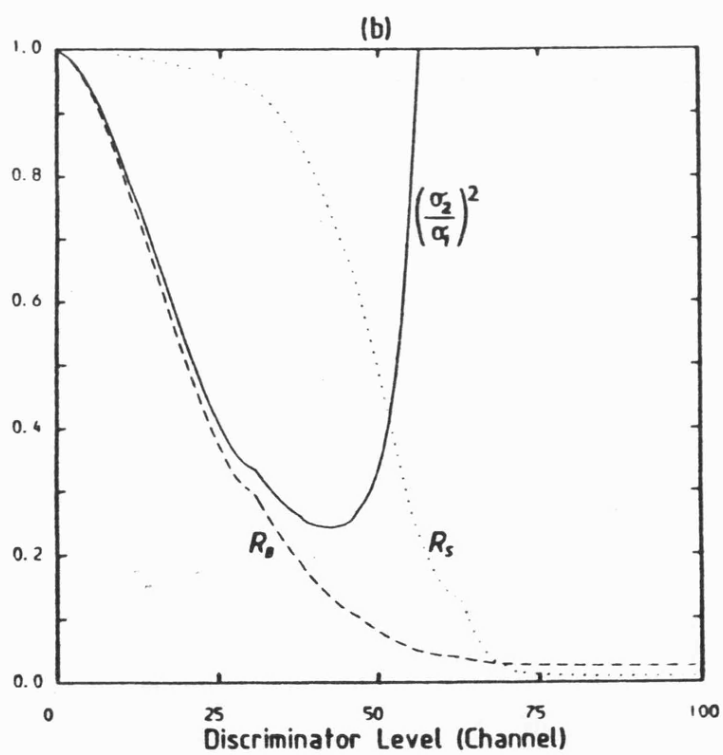
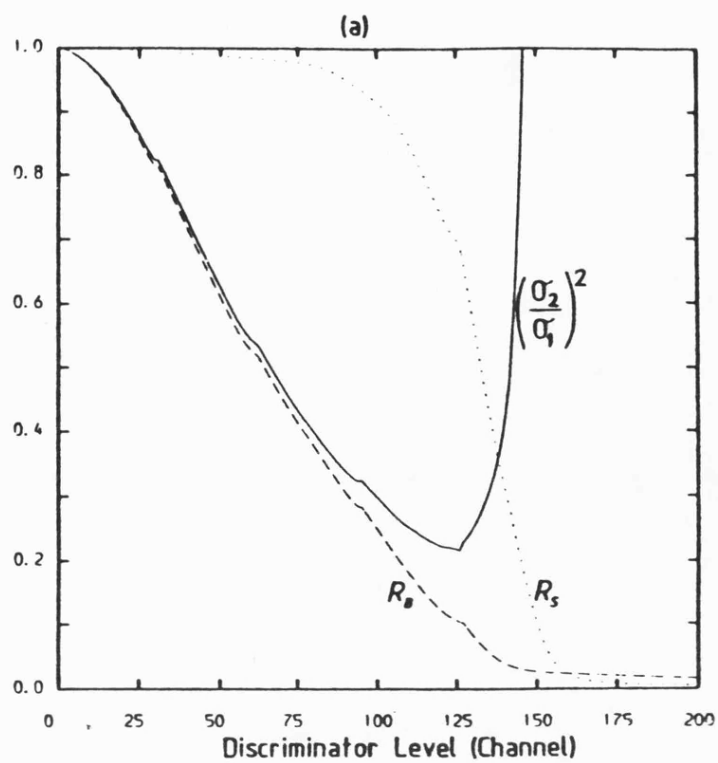


Fig. 8.14 Signal and background acceptance ratios, and the associated figure of merit, for charge width discrimination.

a) for 4mm electrode spacing

b) for 6mm electrode spacing

It is notable that although the spectra are greatly dependant on the electrode spacing, the level of discrimination is not, though of course the accuracy with which the level has to be set is dependant on the the width of the spectra. This obviously makes the broad spectra associated with the 4mm spacing the more advantageous, and similarly a small strip width is preferable to a large one.

The efficiency of this discrimination system is remarkably good considering that only extension of the charge cloud along the anode wires is used. The deviation of the charge track from the perpendicular parallel to the anode wires is thus the only basis of discrimination by this system. However, use of the figure of merit employed throughout this work suggests the system is most efficient for a relatively low signal efficiency (around 70%) and high background rejection (about 90%). If a high signal efficiency is required, say 95%, the background rejection is reduced to 35-40%. This is still comparable to the performance of the best pulse shape discrimination systems.

Chapter 9

Discussion

In today's world the detection of ionising radiation is frequently vital for diagnostic medicine, for radiation protection, and for research. A number of means have been developed, particularly in recent years, for detecting this radiation, which fall into the broad categories of gas detectors, scintillation detectors and semiconductor detectors. Each of these systems has advantages and drawbacks which has so far prevented any specific detector attaining universal use.

For some applications high efficiency detection of small signals is required along with one or two-dimensional imaging capability. This requires complicated and expensive data processing systems, but fortunately one or other consideration is often paramount. This is the case in radiation protection monitoring, where imaging capability would in many cases be desirable but high efficiency signal detection is essential. An example of this is in monitoring contamination of the lung by airborne plutonium isotopes, where the problem is accentuated by the nature of the radiation emitted by the contaminant. Plutonium is an α -emitter, which is the most damaging radiation to an organism because of the large amount of energy deposited in

the vicinity of the contaminant. For this reason the emitted particles have a small penetration depth through tissue, and can not be detected externally. Instead, detection has to be based on measurement of the penetrating x-rays emitted from only a small percentage of disintegrations.

Due to the importance of detection of plutonium in vivo, considerable effort has been devoted to developing more sensitive systems. For this reason, the UKAEA Harwell research laboratory initiated a project to determine whether or not the recent developments in proportional counter design resulting from initiatives in x-ray astronomy would enable a detector to be developed with superior performance to that of the existing phoswich systems.

The result of this work is a multilayer multiwire xenon proportional counter, with a sensitive area comparable to that of the 8 inch diameter phoswich used for the purpose at present at that establishment. The chamber incorporates 6-sided shielding by "massless guards" (guard cells defined electrostatically so as to minimise the amount of material within the active volume of the detector), anticoincidence between layers, and pulse shape discrimination.

In order to facilitate the assessment of this counter a figure of merit was derived to indicate the performance of the detector as a function of the signal and background efficiencies resulting from application of discrimination

systems, and of the initial signal and background count rates. The number of considerations involved in expressing counter performance make it impossible employ a single figure that is universally applicable.

This counter has a low intrinsic background count rate and good signal acceptance and background rejection efficiencies. The two simplest rejection systems, the guard anodes and layer anticoincidence, are highly efficient and result in a minimal loss of signal. The guard cathodes, however, result in ~10% signal loss in addition to reducing the effective sensitive area by intensifying the field at the ends of the anode wires and thus increasing the gas gain. The front guard cathode is efficient at reducing the number of background events resulting from Compton electrons ejected from the front window detected on layer 1.

Pulse shape discrimination is more complicated. The performance of two readily available units for this purpose were investigated, and found to be inadequate for this particular application. A crossover discrimination system was thus developed to make full use of the pulse shape characteristics of the detector. In practise this system provides ~95% rejection of background for ~5% loss of signal. The shape of the background spectrum shows that the small number of false events that are not rejected by this system are mainly those resulting from point ionisation and are thus indistinguishable from genuine signal events, rejection of long track events being nearly 100%.

A by-product of the development of the crossover discrimination allowed investigation of the mobility of the positive ions in the high field region close to the anode. These measurements showed that charge transfer from the Xe^+ atomic ion to the molecular Xe_2^+ ion occurs over time scales of $\sim 1\mu\text{s}$, corresponding to reduced field strengths, E/p , of 60-70 V/cmTorr.

In the years since the counter was built the electrodes show some sign of deterioration, which has a detrimental effect on the counter performance by worsening the gain consistency, and thus the resolution, on layers 1 and 2. Such a deterioration can be expected due to a build up of contaminants on the anode wires as a result of prolonged use at high voltage. The counter gas, however, shows no noticeable deterioration, indicating that the early problems of establishing a good seal have been overcome.

Charge width discrimination is complimentary to pulse shape discrimination because it relies on the extension of the charge cloud in the perpendicular axes. The system investigated here is as simple as is feasible, but still requires complicated processing electronics, in particular the use of a microcomputer to calculate an algorithm. The system requires very careful tuning, in terms of the amplifier gains and ADC baselines in particular, and the form of the charge width spectra are highly dependant on the relative width of the cathode strips to that of the induced charge distributions, but the level of discrimination

possible by this method is good.

This system could be applied to the multiwire lung monitor, at the expense of more complicated cathode wiring. It is doubtful, however, if it would make a significant contribution to the background rejection because, as stated above, the remaining background is almost entirely due to short track events that are indistinguishable from the x-ray point ionisation. A similar argument applies to the possibility of using anticoincidence between anode wires within each layer, and the only improvement in performance, in terms of signal and background acceptance ratios, will arise if the source of this residual background could be identified and if a means of discrimination were applicable.

One modification which might improve the detector performance would be to lengthen the anode wires, and thus make the guard cathodes (end guard cells) more remote from the sensing volume. This should reduce the loss of signal, and only increase the background by a small amount. Of course the dimensions of the detector are subject to optimisation, by balancing the solid angle presented to the source against overall detector volume (and thus background level), in a similar way to the operating conditions, though previous investigations by other workers have shown there to be little point in exceeding 8 inch diameters.

In the final analysis the performance of the counter for the specific application for which it was designed,

namely in vivo detection of plutonium, was found to be slightly superior to that of existing systems. However, this improvement in performance is at the expense of considerably greater complexity in design and operation, and any further improvements will also add to the complexity, and cost, of the system. For this reason the multiwire chamber does not appear to have sufficient advantage over the phoswich to warrant replacing it as standard equipment.

Glossary

Auger electron - electron emitted as a result of
de-excitation of an atom

Ballistic deficit - discrepancy between the measured charge
level and the actual avalanche charge due to pulse
processing

Bronchi - large conducting air passages of the lungs,
commencing at the bifurcation of the trachea and
terminating at the bronchioles

Bronchioles - small branching passages controlling air
passage in the lung

Carina (trachea) - the ridge between the proximal ends of
the two principle bronchi

Cervical - pertaining to the neck

Chelate - a highly stable complex formed between a metal ion
and a chelating agent

Chelation - binding of a metal ion by more than one group

Cilia - long slender microscopic processes extending from a cell surface and capable of rhythmic motion

Colloid - a substance that is in a state between that of a solution and an emulsion, where particles are suspended in a fluid medium

Compton scattering - scattering involving elastic collision between incident photons and unbound or weakly bound electrons, whereby the incident photon energy is shared between the scattered electron and the deflected photon

Endosteal - relating to the endosteum, a vascular membrane lining the central (marrow) cavity of the bone

Epithelium - the cellular covering of the skin and mucous membranes

Exosat - a recent x-ray astronomical satellite

Ferritin - a protein constituting a storage form of iron in liver and other tissues

Fluorescent yield - the fraction of photoionized atoms that de-excite by emission of characteristic (fluorescent) photons rather than of Auger electrons

Gastrointestinal - relating to the stomach and intestinal tract

Gonads - testis or ovary

Guard cell - zone used to reject background in a detector on the basis of incident direction

Hydrolysis - reaction in which bonds in the reactant are broken by reaction with water, with the addition of a hydroxyl group (OH) and a hydrogen atom to the atoms previously joined

K shell - innermost atomic electron shell

L shell - second atomic electron shell

Lawrence Livermore (LL) phantom - anthropomorphic phantom developed for calibration of lung monitors

Ligands - molecules or ions that bind to the same central entity

Lumbar - pertaining to the lumbus, the lower part of the back

Lymph - a collection of tissue fluids which passes through the lymphatic vessels into the veins, containing lymphocytes, which play a major role in cellular and humoral (body fluid) immunity

Lymphatic system - system of vessels etc controlling lymph

Maximum permissible burden - the maximum "safe" burden of a
radiosotope, as defined by the ICRP

Mediastinum - cavity containing the heart, pericardium,
great vessels etc

Minimum detectable activity (MDA) - the lowest level of
activity detectable, here defined as that activity
which would give rise to a count rate equal to twice
the standard deviation of that measurement

Oxalate - an ion, salt, or ester derived from oxalic acid
 $(\text{HO}_2\text{C}_2\text{O}_2\text{H})$

Parenchyma - the characteristic or functional tissues or
cells of a gland or organ

Phagocytosis - the process by which a cell surrounds and
engulfs a foreign particle

Phoswich - dual crystal scintillation detector

Photoelectric absorption - process whereby the entire energy
of an incident photon is transferred to the scattered
electron

Plasma - the fluid component of circulatory blood (or lymph
etc) in which elements are suspended

Pleura - a membrane that forms a closed sac

Pulminory - pertaining to the lungs

Resorption - process of absorption or assimilation

Specific activity - disintegrations per unit time per unit
mass of a radioactive source

Spleen - the elongated accessory lymphatic organ of the
vascular system

Sternum - breast bone

Subpleural - immediately beneath the pleural membrane

Thorax - the upper part of the trunk between the neck and
abdomen

Tidal volume - volume of air moved with each inspiration or
expiration

Trachea - windpipe

Transferrin - a plasma protein that reversibly binds iron
and transports it to cells

Vertebrae - bones of the spinal column

Work function - the average energy required to produce an ion pair

Abbreviations

ADC - Analogue to digital converter

AERE - Atomic Energy Research Establishment

ALI - Annual limit on intake, the activity of a radionuclide which, taken alone would irradiate a person, represented by Reference Man, to the limit set by the ICRP for each year of occupational exposure.

AMP - amplifier

ANL - Argonne National Laboratory

Bq - Becquerel, the SI unit of activity, 1 Bq = 1 disintegration per second ($\sim 2.7 \times 10^{-11}$ Ci)

Ci - Curie, unit of activity, 1 Ci $\sim 3.7 \times 10^{10}$ Bq

CWT - Chest wall thickness

DTPA - Diethylenetriaminopentaacetic acid

HPGe - Hyperpure germanium

IAEA - International Atomic Energy Agency

ICRP - International Commission for Radiological Protection

LLD - lower level discriminator

LLNL - Lawrence Livermore National Laboratory

MCA - multichannel analyser

MDA - minimum detectable activity, defined as that source strength within the lungs that would give rise to a measured count equal to twice the standard deviation of the measurement for a 40 minute counting period.

MPB - maximum permissible burden. The maximum radioisotope burden recommended by the ICRP.

MPBB - maximum permissible body burden

MWPC - multiwire proportional chamber/counter

pH - measure of acidity/alkalinity based on the log of the concentration of positive ions in solution

PHD - pulse height discriminator

PNL - Pacific Northwest Laboratories

ppm - parts per million

PSA - pulse shape analyser

PSD - pulse shape discriminator

RALI - retained annual limit on intake

SCA - single channel analyser

TAC - time to amplitude converter

uv - ultraviolet

Symbols

- a - constant dependant on the precision with which the background count rate due to a patient can be determined
- A - atom
- A - gas gain
- \bar{A} - mean gas gain
- A^+ - singly positively ionised atom
- A^* - atom in excited state
- A_1 - contribution to σ_e from fluctuations in the crossover point
- A_2 - contribution to σ_e due to jitter on the start pulse produced by noise on the triggering pulse
- A_3 - contribution to σ_e from variations in t_e due to varying signal pulse heights
- b_1 - constant relating the actual crossover time to the electron collection time

- b_2 - constant relating the dependance of the experimental start time (t_s) to the charge level

- B_1 - total background count rate detected within the chamber within the energy limits defined for the source count rate

- B_2 - total background count rate within the defined energy band after applying electronic discrimination

- C - dimensionless parameter dependant on chamber dimensions, $C=1/2\ln(r_c/r_a)$

- d - distance

- D - electron diffusion coefficient

- e - electron charge

- e^- - electron

- E - electric field strength (V/cm)

- \bar{E} - average electric field strength

- E_b - electron binding energy

- E_e - electron kinetic energy

- E_f - fluorescent photon energy
- E_x - x-ray photon energy
- E/p - reduced field
- f - relative variance in avalanche size
- f_1 - fraction of swallowed material absorbed into the blood
- F - figure of merit, $F = (\sigma_2/\sigma_1)^2$
- F - the Fano factor
- G - discrimination function based on the sum of anode and guard cathode signals
- n_a - number of source events rejected "accidentally" through coincidence with other events.
- n_1 - source count rate
- n_2 - total source and background count rate
- N - the actual number of ion pairs produced as a result of radiation absorption by the photoelectric process.

- \bar{N} - average number of ion pairs produced as a result of absorption of radiation of a specific energy by the photoelectric process.
- p - gas pressure
- P - total number of free electrons produced as a result of the photoelectric process and gas gain
- \bar{p} - average number of free electrons produced
- q - charge
- q_n - rms equivalent noise charge
- q_0 - total avalanche charge
- $Q(x)$ - function dependant on the width of the induced charge distribution
- r - radial distance
- r_a - anode radius
- r_c - cathode radius
- r_f - radial distance reached by the ions in time t_f

- R_B - background efficiency, defined as the ratio of the measured background to the total detected background, B_2/B_1
- R_S - signal efficiency, defined as the ratio of the measured signal to the total detected signal, S_1/S_2
- S_A - anode signal
- S_C - guard cathode signal
- S_1 - total source count rate detected in the chamber
- S_2 - resultant source count rate after applying electronic discrimination
- t - time
- t_e - experimentally measured crossover time
- t_f - ion time of flight
- t_s - experimental start time, ie. the time at which the timing system is triggered
- t_x - actual shaped pulse crossover time
- t_0 - chamber characteristic time

- T_s - start channel integration time constant
- T_x - crossover amplifier time constants
- T_1 - time constant of the first linear integrator in the
Adams/White PSD unit
- T_2 - time constant of the second linear integrator in the
Adams/White PSD unit
- v - ion drift velocity
- \bar{v} - average ion drift velocity
- v_e - electron cloud drift velocity
- $V(x)$ - voltage measured as a function of event position in
one dimension
- $V_h(x)$ - highest value of the three cathode signals
- $V_l(x)$ - lowest value of the three cathode signals
- V_a - anode voltage (V)
- w - width of a strip on the sub-divided cathode
- w_a - electron avalanche width

- W - work function (eV), the average energy required to produce an ion pair.
- X - relative avalanche extension, defined as $X = w_a / w$
- Z - atomic number
- ϵ_k - characteristic electron energy
- μ - ion mobility
- $\bar{\mu}$ - average ion mobility
- μ_e - electron mobility
- σ - relative standard deviation on a lung burden measurement
- σ_A - standard deviation on the size of an electron avalanche produced by a single electron
- σ_{dif} - standard deviation of the extent of an electron cloud due to the effects of diffusion
- σ_{dif} - standard deviation of the extent of an electron cloud due to the effects of diffusion

- σ_e - standard deviation on the measured crossover time

- σ_N - standard deviation on the number of ion pairs
produced as a result of photoelectric absorption of
radiation of a specific energy

- σ_p - standard deviation on the total number of free
electrons produced as a result of the photoelectric
process and gas gain

- σ_0 - contribution to σ_e from charge cloud characteristics

- σ_1 - standard deviation of an activity measurement, before
applying electronic discrimination.

- σ_2 - standard deviation of an activity measurement, after
applying electronic discrimination.

- Σ - summation

- τ - time interval over which the primary electrons reach
the multiplication radius

REFERENCES

The following abbreviations are used in describing journals:

AEEW	Atomic Energy Establishment Winfrith report
AERE	Atomic Energy Research Establishment
AWRE	Atomic Weapons Research Establishment
Brit. J. Radiol. Suppl.	British Journal of Radiology
IAEA	International Atomic Energy Agency publication
IEEE Trans. Nucl. Sci.	Institute of Electrical and Electronic Engineers Transactions on Nuclear Science
J. of Nucl. Sci. and Tech.	Journal of Nuclear Science and Technology
Nucl. Instr. and Meth.	Nuclear Instruments and Methods

Phil. Mag.

Philosophical Magazine

Proc. Roy. Soc.

Proceedings of the Royal Society of
London

Rev. Sci. Instr.

The Review of Scientific
Instruments

- [1] E.Rutherford and H.Geiger, Proc.Roy.Soc.A 81, 141
(1908)
- [2] J.S.Townsend, Phil.Mag. February (1901) 198
- [3] B.B.Rossi and H.H.Staub, "Ionization Chambers and
Counters", McGraw Hill (1949)
- [4] G.Charpak, R.Bouclier, T.Bressani, J.Favier and
C.Zupancic, Nucl. Instr. and Meth. 62, 262 (1968)
- [5] G.Charpak, R.Bouclier, T.Bressani, J.Favier and
C.Zupancic, Nucl. Instr. and Meth. 65, 217 (1968)
- [6] G.Charpak, D.Rahm and H.Steiner, Nucl. Instr. and
Meth. 80, 13 (1970)
- [7] J.E.Bateman, J.F.Connolly, R.Stephenson and G.J.R.
Tappern, Nucl.Instr. and Meth. 190, 385 (1981)

- [8] A.R.Faruqi and C.C.Bond, Nucl.Instr. and Meth. 176, 71 (1980)
- [9] S.E.Sobottka, G.C.Cornick, R.H.Kretsinger, R.G.Rains, W.A.Stephens and L.J.Weissman, Nucl.Instr. and Meth. 220, 175 (1984)
- [10] G.Charpak, Nucl.Instr. and Meth. 156, 1 (1978)
- [11] A.R.Faruqi, Nucl.Instr. and Meth. 217, 19 (1983)
- [12] D.Ramsden, Health Physics 16, 145-153 (1969)
- [13] A.Schmitt and H.Fessler, Diagnosis and Treatment of Incorporated Radionuclides, IAEA-SR-6/47, 285-291 (1976)
- [14] R.Giacconi et al, Astrophysical Journal 230, 540 (1979)
- [15] S.Rappaport, R.Petre, M.A.Kayat, K.D.Evans, G.C.Smith and A.Levine, Astrophysical Journal 227, 285 (1979)
- [16] J.E.Bateman, J.F.Connolly, R.Stephenson and A.C.Flesher, Nucl.Instr. and Meth. 176, 83 (1980)
- [17] A.Jeavons, K.Kull, B.Lindberg, G.Lee, D.Townsend, P.Frey and A.Donath, Nucl.Instr. and Meth. 176, 89 (1980)

- [18] C.B.Lim, D.Chu, L.Kaufman, V.Perez-Mendez and J.Sperinde, IEEE Trans. Nucl. Sci. NS-21.1, 85 (1974)
- [19] D.F.Anderson, R.Bouclier, G.Charpak, S.Majewski and G.Kneller, Nucl. Instr. and Meth. 217, 217 (1983)
- [20] J.L.Alberi, J.Fischer, V.Radeka, L.C.Rogers and B.P.Schoenborn, Nucl. Instr. and Meth. 127, 507 (1975)
- [21] R.A.Boie, J.Fischer, Y.Inagaki, F.C.Merritt, H.Okuno and V.Radeka, Nucl. Instr. and Meth. 200, 533 (1982)
- [22] A.Breskin, G.Charpak, S.Majewski, G.Melchart, G.Petersen and F.Sauli, Nucl. Instr. and Meth. 161, 19 (1979)
- [23] E.Mathieson and T.J.Harris, Nucl. Instr. and Meth. 154, 189 (1978)
- [24] W.H.McMaster, N.Kerr del Grande, J.H.Mallett and J.H.Hubbell, "Compilation of X-ray Cross Sections", Lawrence Radiation Laboratory, University of California Report UCRL-50174 (1969)
- [25] J.S.Gordon, "The Imaging Performance of Multiwire Proportional Chambers", PhD. Thesis, University of Leicester (1985)

- [26] C.D.Wagner, "The Role of Auger Lines in Photoelectron Spectroscopy" in "Handbook of X-ray and Ultra-violet Photoelectron Spectroscopy", Heydon and Son (1977)
- [27] Compton and Allison, "X-rays in Theory and Experiment"
- [28] G.F.Knoll, "Radiation Detection and Measurement", Wiley (1979)
- [29] U.Fano, Physics Review 72, 26 (1947)
- [30] G.D.Alkhazov, A.P.Komar and A.A.Vorob'ev, Nucl. Instr. and Meth. 48, 1 (1967)
- [31] V.Palladino and B.Sadoulet, Nucl. Instr. and Meth. 128, 323 (1975)
- [32] G.Schultz and J.Gresser, Nucl. Instr. and Meth. 151, 413 (1978)
- [33] E.Mathieson and N.El Hakeem, Nucl. Instr. and Meth. 159, 489 (1979)
- [34] F.Piuz, Nucl. Instr. and Meth. 205, 425 (1983)
- [35] A.J.F.Boggende and C.J.Schrijver, Nucl. Instr. and Meth. 220, 561 (1984)
- [36] R.W.Hendricks, Rev. Sci. Instr. 40, 1216 (1969)

- [37] H.Sipila and V.Vanha-Honko, Nucl. Instr. and Meth. 153, 461 (1978)
- [38] H.Sipila, V.Vanha-Honko and J.Berquist, Nucl. Instr. and Meth. 176, 381 (1980)
- [39] E.Mathieson, Nucl. Instr. and Meth. A249, 413 (1986)
- [40] G.Smith and E.Mathieson, IEEE Trans. Nucl. Sci. NS-34, 141 (1987)
- [41] M.Atac, A.V.Tollestrup and D.Potter, IEEE Trans. Nucl. Sci. NS-29, 388 (1982)
- [42] G.D.Alkhazov, Nucl. Instr. and Meth. 89, 155 (1970)
- [43] M.W.Charles and B.A.Cooke, Nucl. Instr. and Meth. 61, 31 (1968)
- [44] H.Sipila, Nucl. Instr. and Meth. 133, 251 (1983)
- [45] P.J.Campion, Nucl. Instr. and Meth. 112, 75 (1973)
- [46] M.R.Sims, H.D.Thomas and M.J.L.Turner, Nucl. Instr. and Meth. 199, 597 (1982)
- [47] H.D.Thomas and M.J.L.Turner, Nucl. Instr. and Meth. 221, 175 (1984)

- [48] D.H.Wilkinson, "Ionization Chambers and Counters", Cambridge University Press (1950)
- [49] E.W.McDaniel and E.A.Mason, "Experimental Data on Mobilities and Diffusion Coefficients", Wiley (1973)
- [50] R.A.Pike and D.Ramsden, AEEW Report M-912, (1969)
- [51] V.Lossner, Diagnosis and Treatment of Incorporated Radionuclides, IAEA-SR-6/17, 249-263 (1976)
- [52] P.Gorenstein and S.Mickiewicz, Rev. Sci. Instr. 39 N^O6, 816-821 (1968)
- [53] K.Doi and M.Fujii, Nucl. Instr. and Meth. 155, 305-306 (1978)
- [54] K.Doi, Nucl. Instr. and Meth. 125, 183-187 (1975)
- [55] E.Mathieson and T.J.Harris, Nucl. Instr. and Meth. 88, 181-192 (1970)
- [56] T.J.Harris and E.Mathieson, Nucl. Instr. and Meth. 96, 397-403 (1971)
- [57] J.L.Culhane and A.C.Fabian, IEEE Trans. Nucl. Sci. NS-19, 569 (1972)
- [58] J.W.Leake, E.Mathieson, P.Ratcliff, and M.J.Turner, Nucl. Instr. and Meth. A269 No 1, 305-311 (1988)

- [59] R.N.Varney, Physics Review 88 N^O2, 362-364 (1952)
- [60] R.Gott and M.W.Charles, Nucl. Instr. and Meth. 72, 157-160 (1969)
- [61] P.Rice-Evans, "Spark, Streamer, Proportional and Drift Chambers", Richelieu Press (1974)
- [62] H.W.Ellis, E.W.McDaniel, D.L.Albritton, L.A.Viechland, S.L.Lin, and E.A.Mason, Atomic Data and Nuclear Data Tables 22, 179-217 (1978)
- [63] G.C.Smith and E.Mathieson, IEEE Trans. Nucl. Sci. NS-34, 410 (1987)
- [64] M.A.Biondi and L.M.Chanin, Physics Review 94, 910 (1954)
- [65] A.M.Tyndall, "The Mobility of Positive Ions in Gases", Cambridge University Press (1938)
- [66] A.M.Tyndall and R.J.Munson, Proc. Roy. Soc. A177, 187 (1940)
- [67] Annals of the ICRP 2 No3/4, "Limits for Intakes of Radionuclides by Workers", Pargamon Press (1979)
- [68] L.A.Konig and H.Schieferdecker, Atomic Energy Review 12 No2, 343-407 (1974)

- [69] K.L.Swinth and P.N.Dean, Health Physics 25, 599-603 (1973)
- [70] R.G.Speight, C.O.Peabody and D.Ramsden, "Assessment of Radioactivity in Man" Vol. 1, 115-130, IAEA publication (1964)
- [71] C.W.Sill, J.I.Anderson and D.R.Percival, "Assessment of Radioactivity in Man" Vol. 1, 217-230, IAEA publication (1964)
- [72] J.D.Eakins and A.Morgan, "Assessment of Radioactivity in Man", Vol. 1, 231-244, IAEA publication (1964)
- [73] "Assessment of Plutonium Internal Contamination in Man", Report of the Commission of the European Communities on Radiation Protection, Report EUR 7157 EN
- [74] R.G.Thomas, "Assessment of Radioactivity in Man", Vol. 1, 355-368, IAEA publication (1964)
- [75] K.L.Swinth, W.J.Bair, P.N.Dean, J.Rundo and F.K.Tomlinson, Health Physics 37, 641-657 (1979)
- [76] A.Morgan, A.Black, S.R.Moores and B.E.Lambert, Health Physics 50 No4, 535-539 (1986)

- [77] G.W.Dolphin and S.Jackson, "Assessment of Radioactivity in Man", Vol. 1, 329-354 (1964)
- [78] G.Voelz, J.Umbarger, J.McInroy and J.Healy, Diagnosis and Treatment of Incorporated Radionuclides, IAEA-SR-6/33, 163-176 (1976)
- [79] W.H.Langham, Brit. J. Radiol. Suppl. No7, 95 (1957)
- [80] D.Newton, B.T.Taylor, and J.D.Eakins, Health Physics 44, Supplement No 1, 431-439 (1983)
- [81] H.Kiefer and R.Maushart, "Whole Body Counting", Proc. of the IAEA Symp. Vienna (1961) 289-298
- [82] W.S.S.Jee, "Assessment of Radioactivity in Man" Vol. 1, Proc. of the IAEA Symp. Heidelberg (1964) 369-394
- [83] F.J.Sandalls and A.Morgan, "Assessment of Radioactivity in Man" Vol. 1, Proc. of the IAEA Symp. Heidelberg (1964) 261-274
- [84] J.Rundo, M.G.Strauss, I.S.Sherman and R.Brenner, Health Physics 35, 851-858 (1978)
- [85] W.W.Parkinson and L.C.Henley, Health Physics 40, 327-331 (1981)
- [86] C.D.Berger, Detector Technology 1 No.2, 3-6 (1985)

- [87] F.W.Spiers, "Whole Body Counting", Proc. of the IAEA Symp. Vienna (1961) 3-14
- [88] J.W.Leake, A.Smith, M.J.L.Turner and G.White, Nucl.Instr. and Meth. A235, 589-596 (1985)
- [89] B.Rajewsky, A.Kaul and J.Heyder, "Assessment of Radioactivity in Man" Vol.1, Proc. of the IAEA Symp. Heidelberg (1961) 15-54
- [90] D.Newton, personal communication.
- [91] C.D.Berger and R.E.Goans, Health Physics 40, 535-542 (1981)
- [92] R.B.Falk, W.H.Tyree, C.B.Wood and C.R.Lagerquist, "Advances in Radiation Protection Monitoring" (Vienna:IAEA), 493-503 (1978)
- [93] D.Newton, J.B.Venn, A.L.Anderson and G.W.Campbell, Health Physics 44 No.1, 69-75 (1983)
- [94] S.Mizushita, J. of Nucl. Sci. and Tech. 21 No.10, 775-785 (1984)
- [95] H.E.Palmer and G.Rieksts, Health Physics 47 No.4, 569-578 (1984)
- [96] I.S.Sherman, M.G.Strauss and R.H.Pehl, Health Physics 47 No.5, 711-721 (1984)

- [97] S.M.Morsy, F.M.El-Assaly and A.A.Aloush, Proc. of a Symp. on the Assess. of Radioactive Organ and Body Burdens, IAEA-SM-150/40, (1972)
- [98] B.T.Taylor, Health Physics 17, 59-69 (1969)
- [99] T.Tomitani and E.Tanaka, Health Physics 18, 195-206 (1970)
- [100] R.C.Sharma, I.Nilsson and L.Lindgren, AE-463 (1972)
- [101] H.E.Palmer, Report PNL-3151 for the U.S.Nuclear Regulatory Commission (1979)
- [102] J.Rundo, "Whole Body Counting", Proc. Symp., Vienna (1961), IAEA, Vienna (1962) 121
- [103] D.Newton et al, Health Physics 35 No6, 751 (1978)
- [104] D.Newton et al, AERE Report R_11210 (1984)
- [105] A.Smith and M.J.L.Turner, Nucl.Instr. and Meth. 189, 511-513 (1981)
- [106] M.J.L.Turner and A.Smith, Space Science Reviews 30, 513-514 (1981)
- [107] E.Gatti, C.Cottoni, S.Donati, V.Svelto and F.Vaghi, Energia Nucleaire 17 No.1 (1970)

- [108] J.M.Adams and G.White, Nucl.Instr. and Meth. 156,
459-476 (1978)
- [109] E.Pochin, AWRE Report (1978)
- [110] E.Mathieson, Personal communication
- [111] D.Newton, Personal communication
- [112] D.Newton et al, Proc. Int. Symp. on the Assessment of
Radioactive Contamination in Man (1985)
- [113] H.F.van Beek, W.A.Mels and A.C.Brinkman, IEEE Trans.
Nucl. Sci. NS-31, No 1, 45-47 (1984)
- [114] E.Mathieson, Personal communication
- [115] ICRP Publication 48, Annals of the ICRP 16 No. 2/3.
Pergamon Press (1986)

Background Rejection in Gas Detectors

PhD thesis by Paul Ratcliff, 1988

Abstract

Investigations have been made on the minimisation of the background count rate detected in proportional counters, while maximising the signal detection efficiency. Two methods of background rejection have been developed, based on the time profile of the shaped detector pulses and on the lateral extent of the induced charge distribution on the cathode. Both these systems have proved highly efficient, and the former has been applied to a multiwire proportional chamber designed as a monitor for plutonium lung contamination, an application where high efficiency detection is critical. This instrument, which incorporates full six-sided "massless" guard cells, and utilises real-time data acquisition and handling by microcomputer, has been developed, optimised, and assessed as a possible competitor to the phoswich detectors in use at present and the solid state detectors under development. Results indicate that the counter is likely to offer no more than a marginal improvement in sensitivity, insufficient to justify its increased complexity and higher costs.